

*Preparation and structure elucidation of
multifunctional porous TiO₂ surfaces
by means of plasma electrolytic oxidation*

Dissertation

zur Erlangung des Doktorgrades der Naturwissenschaften

- Dr. rer. nat. -

Fachbereich 02 (Biologie/Chemie)

der Universität Bremen



vorgelegt von

M. Sc. Ariane Friedemann

Bremen 2018

Diese Arbeit wurde am Fraunhofer-Institut für Fertigungstechnik und Angewandte Materialforschung IFAM Bremen unter der Leitung von Herrn Dr. Peter Plagemann in Kooperation mit der Arbeitsgruppe „Chemische Kristallographie fester Stoffe“ von Herrn Prof. Dr. Thorsten M. Gesing an der Universität Bremen im Zeitraum von Oktober 2014 bis Januar 2018 durchgeführt.

Tag der mündlichen Prüfung: 19.04.2018

- 1. Gutachter:** Prof. Dr. Günter Schmitt, Institut für Instandhaltung und Korrosionsschutztechnik IFINKOR, Iserlohn
- 2. Gutachter:** Dr.-Ing. Herbert Juling, Leibniz-Institut für Werkstofforientierte Technologien IWT, Bremen

SELBSTÄNDIGKEITSERKLÄRUNG

Hiermit versichere ich, Ariane Friedemann
Op de Lust 58, 21640 Nottensdorf
Matr.nr.: 2336186

an Eides Statt durch meine Unterschrift, dass diese vorstehende Doktorarbeit mit dem Titel „*Preparation and structure elucidation of multifunctional porous TiO₂ surfaces by means of plasma electrolytic oxidation*“ von mir selbständig und ohne fremde Hilfsmittel nur mit den angegebenen Quellen verfasst und geschrieben wurde. alle Stellen, die ich wörtlich dem Sinne nach aus Veröffentlichungen entnommen habe sind als solche kenntlich gemacht worden.

Zusätzlich versichere ich an Eides Statt, dass ich die vorgenannten Angaben nach bestem Wissen und Gewissen gemacht habe und dass die Angaben der Wahrheit entsprechen und ich nichts verschwiegen habe. Ebenfalls erkläre ich, dass es sich bei den abgegebenen Arbeiten um identische Exemplare handelt und die zu Prüfungszwecken beigelegte elektronische Version der Dissertation mit der abgegebenen gedruckten Version identisch ist.

Die Strafbarkeit einer falschen eidesstattlichen Versicherung ist mir bekannt, namentlich die Strafandrohung gemäß § 156 StGB bis zu drei Jahren Freiheitsstrafe oder Geldstrafe bei vorsätzlicher Begehung der Tat bzw. gemäß § 161 Abs. 1 StGB bis zu einem Jahr Freiheitsstrafe oder Geldstrafe bei fahrlässiger Begehung.

(Ariane Friedemann)

Bremen, 17. Mai 2018

DANKSAGUNG

Diese Arbeit wurde unter der Leitung von Herrn Dr. Peter Plagemann am Fraunhofer-Institut für Fertigungstechnik und Angewandte Materialforschung IFAM in Kooperation mit Herrn Professor Dr. Thorsten M. Gesing an der Universität Bremen der Arbeitsgruppe „Chemische Kristallographie fester Stoffe“ am Institut für Anorganische Chemie und Kristallographie angefertigt.

An dieser Stelle möchte ich mich bei **Herrn Prof. Dr. Bernd Mayer** besonders für die interessante Themenstellung und für die Möglichkeit bedanken, am IFAM mitzuarbeiten und meine Dissertation anfertigen zu können. **Herrn Prof. Dr. Thorsten M. Gesing** gebührt ein spezieller Dank für die Übernahme der Betreuung dieser Dissertation und der intensiven Hilfe bei jeglichen Fragestellungen und der tollen Betreuung während der gesamten Zeit meiner Promotion.

Für die Bereitschaft zur Übernahme und Erstellung der Gutachten zu dieser Arbeit danke ich besonders **Herrn Prof. Dr. Günter Schmitt, Herrn Dr.-Ing. Herbert Juling** und **Frau Prof. Evelina Slavcheva Ph.D.**

Ein herzlicher Dank gilt **Herrn Dr. Peter Plagemann, Herrn PD Dr. M. Mangir Murshed, Herrn Dr. Lars Robben** und **Frau Dr. Olga Yeszerska** für die intensive wissenschaftliche Unterstützung und Betreuung bei jeglichen Problemen und Fragestellungen.

Für die Anfertigung sämtlicher Rasterelektronenmikroskop-Aufnahmen und FIB-Schnitte sowie Messungen am Transmissionmikroskop, die damit verbundene Zeit und Mühen und die Demonstrationen zur Durchführung und die intensive wissenschaftliche Auseinandersetzung zur Interpretation aller Ergebnisse, bedanke ich mich sehr ausdrücklich bei **Herrn Dr. Karsten Thiel**.

Allen Mitgliedern der Arbeitsgruppen „Korrosionsschutz und Elektrochemie“ und **„Chemische Kristallographie fester Stoffe“** danke ich sehr für die schöne Zeit und gute Zusammenarbeit sowie die angenehme Arbeitsatmosphäre während der gesamten Arbeitszeit.

DANKSAGUNG

Herrn Dr. Shahram Nouri Shirazi danke ich für seine Hilfestellung bei vielen wissenschaftlichen Fragestellungen und der intensiven Mithilfe am Patent und einem immer offenen Ohr.

Ebenfalls gilt ein Dank an die Mitarbeiter des IFAMs **Herrn Jonas Aniol** und **Herrn Andreas Seiler** für die Durchführung der XPS-Messungen.

Für die Bereitstellung der Röntgen-Pulver-Diffraktometrie-Messanlagen und die dazugehörigen Einführungen am Gerät danke ich ganz herzlich der **AG Gesing** und **AG Fischer** der Universität Bremen.

Frau Naiana Suter, Herrn Juliano Luiz Faccioni, Herrn Benjamin Heim und **Frau Amelie Greif** und **Frau Linda Gätjen** danke ich ebenfalls für die Mühen bei der Durchführung der Zelltests und den damit verbundenen Auswertungen sowie **Herrn PD Dr. Ingo Grunwald** für die Hilfe bei jeglichen biologischen Fragestellungen.

Genauso danke ich **Frau Dr.-Ing. Andrea Berg, Frau Kerstin Lunkwitz** und **Frau Anja Giethmann** für die Hilfestellung bei Mikroskopaufnahmen und speziellen Schleifarbeiten.

Herrn Dr. Urs Haßlinger und **Herrn Dr.-Ing. Martin Ritter** danke ich sehr herzlich für die Erstellung und die Assistenz der EBSD-Messungen.

Für die Hilfe und Unterstützung bei den LIBS-Messungen während des Prozesses danke ich **Herrn Dr. Hauke Brüning** und **Frau Mareike Schlag**.

Ein weiterer Dank gilt **Herrn Karl Woicke** für die Hilfe, Bereitstellung und Anfertigung einiger spezieller Materialien für die praktische Arbeit.

Bei **Ms. Laura Davies** bedanke ich mich sehr herzlich für die Korrektur der englischen Sprache.

Mit ganzem Herzen bedanke ich mich bei **meiner Familie, meinem Lebenspartner und meinen Kommilitonen und Freunden**, die mir während der ganzen Zeit zur Seite standen und ständig ihre Unterstützung zukommen ließen und ebenso immer ein beruhigendes und aufbauendes Wort für mich parat hatten.

LISTE DER PUBLIKATIONEN

Die vorliegende Dissertation wurde auf Grundlage der folgenden drei Publikationen und einem Patent [95], [196], [208], [222] erstellt.

PUBLISHED CONTRIBUTIONS

- [I] A.E.R. Friedemann, Th. M. Gesing, P. Plagemann „Electrochemical rutile and anatase formation on PEO surfaces” Surface & Coatings Technology 315 (2017) 139–149, <https://doi.org/10.1016/j.surfcoat.2017.01.042>
- [II] A.E.R. Friedemann, K. Thiel, Th. M. Gesing, P. Plagemann „Photocatalytic activity of titania films produced with plasma electrolytic oxidation” Surface & Coatings Technology 344 (2018) 710-721, <https://doi.org/10.1016/j.surfcoat.2018.03.049>
- [III] A.E.R. Friedemann, K. Thiel, U. Haßlinger, M. Ritter, Th. M. Gesing, P. Plagemann „Investigations into the structure of PEO-layers” Applied Surface Science 443 (2018) 467–474, doi: <https://doi.org/10.1016/j.apsusc.2018.02.232>
- [IV] Ariane Friedemann, Dr. Malte Burchardt, Dr. Nouri Shirazi, Dr. Thorsten Fladung, Dr. Ingo Grunwald, Dr. Dirk Salz; Patentanmeldung DE 10 2017 111 784.9 „Beschichtetes Substrat mit titanhaltiger Beschichtung und modifizierter Titanoxidbeschichtung“ 2017 applied for

CONFERENCE AND POSTER CONTRIBUTIONS

- a) A. Friedemann, P. Plagemann, Th. M. Gesing, “Plasma electrolytic oxidation of Titanium to form multifunctional porous Titanium dioxide layers”, 24th Annual Meeting of the German Crystallographic Society (DGK), Stuttgart, 2016, Poster Presentation

- b) A. Friedemann, P. Plagemann, Th. M. Gesing, “Plasma electrolytic oxidation of titanium to form multifunctional porous Titanium dioxide layers”, GDCh-Wissenschaftsforum Chemie, Dresden, 2015, Poster Presentation

- c) A. Friedemann, P. Plagemann, Th. M. Gesing “Plasma Electrolytic Oxidation of Titanium to form Multifunctional Porous Titanium Dioxide Layers”, GfKORR-Jahrestagung 2015 'Korrosionsschutz fängt bei der Vorbehandlung an', Frankfurt am Main, 2015, Poster Presentation

- d) A. E. R. Friedemann, K. Thiel, Th. M. Gesing, P. Plagemann “Investigations on the structure of PEO layers on titanium”, 6th Regional Symposium on Electrochemistry of South-East Europe, Hungary Balatonkenese, 2017, oral lecture

- e) A. E. R. Friedemann, K. Thiel, Th. M. Gesing, P. Plagemann “Investigations on the structure of PEO layers on titanium”, 2nd International Conference on Light Materials – Science and Technology (LightMAT 2017) ‘Aluminium, Magnesium, Titanium moving the world’, Bremen, 2017, oral lecture

ABKÜRZUNGSVERZEICHNIS

AC/DC	Alternating current /direct current	MB	Methylene blue
CAE	Constant analyzer energy-mode	PBS	Phosphate buffered saline
CCD	Charged coupled device	PEEK	Polyetheretherketone
CDEM	Channel detection electron multiplier	PEO	Plasma electrolytic oxidation
CVD	Chemical vapor deposition	PET	Polyethylenterephthalate
DAPI	4',6-diamidino-2-phenylindole	PTFE	Polytetrafluorethylene
DASF	Derivation of absorption spectrum fitting	PU	Polyurethane
EBSD	Electron backscatter diffraction	PP	Polypropylene
EDX/EDS	Energy dispersive x-ray spectroscopy	PVD	Physical vapor deposition
FESEM	Field-scanning electron microscope	RGB	Red green and blue colors
FIB	Focused ion beam	RhB/RB	Rhodamine B
HA	Hydroxyapatite	SBF	Simulated body fluid
HAADF	High-angle annular dark field	SEM	Scanning electron microscopy
HF	High frequency	sscm	Standard cubic centimeter per minute
HMDSO	Hexamethyldisiloxane	STEM	Scanning transmission electron microscopy
IR	Infrared	UV-Vis	Ultraviolet-visible light
LMIS	Liquid metal ion source	XPS	Photo electron microscopy
		XRD	X-ray diffraction

TABLE OF CONTENTS

DANKSAGUNG	I
LISTE DER PUBLIKATIONEN	III
ABKÜRZUNGSVERZEICHNIS	V
ZUSAMMENFASSUNG	- 1 -
ABSTRACT	- 5 -
1. INTRODUCTION AND MOTIVATION	- 8 -
2. THEORETICAL BACKGROUND	- 11 -
2.1 Surface treatment of metals	- 11 -
2.1.1 Electrochemical anodization of titanium	- 12 -
2.1.2 Plasma electrolytic oxidation	- 16 -
2.2 Titanium dioxide modifications and their properties	- 21 -
2.3 Photocatalysis	- 24 -
2.3.1 Photocatalytic properties of titanium dioxide and mechanism	- 25 -
2.4 Biocompatibility of biomaterials in medical technology	- 28 -
2.4.1 Titanium and titanium alloys	- 30 -
2.4.2 Polymers	- 31 -
2.4.3 Cell adhesion and cell attachment at biomaterials	- 33 -
3. EXPERIMENTAL PROCEDURE	- 35 -
3.1 Chemicals	- 35 -
3.2 Analytical methods	- 37 -
3.2.1 Scanning electron microscopy (SEM) and focused-ion-beam (FIB)	- 37 -
3.2.2 X-ray diffraction (XRD)	- 37 -
3.2.3 Band gap measurement	- 37 -
3.2.4 X-ray-photoelectron spectroscopy	- 38 -
3.2.5 Electron backscatter diffractometry (EBSD)	- 38 -
3.2.6 RAMAN Spectroscopy	- 38 -
3.2.7 Scanning transmission electron microscopy (STEM)	- 38 -
3.2.8 Physical vapor deposition (PVD)	- 39 -
3.2.9 Fluorescence measurement	- 39 -
3.3 Working regulations	- 40 -
3.3.1 Plasma electrolytic oxidation	- 40 -

3.3.2	Photocatalytic measurement	- 41 -
3.3.3	X-ray diffraction (XRD) and Rietveld refinement	- 41 -
3.3.4	Spectroscopic investigations on the plasma electrolytic discharges	- 41 -
3.3.5	Seeding of cell culture	- 42 -
3.3.6	Cell adhesion with vertical flow assay	- 42 -
4.	RESULTS AND DISCUSSION	- 43 -
	<i>CHAPTER 1: CHARACTERIZATION</i>	- 43 -
4.1	Oxide layer modification by plasma electrolytic oxidation with variation of the electrolytic system	- 43 -
4.1.1	Electrolytic systems	- 43 -
4.1.2	Morphology of the PEO oxide layers	- 45 -
	<i>CHAPTER 2: CRYSTALLINITY</i>	- 52 -
4.2	Crystallinity of PEO oxide layers	- 52 -
4.2.1	Degree of crystallinity and phase composition of PEO-layers	- 52 -
	<i>CHAPTER 3: PHOTOCATLYTIC ACTIVITY</i>	- 57 -
4.3	Photocatalytic activity of PEO-layers	- 57 -
4.3.1	Band gap measurements of PEO-surfaces	- 61 -
4.3.2	Methylene blue/rhodamine B degradation	- 65 -
	<i>CHAPTER 4: BIOCOMPATIBILITY</i>	- 73 -
4.4	Transfer of surface modification using PEO on titanium-coated polymer surfaces	- 73 -
4.4.1	Bonding strength of the polymer/titanium interface	- 74 -
4.4.2	Plasma electrolytic oxidation on titanium coatings on PEEK substrates	- 78 -
4.4.3	Aging resistance of the titanium coating	- 79 -
4.4.4	Cell morphology and settling on PEO-surfaces	- 85 -
	<i>CHAPTER 5: PEO MODEL</i>	- 94 -
4.5	Investigations for the understanding of the PEO process model	- 94 -
4.5.1	Investigations into the oxide layer crystallinity	- 94 -
5.	CONCLUSION	- 106 -
6.	OUTLOOK	- 108 -
7.	BIBLIOGRAPHY	- 110 -
8.	CURRICULUM VITAE	- 126 -

ZUSAMMENFASSUNG

Die plasmaelektrolytische Oxidation (PEO) ist ein zur Erzeugung von stabilen, kompakten, keramikartigen und porösen Oxidschichten etabliertes elektrochemisches Verfahren und wurde im Laufe des 20ten Jahrhunderts vermehrt zur Strukturierung von Metalloberflächen wie Aluminium, Magnesium und Titan herangezogen. Speziell in den Bereichen des Wärmeschutzes und Korrosionsschutzes stieg die Verwendung des Verfahrens im industriellen Maßstab in den letzteren Jahren ebenso stark an wie der Einsatz zu dekorativen Aspekten. Ebenso ist die plasmaelektrolytische Oxidation aufgrund ihrer Möglichkeit der Variation der Oberflächeneigenschaften wie Porosität, Schichtdicke und Oberflächenzusammensetzung besonders für die Medizintechnik und Implantologie interessant geworden. Das PEO-Verfahren ermöglicht es, durch die Entstehung von energiereichen Plasmaentladungen kristalline Oxide, besonders auf Titanoberflächen, zu erzeugen. Diese Titandioxide ermöglichen wiederum die photokatalytische Aktivität der Oberflächen und können ebenso deren Verschleißfestigkeit deutlich steigern. Die ablaufenden physikalischen und chemischen Prozesse sind jedoch sehr komplex und für manche Metalle, wie hier für Titan, noch nicht vollständig verstanden.

Eine der wichtigsten Fragestellungen für das Verständnis der ablaufenden Prozesse ist die Aufschlüsselung ausgesuchter Parameter, wie Elektrolytzusammensetzung, angelegte Spannung und der daraus ableitende Aufbau der Oxidstrukturen. Diese Einflussfaktoren wurden im Rahmen der vorliegenden Arbeit analysiert und der Strukturaufbau ebenso wie Oberflächeneigenschaften genauestens untersucht. Dazu wurden im Rahmen der Arbeit reine Titanwerkstoffe mit verschiedensten elektrolytischen Systemen behandelt, um eine Entschlüsselung der Unterschiede in Struktur, Aufbau und daraus resultierenden Eigenschaften zu ermöglichen.

Deutliche Unterschiede der Oxidschichten in Phasenbildung und Aufbau wurden röntgenographisch und mikroskopisch nachgewiesen. Mit einer Erhöhung der Spannung und der richtigen Auswahl des Elektrolyten konnte der strukturelle Aufbau der Oxidschichten in Porengröße und Porenverteilung sowie Schichtdicken und Grad der Kristallisation der Titandioxidphasen deutlich variiert werden. Der Anteil an kristallinen Oxiden konnte im hohen Maße mit Hilfe dieses Verfahrens durch die Wahl der richtigen Elektrolytzusammensetzung und Steigerung der Spannung erhöht werden.

ZUSAMMENFASSUNG

Mit einer Erhöhung der angelegten Spannung stiegen die Größen der Porenstrukturen und die Oxidschichtdicken signifikant an. Hohe verwendete Spannungen ebenso wie eine hohe Elektrolytleitfähigkeit steuerten zur Bildung von kristallinen Bestandteilen der Phasen Anatas und Rutil bei. Durch die Zugabe von organischen Substanzen ließ sich die Durchbruchsspannung der Plasmaentladungen herabsetzen und der daraus resultierende Energieeintrag im Laufe des Prozesses wurde intensiviert. Durch die hohen freigesetzten thermischen Energien wurde die Umwandlung des erzeugten Titandioxids in die thermodynamisch stabile Phase Rutil begünstigt. Beide polymorphen Modifikationen konnten mit Hilfe der Röntgendiffraktometrie in allen PEO-Oberflächen nachgewiesen werden. Aufgrund der gebildeten kristallinen Titandioxide entstand eine photokatalytische Aktivität der Oxidschichten, welche mittels UV-Vis-Spektroskopie untersucht wurde. Oberflächen mit einem hohen Anteil an Anatas und einer hohen Schichtdicke, sowie Oberflächen mit einem Verhältnis von Anatas zu Rutil von 1:1, zeigten die intensivsten photokatalytischen Eigenschaften. Die kleinen Kristallitgrößen im Bereich von 20 – 30 nm von Anatas und Rutil in Verbindung mit hohen Anteilen des kristallinen TiO_2 wirkten sich weiterhin positiv auf die photokatalytische Aktivität der PEO-Schichten aus. Zudem ergab die Auswertung der Reflektionsspektren mit Hilfe der Tauc und DASF Methode einen direkten Übergang der TiO_2 -Phasen entgegen einer erwarteten indirekten Bandenlücke des TiO_2 . Dies ließ sich auf die kleinen Kristallitgrößen zurückführen, welche einen positiv Einfluss auf die Effizienz der photokatalytischen Eigenschaften der PEO-Oberflächen haben.

Im darauffolgenden Teil der Arbeit wurde die Übertragung der hergestellten Schichten für eine Anwendung in der Implantat-Technik auf polymere Substrate hin untersucht. Eine mit Hilfe des PVD-Verfahrens aufgebraute dünne Titanschicht wurde mittels des PEO-Verfahrens oxidiert und mit der charakteristischen Porenstruktur versehen. Hierfür wurde ein bereits untersuchter Elektrolyt [1,2] zur Steigerung der Biokompatibilität und Bildung von knochenähnlichem Hydroxylapatit verwendet. Die notwendigen Bindungen zur Bildung des Hydroxylapatits konnten folgend mittels XPS-Untersuchungen auf den erzeugten Schichten nachgewiesen werden. Zu Beginn der Untersuchungen ergab sich die Notwendigkeit zur Verbesserung der Haftfestigkeit des Titans auf der polymeren Oberfläche, um eine geeignete Stabilität der PEO-Schichten für den Einbau in den menschlichen Körper zu gewährleisten. Die benötigte Haftfestigkeit konnte mittels einer SiO_2 -Zwischenschicht erzielt werden, welche im verwendeten Stirnabzugstest den gewünschten Kohäsionsbruch im Substrat verursachte.

ZUSAMMENFASSUNG

Die so hergestellten PEO-Schichten auf polymerem Untergrund wurden weiterhin auf ihre Eignung der Zellanwachsung untersucht. Dabei zeigte sich jedoch keine eindeutige Abgrenzung der Zelladhäsion im Vergleich zum reinen Titanwerkstoff zeigte. Es wurde jedoch eine Verbesserung zum reinen polymeren Substrat erzielt. So wurde die Eignung des PEO-Verfahrens zur Modifizierung von polymeren Werkstoffoberflächen und der Verbesserung des Einwachsens in den menschlichen Körper aufgrund einer vermehrten Zelladhäsion im Laufe der Untersuchungen nachgewiesen.

Durch die Ermittlung der Oberflächeneigenschaften und -zusammensetzungen der Oxidschichten wurden diese in ihrem strukturellen Aufbau tiefer greifend untersucht. Ziel war es hierbei, ein besseres Verständnis der Einwirkung der Plasmadurchbrüche auf die Schichtbildung zu erlangen. Mittels Raman-Spektroskopie und der EBSD-Technik wurden die kristallinen Bestandteile innerhalb der gesamten Oxidschicht nachgewiesen und identifiziert. Es zeigte sich, wie auch in den XRD-Messungen ersichtlich, eine Erhöhung der kristallinen TiO_2 -Phasen vom unteren Rand der Oxidschicht bis zur Schichtoberfläche. Des Weiteren wurde der Aufbau der PEO-Oxidschichten mit Hilfe einer detaillierten Analyse mittels STEM-Methode weiter entschlüsselt. Hierdurch wurden große Kristalle im oberen Bereich der Oxidschicht und kleinere Kristalle an der Grenzschicht zum Titansubstrat sichtbar. Diese Bereiche entstanden zum einen durch hohe Energien der Entladungen im späteren Verlauf der Oxidation, wohingegen die kleineren Kristalle am unteren Rand der Oxidschicht mit dem Einwirken der Entladungen bis zum Grund der Oxidschicht zu erklären sind. Rund um die erzeugten Porenstrukturen der Oxidschicht ließen sich amorphe TiO_2 -Bereiche erkennen. Diese amorphen Bereiche führten zu dem Schluss, dass das entstehende TiO_2 während des Prozesses in die flüssige und gasförmige Phase überführt werden kann. Die verminderte Leitfähigkeit in der Gasphase und der umgebende kältere Elektrolyt führten zu einer schnelleren Abkühlung des TiO_2 im Bereich der Porenstrukturen und somit zu einer verminderten Bildung von kristallinen Strukturen.

Die in dieser Arbeit vorgestellten Ergebnisse zeigen die Möglichkeit der Anpassung der Oberflächeneigenschaften, wie Morphologie, Kristallinität und photokatalytische Aktivität von PEO oxidierten Titandioxidschichten in einer Reihe von Anwendungsgebieten. Die Kristallinität der Titandioxide kann mit Hilfe des PEO-Verfahrens gezielt gesteuert werden und hilft die Stabilität, wie auch die photokatalytische Aktivität der Schichten anzupassen. Die Übertragung von dünnen PEO-Schichten auf polymere Substrate ebenso wie die Verbesserung der Haftfestigkeit von Titan auf polymerem Substrat mit einer speziellen

ZUSAMMENFASSUNG

Haftvermittlerschicht konnten erfolgreich erzielt werden. Polymere Substrate werden in der Medizin neben Titan ebenfalls als Implantatwerkstoff eingesetzt, können aber den biokompatiblen Anforderungen oftmals nicht standhalten. Die Verbesserung der Zelladhäsion gegenüber reinen Polymeren, mittels der Aufbringung einer PEO-Schicht, konnte dagegen erfolgreich erzielt werden. Die weiteren intensiven Untersuchungen zum Aufbau der PEO-Oxidschichten führte zu einem besseren Verständnis des Prozesses und der Einwirkungen der Plasmen Spezies auf die gesamte Schicht. Das Modell der plasmaelektrolytischen Oxidation wurde damit auf Titanwerkstoffe erweitert.

ABSTRACT

Plasma electrolytic oxidation (PEO) is an established electrochemical process to produce of stable, compact, ceramic-like and porous oxide layers and was increasingly used during the 20th century for the structuring of metal surfaces such as aluminum, magnesium and titanium. On an industrial scale, especially in the fields of thermal protection and corrosion protection, the applications of the process have increased significantly in recent years, such as its use for decorative aspects. Likewise, PEO has become interesting for medical technology and implantology due to the diversity of its varying surface properties such as porosity, layer thickness and surface composition. The PEO-process makes it possible, especially on titanium surfaces, to produce crystalline oxides through the formation of high-energy plasma discharges. These titanium dioxides can in turn enable the photocatalytic activity of the surfaces and significantly increase their wear resistance. However, the ongoing physical and chemical processes are very complex and for some metals, as here for titanium, are not fully understood.

One of the most important aspects to understanding the involved process events is the investigation into used parameters, such as electrolyte composition, applied voltage, and the resulting structure of the oxide layer. These influencing factors were analyzed in the present work, and both the structures and the surface properties were examined in detail. In this work, pure titanium materials were treated with various electrolytic systems to enable a decoding of differences in structure and the resulting properties. Distinct differences between the oxide layers in terms of phase formation and structure could be demonstrated by x-ray diffraction and microscopic examination. By increasing the voltage and choosing the right electrolyte, the structure of the oxide layers could be varied with regard to pore size and distribution as well as in layer thickness and the degree of crystallinity of the titanium dioxide phases. Using this method, the proportion of crystalline oxides in the PEO-layers could be adjusted through the right electrolyte composition and an increase in the applied voltage.

With the increase in the applied voltage, the size of the pore structures and the thickness of the oxide layers also sharply increased. A high voltage as well as a high conductivity of the electrolyte contributed to the growth of the crystalline components anatase and rutile. Through the addition of organic substances, the breakdown voltage of the plasma discharges could be reduced and the resulting energy input was intensified during the process, whereby the high energy release promoted the conversion of the titanium dioxide into the

ABSTRACT

thermodynamically stable rutile phase. Both polymorphs could be detected by x-ray diffraction in all PEO-surfaces. Due to the resulting crystalline photoactive titanium dioxides, the photocatalytic activity of the oxide layers was investigated using UV-Vis reflectance spectroscopy. Surfaces with a high content of anatase and a high layer thickness, as well as surfaces with an anatase to rutile ratio of 1:1, showed the most intense photocatalytic properties. The small average crystallite sizes, in a range of 20 - 30 nm, of anatase and rutile in combination with high levels of crystalline TiO₂ had a positive effect on the photocatalytic activity of the PEO-layers. Furthermore, the evaluation of the reflection spectra with the help of the TAUC and DASF methods revealed a direct transition of the TiO₂ phases against an expected indirect band gap of TiO₂. This can be attributed to the small crystallite sizes, which have a positive influence on the efficiency of the photocatalytic properties of the PEO-surfaces.

In the following part of this work, the transfer of the prepared layers to a polymeric substrate for use in implant technology was investigated. A thin titanium layer was applied by means of the PVD processes so that it could be oxidized with plasma electrolytic oxidation and the characteristic pore structure could be transferred. For this purpose, a previously investigated electrolyte [1,2] was used to increase the biocompatibility and formation of bone-like hydroxyapatite. The necessary bonds for the formation of the hydroxyapatite were subsequently detected on the produced layers by means of XPS measurement. At the beginning of the investigations, there was a need to improve the adhesion of titanium to the polymeric surface to ensure proper stability of the PEO-layers for incorporation into the human body. The required adhesive strength could be achieved with an SiO₂ interlayer, which caused a desired cohesive failure in the substrate in the pull-off test used here. The as prepared PEO-layers on a polymeric substrate were further investigated for their cell growth suitability, with no clear improvement of cell adhesion compared to the pure titanium material. However, an improvement could be achieved compared to the pure polymeric substrate. Thus, during the course of the studies, it was possible to demonstrate the suitability of the PEO-process for modifying polymeric material surfaces and improving human ingrowth due to increased cell adhesion.

By determining the surface properties and compositions of the oxide layers, it was possible to investigate these in more depth regarding their structural design, thus gaining a better understanding of the effect of the plasma discharges. Using Raman spectroscopy and the EBSD technique, the crystalline constituents could be detected and identified within the entire

ABSTRACT

oxide layer. Analogical to the XRD measurements, an increase in crystalline TiO₂ phases was found from the lower part of the oxide layer to the surface of the layer. Furthermore, the structure of the PEO oxide layers could be decrypted because of a detailed analysis using the STEM method, whereby large crystals in the upper area of the oxide layer and smaller crystals at the boundary layer to the titanium substrate could be visualized. For the first case, these areas were created by the high energies of the discharges in the later course of the oxidation, whereas the smaller crystals at the lower part of the oxide layer could be explained by the effects of the discharges as far as the bottom of the oxide layer. Amorphous TiO₂ was detected around the generated pore structures of the oxide layer. These amorphous regions led to the conclusion that the resulting TiO₂ can be converted into the liquid and gaseous phases during the process. The reduced conductivity in the gaseous phase and the surrounding colder electrolyte led to a faster cooling of the TiO₂ in the area of the pore structures and thus to a reduced formation of crystalline structures.

The results presented in this work demonstrate the possibility of adapting the surface properties, such as morphology, crystallinity, and photocatalytic activity of PEO oxidized titanium dioxide layers for a variety of applications. The crystallinity of the titanium dioxides can be selectively controlled and helps to adjust the stability as well as the photocatalytic activity of the layers. The transfer of thin PEO-layers to polymeric substrates, as well as the improvement of the adhesion of titanium to polymeric substrates with a special adhesive layer, has thus been successfully achieved. In addition to titanium, polymer substrates are also used as an implant material in medicine, but they often cannot withstand the biocompatibility requirements. The improvement of cell adhesion to pure polymers by applying a PEO-layer was successfully achieved. Further intensive investigations into the structure of the PEO oxide layers led to a better understanding of the process and the effects of the plasma species on the entire layer. This helped to expand the model of plasma electrolytic oxidation on titanium materials.

1. INTRODUCTION AND MOTIVATION

Plasma electrolytic oxidation (PEO) offers many possibilities to modify surfaces of lightweight metals, especially aluminum, titanium, and their alloys. Due to its variety of properties, such as biocompatibility and corrosion protection, titanium was chosen for the investigations in this study. Titanium forms compact and stable oxide films for several applications. Using PEO it is possible to form structured, thick and crystalline oxide films. One of the most important effects for the different film properties is the composition of the electrolytic system [3–5]. Different mixtures of acids and the applied voltages can form typical crater-like structures [6,7]. The type of the electrolytic system has an influence not only on the structure, but also on the crystallinity of the titanium dioxide phases contained. The effects of the electrolytic system and the applied voltage on the crystallinity of plasma electrolytic oxidized samples are two important factors for tuning the multiple properties of PEO-layers. Because of the high energies from the micro-discharges on the anode surface, the crystallinity of the formed oxide layer can be controlled. The crystallinity leads to an interesting property of TiO₂, namely the photocatalytic activity. With the aim of producing an improved biocompatibility and a possible photocatalytic activity of TiO₂, This study attempted to adjust and optimize the morphology and crystallinity of PEO-surfaces using different electrolytic systems.

Due to its many useful properties, photo-catalysis has been the focus of scientific research. The high levels of energy consumption and the development of ecological disposal methods makes photo-catalysis necessary for new investigations as a gentle method for removing organic or inorganic pollutants [8–10] and to create renewable energies [11–14]. In this field, semiconducting compounds have proven to be particularly effective, whereby TiO₂ is the most successful photo-catalyst due to its high photon-absorbing property. A number of parameters are important for photocatalytic activity such as phase composition, crystallite size and particle size, surface area, crystallinity, or impurities like the absorption and desorption of molecules [15,16]. Anatase seems to be the most active polymorph of TiO₂, while the influence of rutile has also investigated over the last few years [17–22]. Most studies use nano-particulate crystalline powder samples with a high surface area, which enable a high absorption of photons [23,24]. The combination of crystallinity and a high surface area is purposefully used to strengthen photocatalytic activity. The photocatalytic activity of TiO₂ on crystalline PEO-surfaces has been reported in several publications [4,7,25–27]. However, the effect of the electrolytic system on the crystallinity and the resulting photocatalytic activity

INTRODUCTION AND MOTIVATION

has not yet been fully investigated. The plasma electrolytic oxidation produces titania layers with a high porosity and crystallinity of anatase and rutile phases. The porous surfaces indicate an enlarged specific surface area, which leads to a strong potential to form photocatalytically active surfaces. Over the last few years, photo-catalysis and PEO have moved to the front of the discussion [4,25–28]. Therefore, the photocatalytic activity of different PEO-surfaces with different contents of crystalline phases and surface morphologies are to be investigated.

Due to their range of properties, titanium materials are widely used in medicine as implantation materials. Its thin, natural oxide layer can have a positive effect on cell-adhesion [29]. With a controlled structuring of the titanium dioxide layers using PEO, the biocompatible properties can be improved even further [30,31]. In some medical applications, the brittle and rough properties of titanium polymer materials are used for implantation. The PEO-process modifies the surface of titanium into a pore-rich structured surface with an increased surface area and oxide layer thickness. With increased pore size and layer thickness the cell adhesion rate should be improved through the production of increased mechanical anchoring points. The combination of flexible polymers with the good properties of titanium through a metallization of the surface has, already been reported by Devine et al. [32], Han et al. [33], and Cook et al. [34]. The coating with titanium with different supporting materials and a subsequent PEO-surface treatment was reported by Martin et al. [35]. An application of TiO₂ coatings without a surface treatment on PEEK implants has been published [36–38], but the combination of PEO-treatment on thin titanium layers on polymer substrates has not been fully investigated and will be examined in this study.

Plasma electrolytic oxidation is a complex and difficult process and it is not yet fully understood for titanium materials. Because of the multiple varieties of the properties of titanium dioxide and its modifications, it is increasingly important to go deeper into the whole PEO-process to understand oxide layer formation. In general, the process is based on the interaction at the solid-liquid interface and on some electrical, mechanical, and thermal theories [39–41]. The mechanical effects depend on the defects in the formed oxide layer, while the thermal effects are due to the high current densities that are formed by the plasma discharges during the process. These effects lead to an increased electrical conductivity [42]. The discharge formation has been described by previous researchers as glow discharge electrolysis, electronic avalanche, and electronic tunneling [41,43–45]. Also, the state of the appearance of the plasma discharges has been investigated in several reports in detail for

INTRODUCTION AND MOTIVATION

aluminum and magnesium alloys [46–49]. In this case, the investigations into PEO plasma discharges, especially for titanium and its alloys, are still quite new, and some models for layer growth in order to obtain oxide layer formation has been reported in the last few years [50–53]. Using the different PEO-layers produced here, the entire inner oxide structure can be considered in order to more closely understand the complex influence of the plasma and the oxide layer formation during the PEO-process.

2. THEORETICAL BACKGROUND

2.1 Surface treatment of metals

The targeted adaptation of the properties of a metal or metallic material, like its adhesion promotion, corrosion resistance, or improved biocompatibility, can be achieved through a variety of surface treatments. Various methods and techniques are used for this purpose (Tab. 1).

Tab. 1 Surface treatment methods for the structuring of metal surfaces and the magnitude of the modification [54–56]

Type of treatment	Process	Modification of surface
Mechanically	grinding	100 μm - 1 mm
	polishing	
	sandblasting	
Physically	PVD/CVD coating (sputtering)	0.2 - 50 μm
	laser, electron beam	
Chemically	plasma etching	Up to 100 nm
	anodization	
	ion implantation	
	sol-gel-coating, dip-coating	

The structures of surfaces can be roughened using a mechanical method, but the adjustment of the chemical composition of the surface is not possible, therefore a combination of chemical and physical surface treatment methods must be used [55]. Where mechanical methods cause structuring through the action of force onto the surface, metal surfaces are modified by thermal, kinetic, or electrical energies [29] in a physical treatment by applying layers or coatings. Thin layers of atoms, ions, or molecules are applied to the surface by gas phase deposition, and hence evaporation or sputtering, where they can react with the atoms of the crystal lattice of the metal and thus bind to the surface. By means of these thin-film technologies, high-purity coatings with a targeted chemical composition can be produced in a vacuum. These can be, on the one hand, merely decorative, but functional layers for protection against corrosion or wear protection can also be achieved. The adhesion strengths and layer thicknesses are markedly higher in contrast to the chemical surface treatment [56]. Chemical surface treatments, such as sol-gel coatings or electrochemical treatments are based on the reaction of the metal substrate with used medium, whereby wet-chemical processes through oxidizing reactions of the metal with an acid or lye are the most established ones. Various electrolytes, such as HNO_3 , H_2SO_4 , HCl , NaOH , KOH as well as additions of HF , are used for the production of thin, porous layers [29]. In such electrochemical processes, the metals are connected into the system as anode (Fig. 1), and the surface is treated by applying a

THEORETICAL BACKGROUND

voltage between the working electrode (anode) and a counter electrode (cathode). Hereby, the conversion of the metal-substrate-ions into a very hard, scratch-resistant metal oxide layer occurs [57]. Through the electrolyte, the generated ion-flux allows the growth of an oxide layer and the associated change in the topography [55].

2.1.1 Electrochemical anodization of titanium

Electrochemical processes with oxidizing reactions of the metal surface produced by a foreign current are summarized by the term "anodizing" or "anodization". This method is mainly used for aluminum, but the valve metals magnesium, zinc and titanium, and their alloys, can also be used. By adjusting the different parameters, such as the electrolyte or electrical parameters (voltage, current) used, layer thickness, composition, and morphology can be varied significantly.

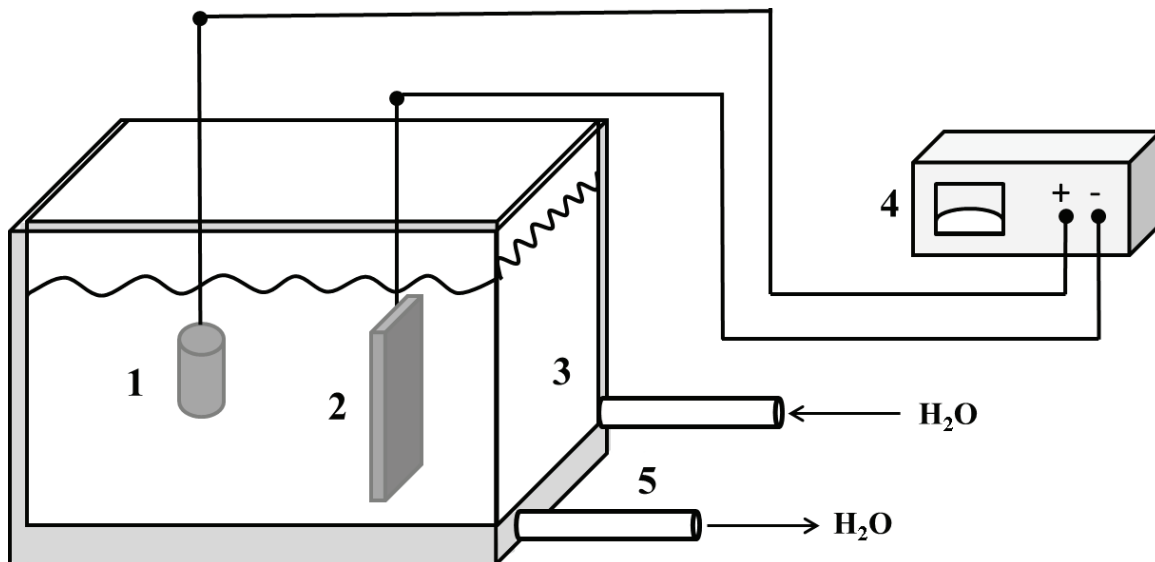


Fig. 1 Schematic illustration of a classical bath anodization with two electrode circuits with (1) a working electrode (anode) (2) counter electrode (cathode) (3) aqueous electrolyte bath (4) DC power supply, voltage source, potentiostat, and (5) water cooling

These valve metals have the property of forming a natural oxide layer a few nanometers thick at the atmosphere, which can be significantly increased through the anodization process. The method of anodization also includes the method of "eloxation", which is especially applied to aluminum and is derived from the abbreviation "eloxal" (electrolytic oxidation of aluminum). The reactions at the anode and cathode are shown in Fig. 2 [57].

THEORETICAL BACKGROUND

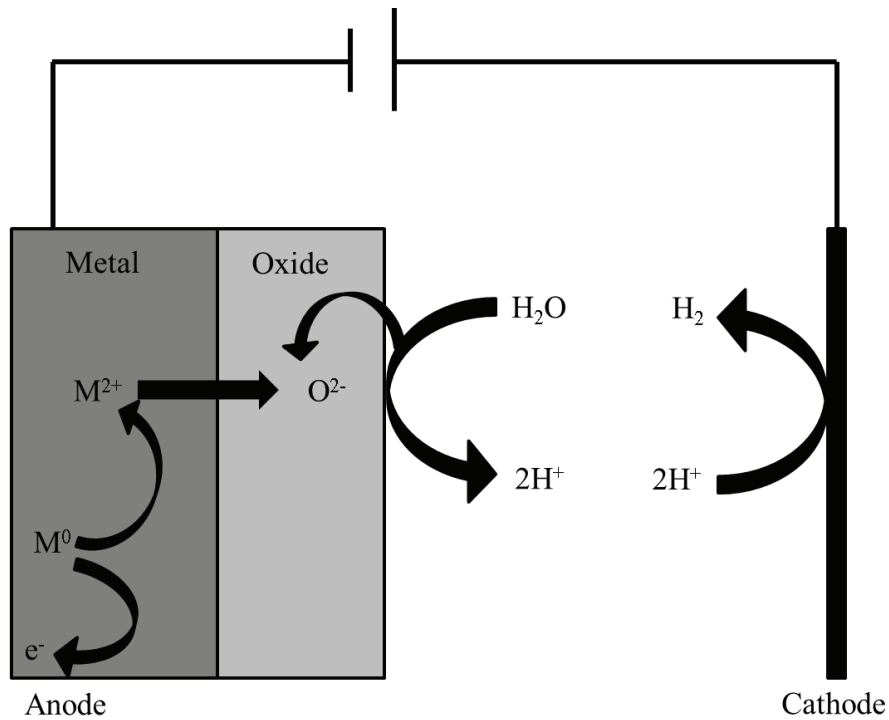
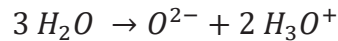
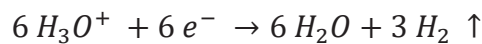
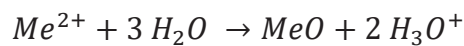


Fig. 2 Illustration of oxide growth in an acidic electrolyte and the reaction processes at the anode surface and the reactions at the cathode surface, according to [58]

Anode reactions:



Cathode reactions:



The thickness x of the oxide layer depends on the potential or the applied voltage ΔU , on the duration t of anodization and on temperature T . The voltage difference across the oxide results in an electric field strength E , which regulates the mass transport during the process. The current density i decreases with time as a result of the decreasing field strength of the growing oxide layer until the outgoing reaction almost comes to a stop ($A, \beta = \text{const.}$) [58].

$$i = A \cdot e^{\beta \cdot E_{Oxide}}$$

$$E(t) = \frac{\Delta U}{x(t)}$$

THEORETICAL BACKGROUND

In electrochemistry, a distinction is made between active and passivated materials that tend to form oxide layers (Fig. 3). Both material groups undergo different electrochemical reactions. In both cases, the anodic current density increases sharply in the first region and an active dissolution of the metal takes place. In the case of passivated substances, an adsorption of dissolution products on the surface begins until it is saturated in the second region and the current density reaches a maximum. These adsorbates form a solid oxide layer and the current strength drops sharply until a passive layer is formed. In the third area (passive area), the resolution of the metal is reduced. The current strengths for active materials remain virtually constant in these areas and only increase with increasing potential [59].

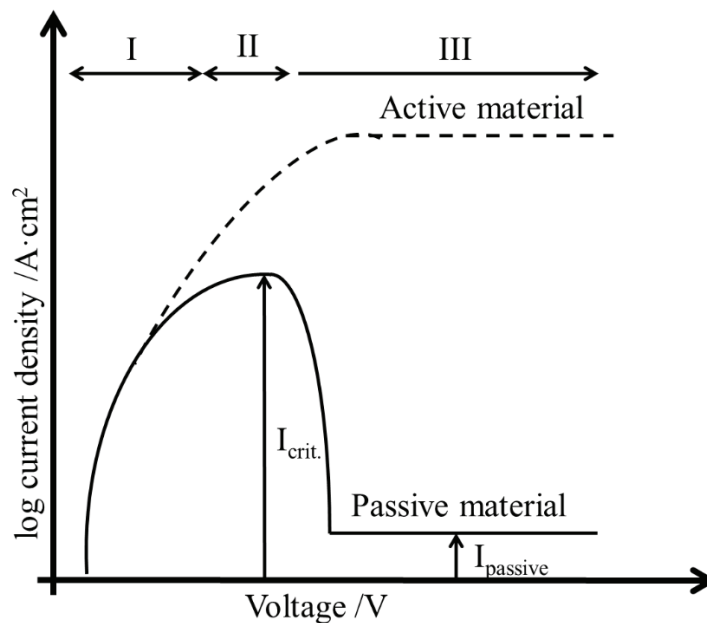


Fig. 3 Current-density-potential-curve of active and passive materials and the three stages of the anodizing process according to [59]

An increase in the specific surface area can be achieved through a variety of different anodizing processes. One of these possibilities is the production of a highly porous layer by means of nano-structuring, the result is, referred to as "nanotubes". The electrochemical formation of such nano-porous layers is mainly applied to aluminum, but more recently to titanium materials as well [60–62]. These nanotubes are open at the surface of the material and are closed at the bottom. The basic structure is highly ordered, and the diameter and wall thickness have the same value for all tubes. Due to this regularity, the specific surface area greatly increases. To produce this controlled, porous structure, the electrolyte fractions of fluorides are added in order to ensure an equilibrium between anodic oxide layer formation and chemical dissolution. The reactions that take place are shown in Fig. 4 for the example of titanium:

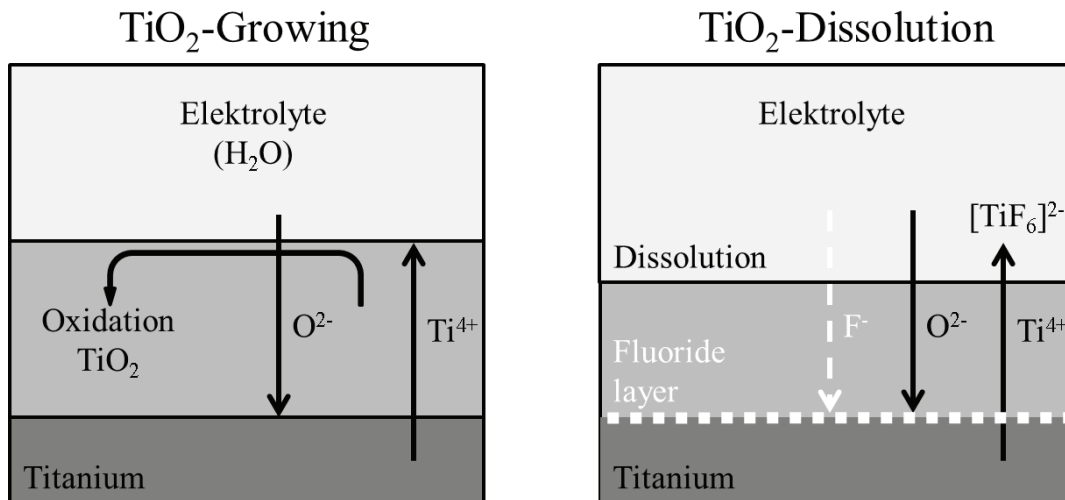


Fig. 4 Growing and dissolution of the oxide layer in fluoride-containing electrolytes with the transport of mobile ions through the oxide layer, according to [63]

Due to the simultaneous formation and dissolution, a new increase in the current density is generated in the current-density-potential curve. After the formation of a barrier layer, the local dissolution of the oxide layer and the formation of randomly arranged pores occur. After some time, an equilibrium of the current between the pores occurs and a self-organized growth of the nanotube layers results [63]. In Fig. 5, the individual phases of the formation of the nanotubes are shown.

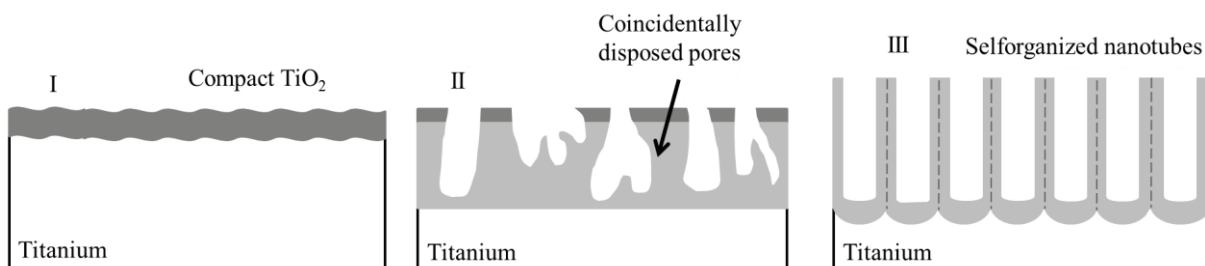


Fig. 5 Three typical phases of the formation of a TiO₂ nanotube layer with the three typical forming processes and the final self-organization according to [63], (I) first stage of forming an amorphous and compact oxide layer, (II) growth of an oxide layer and the formation of pore structures and defects in the layer, (III) self-organization of TiO₂ during the anodization process

Such structured and organized layers also have a positive influence on the biocompatibility of the surfaces, depending on crystallinity and morphology, because these accelerate the formation of hydroxyapatite [64]. The relatively "new" established method of plasma electrolytic oxidation (PEO), with high voltages of up to 1000 V, high layer thicknesses of up to 100 μm and a very high porosity of the surface, is a special case of anodizing like the formation of nanotubes. In contrast to the nanotubes, however, there is no dissolution of the formed oxide layer during plasma electrolytic oxidation and thus there is a continuous growth of these layers.

THEORETICAL BACKGROUND

2.1.2 Plasma electrolytic oxidation

In addition to anodization, another special method exists to apply oxide layers to metals. In contrast to the anodization process, plasma electrolytic oxidation (PEO), also known as micro arc oxidation (MAO), anodic spark deposition (ASD), and plasma chemical oxidation (PCO), is a high-voltage anodic oxidation process for the surface modification of lightweight and valve metals like aluminum, zirconium, magnesium, and titanium because these metals can form adherent and electrically isolating anodic oxide films [65]. The PEO-process has a long history of development. The technique was first mentioned in 1880 by Sluginov et al. [66] and then further developed in 1937 by Schulze and Betz [67] for the development of capacitors. Up until this century the discharge phenomena had not been studied in detail. Only in the course of the 1960s was the PEO-process used to form oxide layers on different metals [68–71]. During the 1980s, the poor quality of the produced coatings was improved with more efficient electrolytic systems and the use of a pulsed current instead of DC processes. This made the commercialization of the PEO-process possible by companies such as Keronite (UK) [72], Metaker[®] (Germany) [73] and Magoxide-coat (Germany) [74] on light-weight metals [53,75,76]. In the last few years, the PEO-process has received more attention for its use on light-weight metals in transportation, the construction industry, and aerospace because of its ability to form stable oxides and high layer thicknesses, improving corrosion protection [77–79]. PEO combines chemical, electrochemical, and thermodynamic reactions with thermal diffusions in an aqueous solution. The local temperatures at the surfaces can reach 10^3 and 10^4 K due to the plasma micro-discharges [47,53,80]. The process is typically carried out in a range of voltage from 100 V up to 1000 V, and the setup is similar to a common anodization setup as seen in Fig. 1. The setup consists of a typical power supply in DC- or AC-mode. Similar to the “normal” anodization processes a two-electrode-setup is used. The detailed mechanism of the PEO-process, is not fully understand, but there exists a principle overview of the four typical stages during the plasma coating process, as seen in Fig. 6 [47,65,81,82].

THEORETICAL BACKGROUND

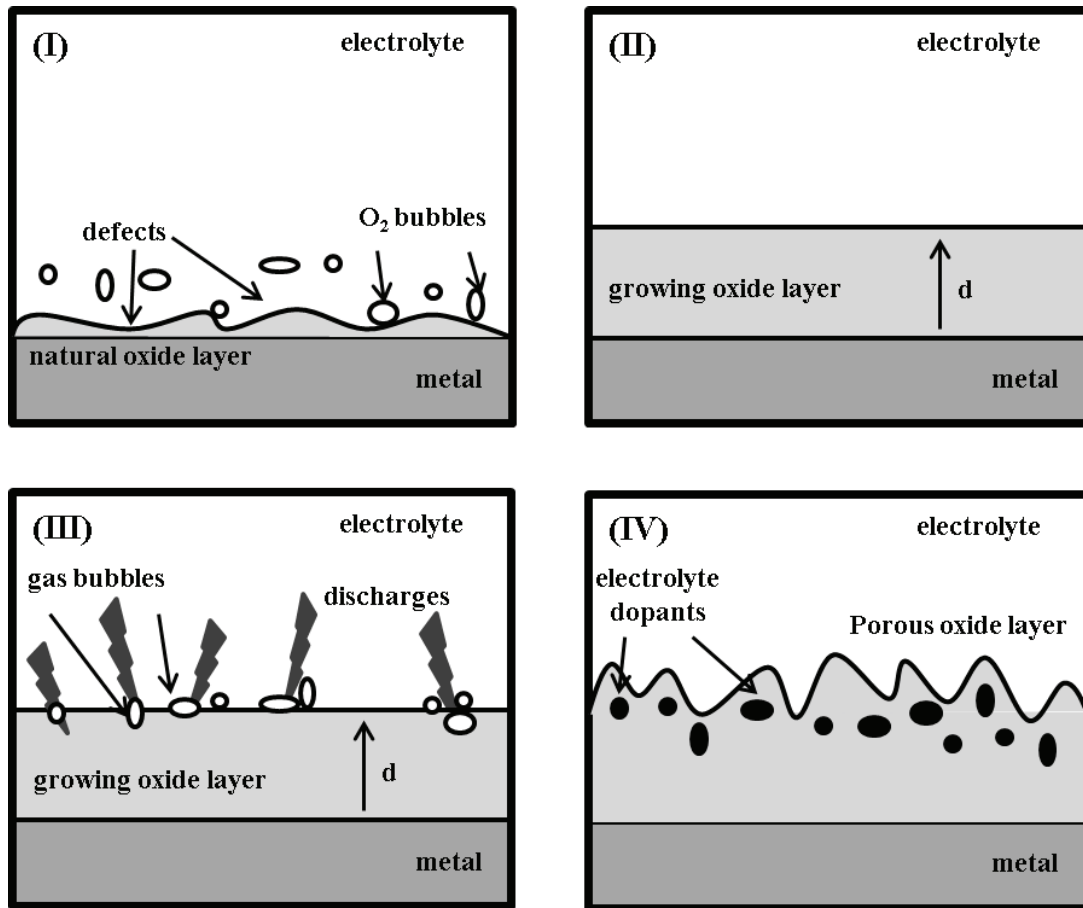


Fig. 6 Schematic representation of the four different stages of the PEO-process, according to [65] and described further in the text

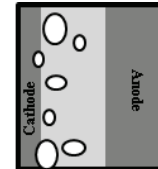
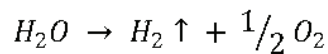
- Stage I** During the first stage, the voltage increases up to the breakdown voltage of the used system and a thin insulating oxide film grows on the surface of the chosen metal. Some oxygen bubbles form around the natural anodic oxide layer, similar to the traditional anodizing process.
- Stage II** When the applied voltage reaches a critical point of the breakdown voltage an electric breakdown takes place, due to the growing oxide layer and its isolating property. The oxide film growth rate then decreases. In the growing layer, some regions are prone to breakdowns because of a shrinking resistance due to some defects.
- Stage III** In the third stage, there is a spark discharge formation with small white sparks occurring randomly over the whole anode surface, while there is also an increase in the current density. The evaporation of the metal and the electrolyte enables the formation of the ceramic-like PEO-treated surface. With an increase in voltage, the sparks grow and change their color from white to orange or red, whereby the micro-arcs become plasma arcs.

THEORETICAL BACKGROUND

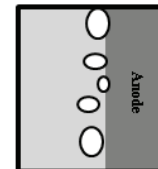
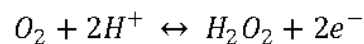
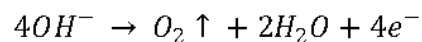
Stage IV The gas evolution of the metal and the electrolyte contents leads to a porous morphology and thermal cracking of the oxide film. The structure of the PEO-coating has a two-layered morphology with a barrier inner layer and a porous outer layer. The thickness varies from 1 to 100 μm [65,76,83].

These four phases of PEO reflect the basic understanding of the mechanism based on electrical breakdowns at the boundary layer from the solid to the liquid electrolyte. Thermal electron emission causes, discharges on the dielectric oxide surface. Tunneling effects and the ionization of other constituents from the electrolyte or the metal lead to an electron current along the dielectrics. This impact ionization leads to the formation of the plasmas, which in turn leads to the formation of a characteristic crater-like surface structure [84]. For aluminum substrates three types of discharges can be explained. A-type and C-type discharges are gaseous discharges in the micro pores, whereby A-types occur at the surface and C-types occur in the deeper pores. B-type discharges, on the other hand, are dielectric breakdowns in the electric field [83,85], that occur in the later stage with a high intensity. The individual reactions of the plasma electrolytic oxidation at the anode and the cathode can be represented as in Fig. 7:

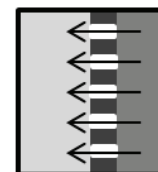
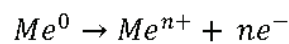
Decomposition of water:



Evolution of O_2 and H_2O_2 :



Metal dissolution:



Formation of oxide layer:

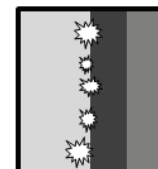
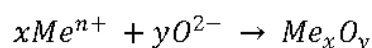


Fig. 7 Reactions during PEO-treatment of metals with a schematic illustration according to [52]

THEORETICAL BACKGROUND

The PEO-coating grows due to different mechanisms. There is outward growth from the substrate towards the electrolyte and inner growth with a transfer of oxygen ions into the coating which react with the metal cations. There, they form the oxide ceramic coating [52]. If different ions, like calcium- or phosphate ions, are dissolved in the electrolyte, these are incorporated into the oxide layer due to high temperatures and electric breakdowns. These high temperatures follow from the strong and intense discharges in the final fourth stage of the PEO-process, forming discharge channels where the electrolyte contents move into the oxide under an electric field. Due to the high temperatures, the substrate material melts and diffuses into the channels and is solidified by the cooler electrolyte. The gaseous phases escape through the channels to the surface and result in the characteristically crater-like structures (volcano). All complex processes, such as, melting, solidification, and evaporation, occur simultaneously during PEO and form the volcano-like structures at the surfaces [47,83,86–90]. The PEO-morphology for aluminum, magnesium, and titanium is shown in Fig. 8.

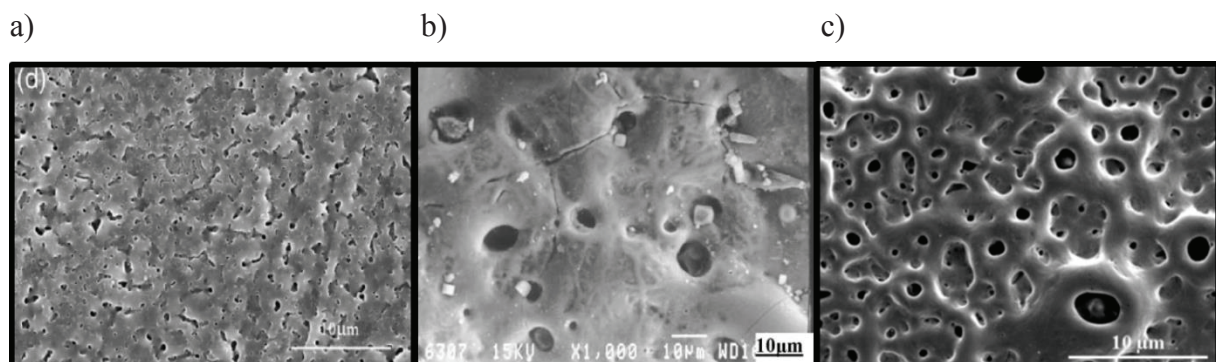


Fig. 8 SEM micrographs of PEO-coatings formed on a) magnesium alloy AZ31 [91], b) aluminum alloy 2024 [92], and c) titanium grade 1 [93]

Due to the high temperatures and high cooling rates at the coating/substrate interface, crystalline parts can form in the oxide layer [94]. The PEO-process and the coating morphology are dependent on such parameters as electrolyte composition, substrate material, and current mode (voltage). The electrolyte composition is one of the most important influences on the PEO-coatings. The electrolyte induces the metal passivation and transmits the necessary energy for oxidation. The components of the electrolyte, which will be incorporated into the coating, are also necessary for the corresponding properties of the oxide layer. Morphology, adhesion strength, micro-hardness, and tribological properties can be affected by the electrolyte [1,95–98]. Organic or inorganic additives are used to improve the conductivity and the coating thickness and thus corrosion protection. Coatings containing TiO_2 , ZrO_2 , and Al_2O_3 nanoparticles have a higher adhesion to the substrate as well as, wear

THEORETICAL BACKGROUND

resistance and scratch hardness [99–102]. The multiple properties of the PEO-coatings and how they are affected are shown in Tab. 2.

Tab. 2 The properties and the impacts of PEO-layers

Property of the PEO-coating	Influence/ impact	Literature
Mechanical	Phase composition/phase transformation	[103]
	Crystallinity	[104]
Wear resistance	Porosity	[105]
	Hardness	
Corrosion resistance	Thickness of barrier layer	[106]
	Number, size of defects	
	Porosity, size of pores	
Thermal protection	Additives	[107]

Also, the composition of the substrate can affect the properties of the PEO-coating with a different coating thickness and porosity level [106]. The PEO-coating contains three different layers, from the bottom of the substrate (1), to a thin inner layer (barrier layer) (2), followed by an intermediate layer, known as the “functional layer” (3). The functional layer has a sub-micrometer porosity, which is the result of dissolved and trapped oxygen in the molten oxide layer, see Fig. 9 [108].

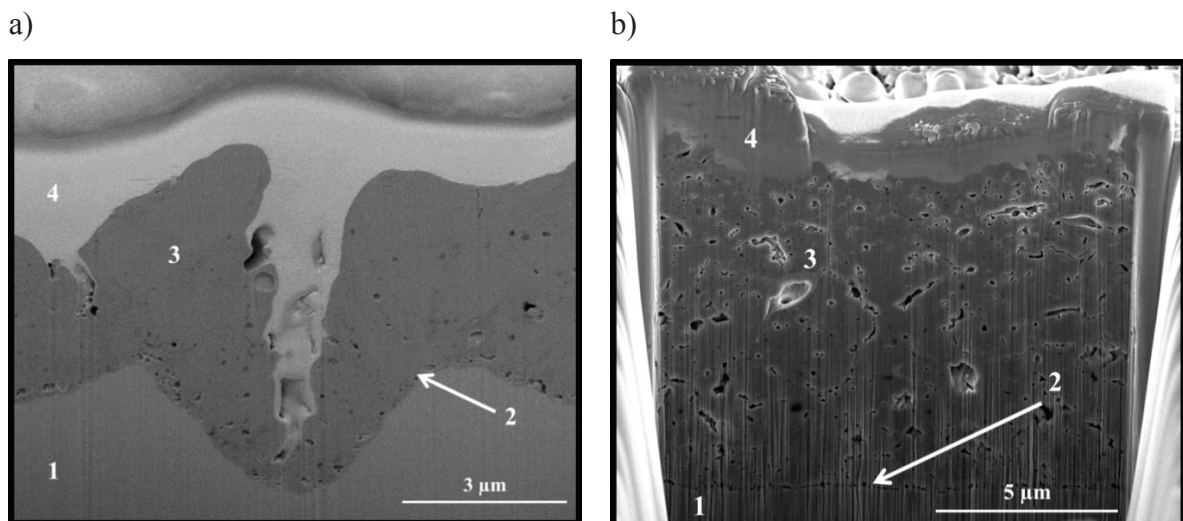


Fig. 9 Focused ion beam cross-section micrographs of a typical PEO titanium dioxide layer described in the literature; PEO TiO₂ layer with three components: a) Titanium dioxide PEO-layer with characteristic pore structure, b) porous titanium dioxide PEO-layer; (1) titanium substrate (2) barrier layer (3) functional layer (4) conductive Pt-layer from the FIB-preparation setup

2.2 Titanium dioxide modifications and their properties

Titanium and its alloys form a thin protective oxide layer under atmospheric conditions. The composition of these thin oxide layers consists of largely amorphous, unordered titanium dioxide, while specifically produced oxide layers can consist of crystalline phases of titanium dioxide [109,110]. Amorphous TiO₂ crystallizes at an approximate temperature of 350 °C. In nature, titanium dioxide exists in three crystalline modifications, namely anatase, rutile, and brookite. All three modifications have distorted oxygen octahedra, while anatase and rutile are associated with the tetrahedral crystal system and brookite with orthorhombic. The oxygen atoms in rutile form a hexagonal closest packing, whereas in anatase and brookite they form a cubic closest packing. The polymorph rutile is the thermodynamically stable form, in contrast to the other two modifications, due to its structure. Brookite and anatase can thereby convert to rutile after a temperature of 750 °C [111–113].

Tab. 3 Crystallographic parameter of the titanium dioxide phases [113]

Phase	Crystal system	Space group	Lattice parameter /Å			Frequent crystal surface
			a	b	c	
Anatase	Tetragonal	I4 ₁ /amd	3.78	3.78	9.51	[0 0 1] [1 1 0] [0 1 0]
Rutile	Tetragonal	P4 ₂ /mnm	4.59	4.59	2.96	[1 1 0] [0 1 0]
Brookite	Orthorhombic	Pbca	9.174	5.45	5.14	-

In Tab. 3 the crystal parameters associated with the oxide modifications is shown and the unit cells are shown in Fig. 10 to Fig. 12 [113]. Due to the natural stability and advantageous properties, only anatase and rutile are of technical relevance. The different crystal structures of the polymorphs are shown in the x-ray diffraction pattern in Fig. 13 by their reflection positions.

THEORETICAL BACKGROUND

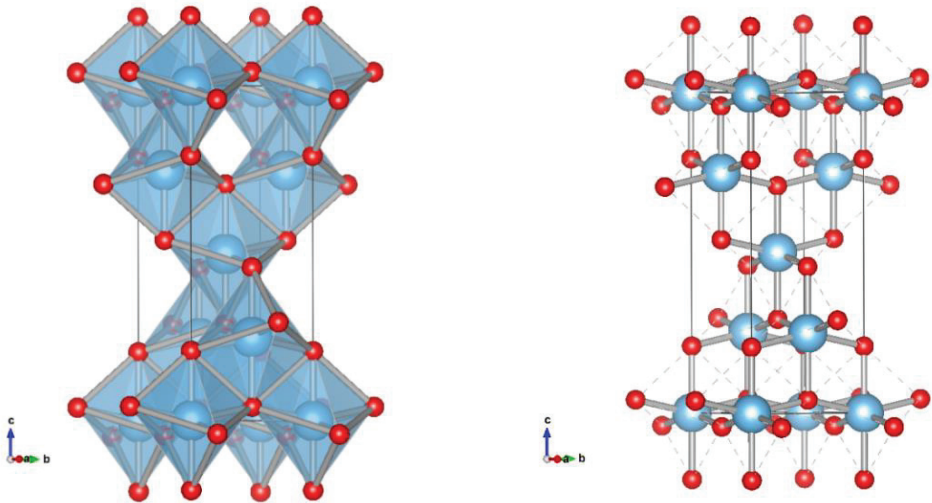


Fig. 10 Illustration of one unit cell and the crystal structure of anatase, (left) polyhedral structure (right) atomic bonding structure

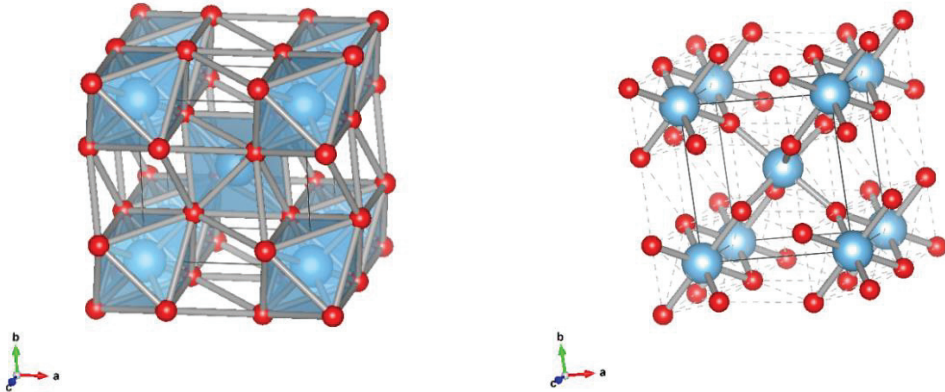


Fig. 11 Illustration of one unit cell and the crystal structure of rutile, (left) polyhedral structure (right) atomic bonding structure

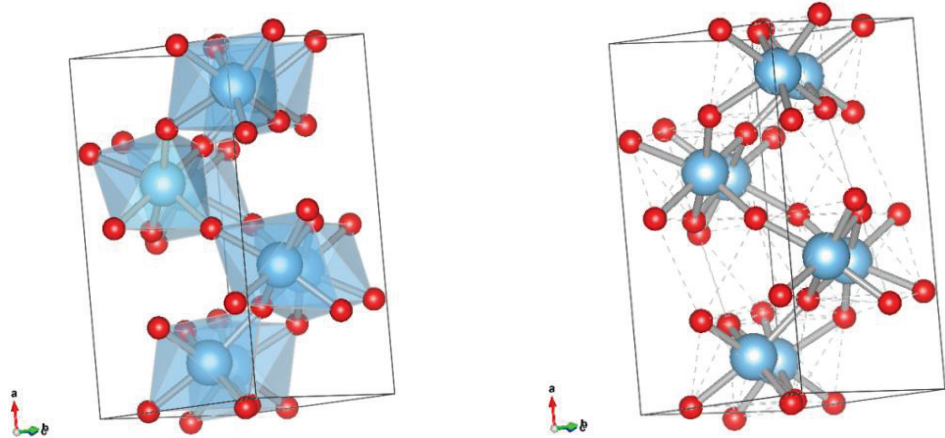


Fig. 12 Illustration of one unit cell and the crystal structure of brookite, (left) polyhedral structure (right) atomic bonding structure

THEORETICAL BACKGROUND

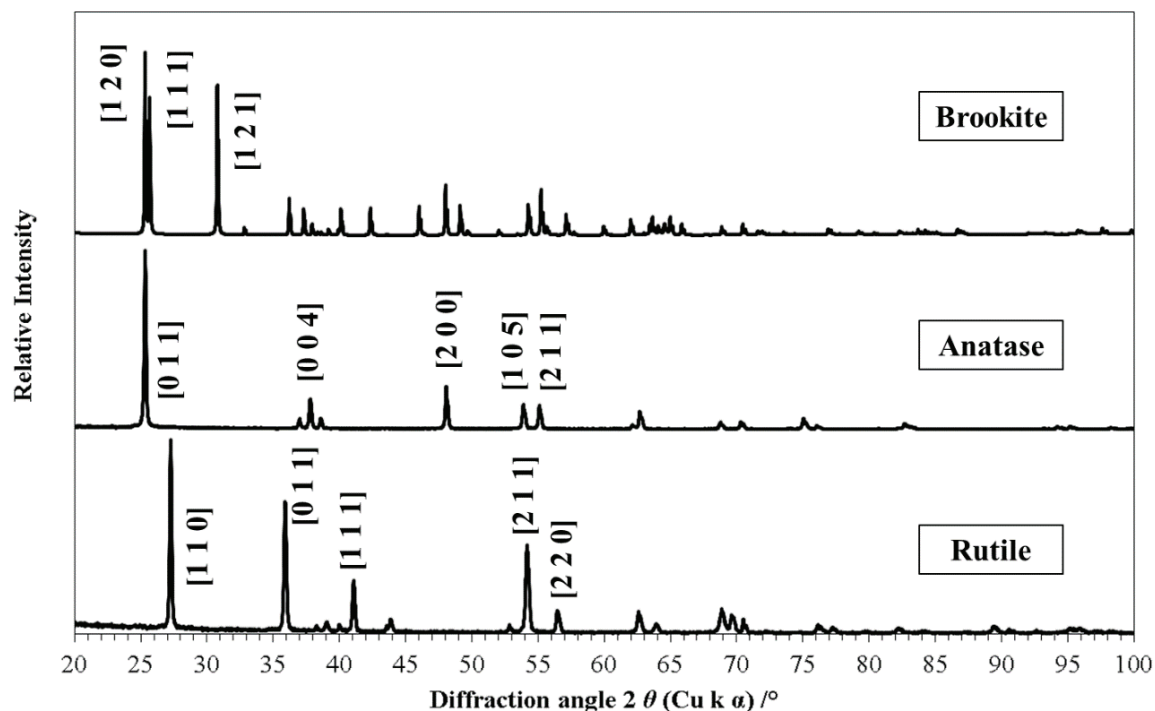


Fig. 13 XRD-diagram of the three main TiO₂-phases with their main reflection signals and its crystal orientation marked at the associated reflections in square brackets

The two oxide modifications anatase and rutile are stable in their crystal structure and do not undergo any changes under normal conditions, but both polymorphs, particularly anatase, exhibit a certain photocatalytic activity, which is important in many applications in medicine as well as in the construction industry. Furthermore, the three oxide modifications differ in their density, while rutile is the only thermodynamically stable form (anatase: 3.88 g/cm³, rutile: 4.26 g/cm³, brookite: 4.1 g/cm³). In addition to its high oxidation capability, TiO₂ is generally chemically inert and non-toxic, and in addition to its photocatalytic properties it is widely used as a pigment in paints, textiles, toothpastes, cosmetics, foodstuffs, and medical products. Because of the high refractive indices of anatase ($n = 2.55$) and rutile ($n = 2.7$), both modifications are used as white pigments in such application areas [111]. The most commonly used commercially available titanium dioxide mixture is AEROXIDE® TiO₂ P25 from Evonik. It consists of 70 - 80% anatase and 20 - 30% of rutile and is produced industrially by flame pyrolysis of titanium tetrachloride (TiCl₄). Due to the high photocatalytic activity of the product, it is used as a standard in many studies [114,115].

2.3 Photocatalysis

In general, photochemical reactions are those in which the necessary activation energy is not required in the form of heat but in the form of radiation as light. Among such light-induced reactions are, on the one hand, chemiluminescent reactions and, on the other hand, physically supported processes of fluorescence, phosphorescence, photovoltaics, and photoelectrochemical reactions such as photocatalysis. Photoreactions play one of the most important roles on Earth. They are the basis of life as they are used in the process of photosynthesis to form and decompose organic molecules. In many subsequent studies, small photochemical reactions, such as the reddish discoloration of nitric acid by sunlight, the blackening of silver chloride, the development of oxygen from carbonic acid by plant parts, and numerous photoinduced reactions for the synthesis of organic compounds, were discovered. Most of the time, thermally induced reactions have predominated in chemical research [116].

It was only at the beginning of the 20th century that photochemistry achieved a clear advance with a focus on the versatile applications of photocatalysis. The term photocatalysis is defined as a change or an initiation of a chemical reaction in the presence of a catalyst by means of ultraviolet, visible, or infrared radiation [117,118]. A substance is referred to as a catalyst when it accelerates a chemical reaction without being consumed as well as reduces the free activation enthalpy [119]. After the radiation has been absorbed, the catalyst is found in an excited state and is thus capable of transforming the reaction partners. In this state, the catalyst is repeatedly capable of reacting with other substances and regenerates itself. Semiconductor materials, which have a band gap between the valence and the conduction band, have proven to be particularly useful for this purpose [120].

The process of photocatalysis has become the focus of scientific research over the years due to the high level of energy consumption and its associated pollution in the world as well as emerging ecological developments. The fields of the degradation reactions of organic and inorganic contaminants with the help of sunlight and the generation of renewable energies play an important role [8,9,11,12,121]. Hereby, not only can various compounds be degraded by a photocatalytic reaction, pollutants can also be removed from the air or water [10,13,14,122]. In most cases, the catalysts can be improved in their activity and properties by doping, modifying, or changes to particle size [123–125]. Doped compounds of hybrid metal oxides have a certain photocatalytic activity because of a shift in the band gaps [123,126]. The

THEORETICAL BACKGROUND

possibilities of the application of photocatalysts are very diverse and are not limited to the environmental and energy industry, but are also used in medicine and surface engineering. In medicine, the photocatalytic effect is not only used in the removal of bacteria [4,127–129], it is also used for cancer cell treatment [130,131]. The versatile application of photocatalytic degradation is also used in surface technology for self-cleaning surfaces or so-called anti-fog coatings [15]. A large number of materials and their composites are available for these applications, including zirconium oxides, tungsten-molybdenum oxides and, the most common material, titanium dioxide [123,126].

2.3.1 Photocatalytic properties of titanium dioxide and mechanism

The photocatalytic activity of TiO₂ was first reported by Fujishima et al. [132,133] in the form of various applications for the splitting of water and other inorganic and organic substances [15]. At the end of the last century, between 1995 and the beginning of the 2000s, TiO₂ was increasingly the subject of research on the basis of a large number of emerging publications and patents in the field of pollutant degradation [134,135]. The photocatalytic properties of titanium dioxide are due to its semiconducting properties. The electrons of the semiconductors can pass into an excited state by the absorption of photons from light quanta of the near IR- and visible UV-region, resulting in a so-called “hole” to the electron in the ground state. Inorganic semiconductor compounds have, in addition to localized atomic orbitals, crystal orbitals, which are called energy bands, and these contain the energy states of the electrons. In these energy bands there are forbidden zones for the occupation by electrons, which are called “gaps”. Depending on the number of freely available valence electrons, corresponding valence bands V_B are formed. Similarly, there are empty conduction bands C_B . These “bands” have a defined distance with a certain value ($E_g = xy$ eV), depending on the solid. As the number of atoms increases, E_g becomes smaller and the absorption shifts into the longer wavelength. The following Tab. 4 shows some values for typical semiconductors.

Tab. 4 Values for the photocatalytic activity and associated band gaps of selected inorganic semiconductors [116]

semiconductor	Valence band V_B/V vs. NHE	Conduction band L_B/V vs. NHE	E_g /eV	λ /nm
TiO ₂	+ 2.6	-0.6	3.2	390
CdS	+ 1.5	-0.9	2.4	520
ZnS	+ 1.84	-1.84	3.6	340

THEORETICAL BACKGROUND

The top valence band edge is responsible for the oxidation potential of a substance and the lowest conduction band edge is responsible for the reduction potential [116]. During the absorption of photons, electrons are excited from the uppermost occupied valence band into the lowest unoccupied conduction band into a higher energy state. This way an electron-hole-pair will be generated in the valence band (exciton). The absorption of the radiation energy must correspond to the energy of the band gap E_g of the substance. The band gaps of the two active oxide modifications of TiO_2 have a relatively small value of $E_g = 3.2$ eV for anatase and $E_g = 3.0$ eV for rutile [15]. The photocatalysis and the ligand model as well as the related reactions of TiO_2 are shown in Fig. 14 and Fig. 15.

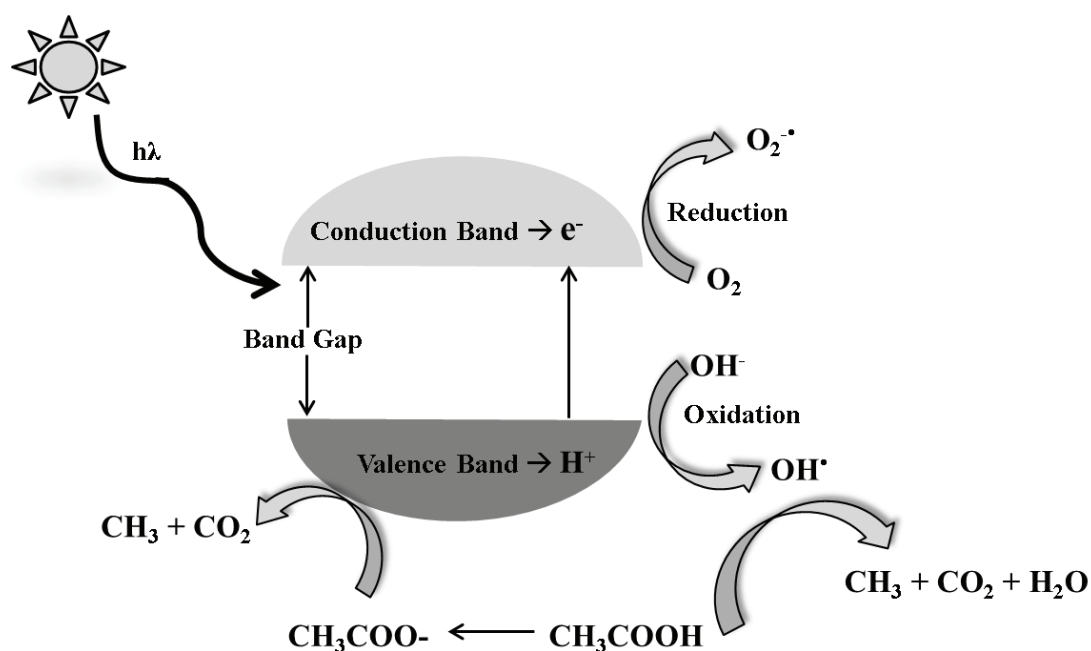


Fig. 14 Illustration of the band gap model of titanium dioxide in the presence of oxygen, water and organic substances, according to [136]

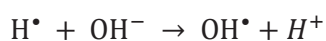
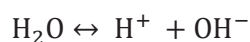
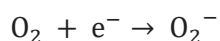
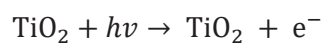


Fig. 15 Possible reactions of the photocatalysis of titanium dioxide [19]

THEORETICAL BACKGROUND

In the series of semiconductor compounds, titanium dioxide (TiO_2) has emerged as one of the most promising photocatalysts due to its high oxidation ability and the rapid formation of excitons (electron-hole-pairs). Due to these defects in the valence band, the resulting positive charge is available for the adsorption of organic or inorganic compounds. It is formed a high redox potential of +2.53 V vs. SHE (standard hydrogen electrode) in the band gap, and the electrons only have a potential of -0.52 V vs. SHE. This leads to the splitting of water and the formation of hydroxyl ions and the oxidation to hydroxyl radicals (OH^\bullet). This leads to the generation of active superperoxide radicals ($\text{O}_2^{\bullet-}$) and the formation of hydrogen peroxide. The formed radicals can thus directly react with adsorbed compounds at the surface (heterogeneous catalysis) or initiate the decomposition of gaseous compounds from the gaseous phase (homogeneous catalysis) [19,137]. A schematic representation of such catalysis is shown in Fig. 16.

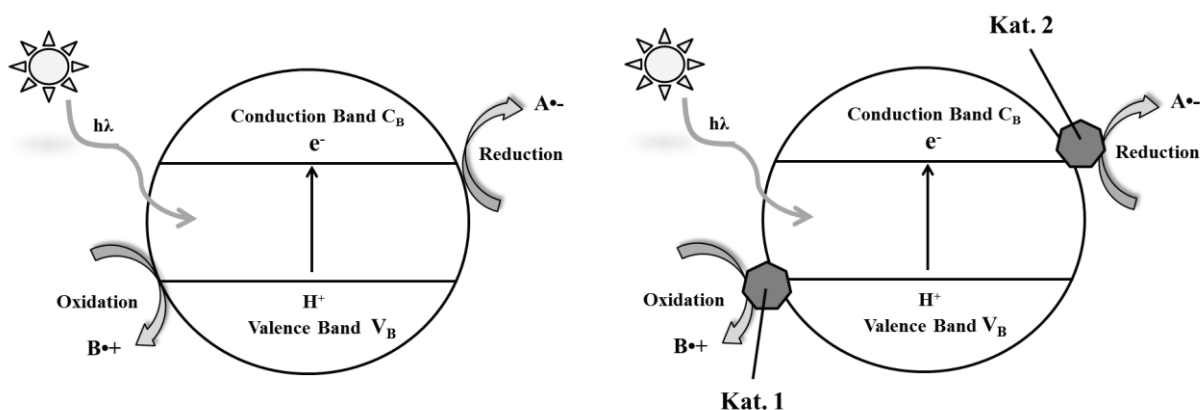


Fig. 16 Schematic representation of photocatalysis on semiconductor particles with the formation of donors B and acceptors A at the band gaps (left) homogeneous catalysis and (right) heterogeneous catalysis with two selective catalysts according to [116,138]

The energy level of anatase often corresponds to the redox potential of the adsorbed molecules, whereby electrons can be transmitted more easily. Therefore, anatase is mainly used for photocatalytic applications. The influence of rutile and brookite has only been partially investigated [139,140]. The commercially available AEROXIDE® TiO_2 P25 from Evonik with a composition of approx. 80% anatase and 20% rutile and a very small particle size of 21 – 35 nm is used as an excellently photocatalytically active substance. For photocatalytic applications, many anatase-rich substances exist with a wide range of particle sizes of 5 nm to 35 nm and a composition of anatase to rutile of 100% anatase to 75% anatase and 25% rutile (AEROXIDE® TiO_2 P25), which strongly influences the photocatalytic activity.

2.4 Biocompatibility of biomaterials in medical technology

Biomaterials are those materials that have a similarity or a certain affinity to a living organism and may include a wide range of materials that come into contact with different biological areas [141]. An important aspect of biomaterials is their biocompatibility or biotolerance. They are in direct contact with the living organism and its electrolytes, such as blood, hard, and soft tissue as well as the cells. If the biocompatibility of a material is available or can be produced, then that material is suitable for a use in the human organism. Biocompatibility includes, on the one hand, high corrosion and wear resistance and, on the other hand, an affinity with the surrounding cells to ensure their growth [29,142]. The most common places for the application of biomaterials are hard tissue, primarily bones, which can be replaced by supporting implants. The trend towards higher ages across the world will lead to an increased need for tissue or organ replacement in humans over the next decades, while the need for biological implants due to worsening bone quality and increasing life expectancy is increasing annually in Germany alone [143,144].

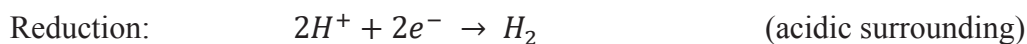
As early as in 1775, an implant in the form of a wire was documented for the fixation of an upper arm bone. In 1840, the American surgeon John Murrey Carnochan replaced part of a human jawbone with a piece of wood. During 19th century, the first investigations into the compatibility of metals were carried out. In 1906, for the first time, materials such as silver, magnesium, zinc, ivory, and gold were used to correct slight bone defects, and the noble metals produced the fewest problems [54,145]. The first publication on the use of prostheses was in 1939 in the “*Journal of Bone and Joint Surgery*” [146]. Owing to long-lasting high stresses and aging, hard tissue such as bones, teeth, and hip- or knee joints can be damaged and are being replaced by medicine in modern times using many interventions. In this case, the materials used may not be damaged or altered by the endogenous substances. Hereby, a large number of chemical, physical, or biological factors play key roles (see Tab. 5) [147].

Tab. 5 Requirements and influencing factors for an implant for use in the body [148]

Physically	Chemically	Biologically
Flexibility	Phase transition	Bioadhesion
Hardness	Toxicity (inert, poisoning)	Biocorrosion (toxic ions)
Resistance	Metallosis	Compatibility with tissues and fluids
Durability	Allergy	

THEORETICAL BACKGROUND

The compatibility and stability of the implants depend on the structure and surface properties due to the adsorption of cell-specific proteins. On the other hand, they are also dependent on subjective factors such as the body fluids (saliva, blood, lymph) and habits of the patient. Basic, acidic and salty constituents in body fluids and foodstuffs can initiate or catalyze electrolytic processes on metallic materials. At the interfaces of the tissue to the substrate surface, chemical interactions can take place through the exchange of ions following partial reactions:



In order to prevent these effects, different actions are taken on the different implant materials, such as coatings, additives in alloys, or certain surface treatments [149]. A large number of biomaterials can be classified according to their degree of biocompatibility (Tab. 6).

Tab. 6 Classification of biomaterials and their application in medical technology [145]

Biomaterial	Biodynamic	Application
Ceramics		
Aluminiumoxide	Bioinert	Middle ear implants Dental implants
Hydroxyapatite	Bioactive	Filling material for bone defects Dental implants
Metals		
FeCrNi-steel alloy	Biotolerant	Bone plates- and screws
CoCr-alloy		Wires
Titanium and titanium-alloys	Bioconductive	Implants with bone contact Coating of implants
Polymers		
Polypropylene (PP)	Bioinert	Sutures
Polyethylenterephthalate (PET)	Bioinert	Artificial blood vessels
Polyurethane (PU)		
Polytetrafluorethylene (PTFE)		

THEORETICAL BACKGROUND

A material is always classified as "bioinert" when it does not release any influencing or toxic substances into the body, and this should be the case for any implant. A material is referred to as "bioconductive" if an integration of the tissue into the structure of the material takes place, while a "bioactive" material is completely enclosed by the tissue. These ratings are important, depending on the application of the implants, to promote the patient's healing process and well-being [145]. In medical technology, various biomaterials such as metals, ceramics, and polymers are used that fulfill these biological requirements. Due to their metallic and non-metallic constituents and the associated crystalline structure, ceramics have a strong ionic bond, which makes them very popular for implants with a high pressure and wear resistance. These include the bone-like hydroxyapatite HA ($\text{Ca}_5(\text{PO}_4)_3\text{OH}$), which has a similar chemical composition to the mineral phase of bone (60 - 70%) and the tooth enamel (98%) [150].

2.4.1 Titanium and titanium alloys

Metals and various metal alloys are important components in implant preparation and are always used when a high mechanical resistance is required. All metals consist of crystallites, which are arranged in a specific crystal lattice and their composition, size and arrangement in this lattice determine the mechanical properties. The deformability and alloying properties of a metal are further determined by the free moving electrons within the crystal lattice [150]. Not only pure metals are used in medical technology, there is also a wide variety of alloys that are selected according to the application due to the multitude of adjustable properties.

Titanium and its alloys have emerged as very versatile materials due to their very high biocompatibility, which makes their integration into the organism very easy. In the 1950s, titanium was used as an implant material in medicine. Since the middle of the last century, titanium has also been used outside the aerospace industry due to its high modulus of elasticity and corrosion resistance [151]. The alloys TiAl6V4 and TiAl6Nb7 and pure titanium (cp-Ti, grade 1 and 2) have proven to be suitable biomaterials. On the titanium metal surface different species can be generated, which can facilitate the absorption of different molecules (Fig. 17). These processes can be accelerated by methods for surface modification, whereby, instead of a thin amorphous oxide layer, also crystalline layers can be produced from the various oxide polymorphs anatase, rutile, or brookite.

THEORETICAL BACKGROUND

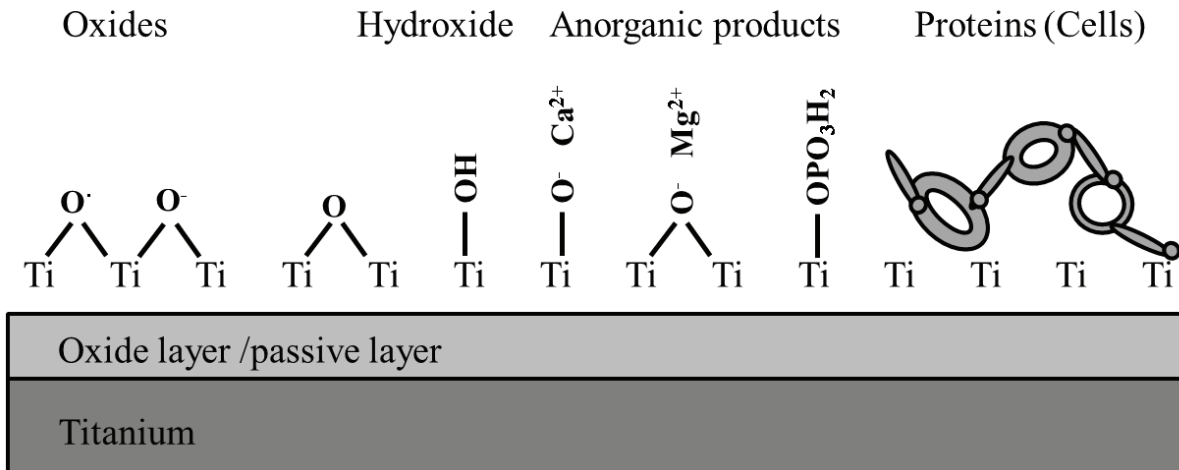


Fig. 17 Formation of possible products on titanium oxide layers with inorganic and organic substances

2.4.2 Polymers

Polymers are molecules that are generated from a mostly covalent bonding of building blocks. These building blocks are called monomers and consist of hydrocarbon chains. These monomers are linked in a continuous repeating unit to form a chain with the number n (*degree of polymerization*). A typical sequence is shown in Fig. 18. There is no exact definition for the number of repeating units n , but this number must be large enough so that the addition of another unit does not change the physical or chemical properties of the material [152].

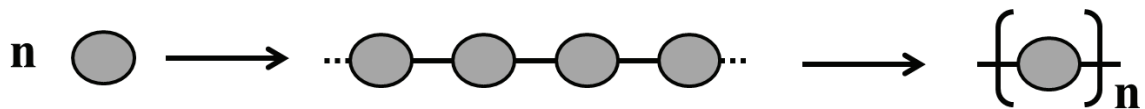


Fig. 18 Schematic illustration of a polymer structure with a theoretical monomer and structural linkage according to [152]

The most common materials, such as metals and ceramics, have a relatively high weight and very low deformability, which is not suitable for some applications where a heavy loading and mobility of the implant are required. Therefore, and because of their similarity to natural-type biopolymers, some polymeric materials have also been used. The first combination, an implant of polytetrafluorethylene and 316L stainless steel, was developed in 1960 by J. Charnley [150]. The biocompatibility of polymeric materials is determined for the most part by their functional groups, and their structure from mostly simpler structural units. In contrast, the human body consists of very complex biopolymers such as proteins, DNA/RNA and polysaccharides, which often makes integration into the body very difficult. Therefore, medically used polymers should have sufficient mechanical strength and sterilization and be as free as possible of non-toxic additives [147,153]. The classification of the polymeric

THEORETICAL BACKGROUND

materials (Tab. 7) is diverse and can be used and classified according to their properties in various areas.

Tab. 7 Classification of polymers and application in medical technology [154,155]

Polymer classification	Polymer	Properties	Application
Thermoplastic	Polyethylene	Linear	Membrane
		Flowable	Blood vessel replacement
		Flexible	
Duroplastic	Amorphous silicones	Strongly cross-linked	Dentistry
	Epoxide resins	Hard	Joint replacement
	Polyester-, phenol-, amino-resins	Brittle	
Elastomer	Silicones	Low cross-linkage	Tubes
	Polyurethane		Catheters

A special high-performance polymer with very high biocompatibility and good mechanical, thermal, and chemical properties is polyetheretherketone (PEEK). Due to this variety of properties, PEEK has also recently been used for the first time in medical technology [156]. PEEK belongs to the class of thermoplastics and is a very tough crystalline polymer with a high melting temperature, for this group, of 607 K. The good mechanical properties of the polymer are maintained even at very high temperatures, which make it very flexible in processing. The water absorption in the polymer is very low in comparison to other thermoplastics. Another important point for medical technology is its high resistance to solvents and strong acids, which makes it very stable and interesting for incorporation into the human body, where a high resistance to any body fluids is required. PEEK also has a high tensile strength and impact resistance as well as a strong resistance against hydrolysis (sterilization/ autoclaving) at high temperatures due to its low water absorption. PEEK is produced by polycondensation by two synthetic routes, One of is shown in Fig. 19.

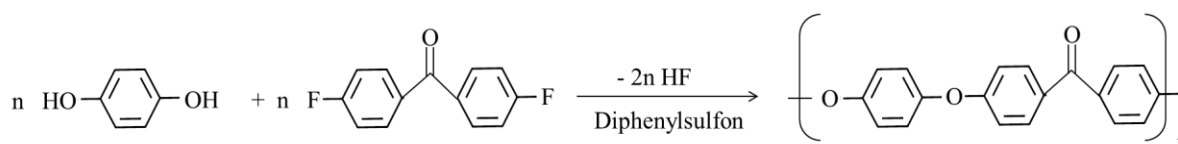


Fig. 19 Schematic illustration of the most common production of PEEK by nucleophilic substitution of hydroquinone and 4,4-difluorobenzophenone according to [157]

THEORETICAL BACKGROUND

PEEK can be prepared by nucleophilic aromatic substitution or by electrophilic substitution on the aromatic (Friedel-Crafts acylation) and is further processed by injection molding and extrusion. Due to its poor solubility, very high temperatures of 573 K to 673 K are used for processing and synthesis. The cooling rates during the processes are designed to be slow in order to increase the crystallinity and biocompatibility [158].

2.4.3 Cell adhesion and cell attachment at biomaterials

Cells have a variety of components that play an important role in the communication between the cell and the adjacent materials and ensure the absorption of proteins, the transport of liquid, and the mechanical attachment of the cell. One part of these components are the receptors, which are responsible for binding specific molecules and directing the signals to the body. After signal processing, proteins are adsorbed onto the entire surface of the substrate to be grown and in most cases the structure determines the strength of the adhesion [159]. The adhesive strength can be strongly influenced by the following factors:

- Chemical binding of the signaling substances and proteins (covalent, ionic bond)
- Electrostatic interaction
- Hydrogen bonding and hydrophilic groups (-OH, -COOH, -NH₂)
- Hydrophobic groups (wettability and contact angle)
- Van der Waals forces

Cell binding on surfaces can be strongly influenced and strengthened by a high hydrophilicity and positively charged groups or hydroxyl and oxygen groups. In addition to these properties, the surface topography with a defined porosity can also favor the strength of cell attachment. Porous structures increase the specific surface area of the substrate and allow the possibility of cell adhesion [160]. The modification of a surface can be carried out by various techniques by means of texturing, either dependently through the base material or independently by various surface structuring methods, with a suitable coating on the surface. By applying a coating, the properties of the biomaterial are to be maintained, while only the interfacial properties, such as adsorption, corrosion resistance, or electrical properties, are varied or improved. This could be achieved, for example, by coating with the metal titanium or its modification titanium dioxide, with the adhesion strength of the coating being one of the requirements. Not only must a mechanical anchoring between the base material and the coating be produced, the chemical bonds between the two substrates must also be created [161]. The binding of tissue to a surface is based exclusively on mechanical interlocking,

THEORETICAL BACKGROUND

whereby the structuring at the micrometer scale can have a positive effect on the growth behavior [55,162]. Likewise, depositions of hydroxyapatite layers on the surfaces of the biomaterials have a strong influence on successful ingrowth into the human body and are state of the art in a large number of publications [163–165]. Several physical methods such as plasma spraying [166], dip coating [167] or ion implantation [168], can be used to apply these bioactive layers. Chemical and electrochemical processes can also be used to deposit apatite compounds by means of the sol-gel processes [169] as well as electrophoresis [170], electrocrystallization [171] and plasma electrolytic oxidation [2,172–174] (see 2.1.2).

EXPERIMENTAL PROCEDURE

3. EXPERIMENTAL PROCEDURE

3.1 Chemicals

All technical chemicals were in quality p. a. and were used in the process without prior purification. The reagents for the bioanalytical investigation of the surfaces were available in the quality required for these studies until ultrapure (see Tab.8 and Tab.9). The commercially purchased titanium and polymer substrates were used in the so-called grade 1 and medical grade, respectively.

Tab. 8 Used chemicals and declaration of purity and manufacturer

Substance	Chemical formula	Purity
SurTec 152 ¹ (alkaline degreasing)	-	< 5% Fatty alcohol ethoxylate 20% Na ₂ CO ₃ < 5% Cocooil aminox ethylate
Turco 5578 ² (alkaline stains)	-	10-30% NaOH 1-10% Triethanol amine 1-10% Sodium gluconate
Sulfuric acid ³	H ₂ SO ₄	95 - 97%
Phosphoric acid ³	H ₃ PO ₄	85%
2-propanol (iso-propanol) ³	C ₃ H ₈ O	99,9%
Ethanol ³	C ₂ H ₆ O	99%
Calcium acetate ⁴	Ca(C ₂ H ₃ O ₂) ₂	≥ 99%
Sodium-β-glycerophosphate	NaC ₃ H ₇ O ₆ P	-
Sodium chloride ³	NaCl	min. 99,9%
Sodium tartrate ⁴	C ₄ H ₄ Na ₂ O ₆	≥99%
Sodium hydroxide ¹⁰	NaOH	Mind. 99%
Sodium hydrogen carbonate ⁹	NaHCO ₃	-
Potassium chloride ⁸	KCl	> 99,5%
Di-potassium hydrogen phosphate ³	K ₂ HPO ₄	mind. 98 - 100,5%
Magnesium chloride ⁹	MgCl	-
Calcium chloride ⁹	CaCl	98%
Sodium sulfate ³	NaSO ₄	p.A.
Tris(hydromethyl)aminomethane ⁴	NH ₂ C(CH ₂ OH) ₃	≥ 99,9%
Hydrochloric acid ⁹	HCl	37%

EXPERIMENTAL PROCEDURE

Tab. 9 Substances and reagents of the bioanalytical investigations with their manufacturer's instructions and purity

Substance	Composition
Mc Coy's 5A with L-Glutamine ⁵	Osteoblasts MG-63
RPMI 1640 with L-Glutamine ⁵	Mouse fibroblasts L929
Phosphate buffer saline solution (PBS) ⁵	140 mM NaCl 10 mM Na ₂ HPO ₄ × 2H ₂ O 2.7 mM KCl 1.8 mM KH ₂ PO ₄
NucBlue® Live ReadyProbes™ Reagent (R37605) ⁶	Nuclear blue: Hoechst 33342 0.1 – 1.0% (w/v)
Trypsin solution 10x (porcine pancreas) ⁴	2.5% solution of 1:250 tryptic activity (quality level: GMP)
Penicillin-streptomycin (sterile filtered 100x) ⁴	10000 units penicillin 10 mg/ml streptomycin
Cell culture medium ⁵	80 ml fetales bovines serum (FBS) 10 ml antibiotic (penicillin, streptomycin)
Formaldehyde-solution ⁴	36.5 – 38% in H ₂ O
4',6-diamidin-2-phenylindol (DAPI) hydrochloride ⁶	5 mg/ml stock
Alexa Fluor 568 Phalloidin ⁶ 300 units	60 - 100% (w/v)
Carbol-fuchsin	solution 1:2 in PBS

¹ Sur Tec (Bernsheim, Germany)

² Henkel (Düsseldorf, Germany)

³ AppliChem (Darmstadt, Germany)

⁴ Sigma Aldrich Co. LL (Steinheim, Germany)

⁵ Bio Whittaker Lonza (Verviers, Belgium)

⁶ Life Technologies Corporation (Eugene, USA)

⁷ Roche Diagnostics GmbH (Mannheim, Germany)

⁸ Fluka Analytical (Steinheim, Germany)

⁹ ©Merck KGaA (Darmstadt, Germany)

¹⁰ VWR International GmbH (Darmstadt, Germany)

EXPERIMENTAL PROCEDURE

3.2 Analytical methods

3.2.1 Scanning electron microscopy (SEM) and focused-ion-beam (FIB)

The studies on the PEO-surfaces were carried out on a scanning electron microscope using a FEI Helios 600 (DualBeam) field-scanning electron microscope (FESEM) (Thermo Fisher Scientific, Hillsboro, USA). The images were generated at an acceleration voltage of 0.35 - 30kV at a working distance of 1 - 10 mm. The specified resolution of the device was 0.9 nm at 15 kV and optimum working distance or 1 nm at 15 kV at the coincidence point. For imaging, an Everhart-Thornley- or InLense-detector was used for the secondary or back-scattering electrons.

The micrographs of the layer thicknesses were represented by using the focused-ion-beam technique of the DualBeam (FEI Helios 600) of the scanning electron microscope with gallium ions from a liquid metal ion source (LMIS). The resolution of the FIB was 5 nm at 30 kV at the coincidence point and the maximum ion current was 20 nA. An Everhardt-Thornley detector and a CDEM detector (Channel Detection Electron Multiplier) were available for recording the secondary electrons, thus the secondary ions could also be detected. The eucentric height of the FIB was 4 mm. Platinum was used as a deposition materials for the protection of the surfaces. This can be seen on the layer thickness images as the uppermost layer.

3.2.2 X-ray diffraction (XRD)

The x-ray analytical measurements were carried out on a Xpert MPD powder diffractometer (PANalytical, Kassel, Germany) with Ni-filtered Cu-K $\alpha_{1,2}$ -radiation ($\lambda_{K\alpha 1} = 154.05929(5)$ pm, $\lambda_{K\alpha 2} = 154.4414(2)$ pm) in Bragg-Brentano geometry ($\theta/2\theta$). The data were collected from 20° to 100° 2 θ with a step-size of 0.0167° per 3 seconds.

3.2.3 Band gap measurement

The band gaps of the produced PEO-samples were determined from UV-Vis diffuse reflectance spectra. A Shimadzu UV-Vis spectrophotometer UV-2600 (Duisburg, Germany) equipped with an ISR-2600 plus a two-detector integrating sphere recorded the spectra. Barium sulfate was used as a reference and was measured before the series to smooth the background. The data were collected from 200 to 1400 nm in 0.5 nm steps.

EXPERIMENTAL PROCEDURE

3.2.4 X-ray-photoelectron spectroscopy

The XPS measurements were performed with a VG 220i-XL-system in magnetic lens mode. The decrease angle of the photoelectrons was 0° with monochromatic $Al_{K\alpha}$ -stimulation. The surfaces were irradiated and measured in Constant Analyser Energy-Mode (CAE) with 70 eV pass energy for overview spectra and with 20 eV in the energetic high resolution line spectra. The analyzed area had a diameter of 0.65 mm and the neutralization of electric not conductive samples was carried out with low energetic electrons with an energy of 4 eV.

3.2.5 Electron backscatter diffractometry (EBSD)

The EBSD measurements were carried out on a Zeiss Supra 55 VP FEG-scanning electron microscope (Zeiss, Oberkochen, Germany) with variable pressure Mode. The imaging was performed under the pressure of a high vacuum at about $1 \cdot 10^{-6}$ mbar with a SE-detector. A Nordlys detector from Oxford Instruments (Abingdon, UK) was chosen for EBSD measurement with an accelerating voltage for SEM between 10 and 20 kV, and the samples were tilted to a standard angle of 70° . The elemental and crystallographic phase and orientation was made with the analysis system by Oxford Instruments (Abingdon, UK) and the program utilized the AZTec software for the evaluation of the results.

3.2.6 RAMAN Spectroscopy

The micro-Raman spectrometer LabRam ARAMIS (Horiba Jobin Yvon, Bensheim, Germany) was equipped with 532 nm (Nd: YAG), 633 nm (He-Ne) and 785 nm (diode laser) lasers and a He-Ne-Laser of 633 nm was chosen. The samples were focused with a 50x lens from Olympus (Olympus Europa SE & CO. KG, Hamburg, Germany) with a numerical aperture setting of 0.75 with a dot setting of 865 nm. The spectra were acquired in a range of 100 cm^{-1} to 1000 cm^{-1} with a resolution of 3.2 cm^{-1} by a CCD detector. The settings and position of the spectra were calibrated and measured against the Raman signal of a Si wafer at 520.7 cm^{-1} .

3.2.7 Scanning transmission electron microscopy (STEM)

The TEM imaging was carried out using an FEI Tecnai TF20 S-TWIN (Thermo Fisher Scientific, Hillsboro, USA) with a field emission gun operated at 200kV in scanning-mode (STEM). An HAADF-STEM detector (Model FP-5360/20, Fischione Instruments, Export, USA) was used to acquire the images. To map the distribution of the crystallites, the camera length was adjusted to the system, and the dominating diffraction ring was placed onto the

EXPERIMENTAL PROCEDURE

detector ring. This led to a good visibility of the crystallites with varying intensities depending on the crystal structure and orientation. TEM samples were prepared with standard focused-ion-beam procedures in a FEI Helios 600 machine (Thermo Fisher Scientific, Hillsboro, USA), as described in [175].

3.2.8 Physical vapor deposition (PVD)

The application of the titanium layer to a polyetheretherketone base body (PEEK) was carried out by means of an ion-assisted high-frequency (HF) plasma polymerization process in a plasma reactor with a volume of 50 cm × 50 cm × 50 cm. The reactor was evacuated with a turbodraining pump (520 l/s) and the substrate was fixed onto the 30 cm × 20 cm electrode plate. In a preceding step, the polymer substrate had been provided with an adhesion-promoting layer in the same reactor. Hexamethyldisiloxane (HMDSO) and oxygen were used as precursors for the primer layer. The sputter etching process ($O_2 = 80$ sccm, $U_{BIAS} = 800$ V, $t = 60$ s) was carried out at a base pressure of $1 * 10^{-4}$ mbar. The HMDSO could flow into the reactor at a flow rate of 2 sccm with a coating time of 300 seconds, and after switching off, the surface was activated for 30 seconds. The metallization of the precoated PEEK substrate was performed by RF magnetron sputtering. The used target material was metallic titanium (purity: 99.9%) with a distance of 45 cm from the substrate. Argon was fed into the chamber with a flow of 120 sccm at a base pressure of $1 * 10^{-6}$ mbar, and the sputtering power at 2000 W was kept constant. After a processing time of 2 hours, a 4 μm thick titanium layer was obtained on the PEEK substrate.

3.2.9 Fluorescence measurement

The optical representation of the cells was carried out with a Zeiss Axio Imager M1 microscope with the integrated camera AxioCam MRn and recorded in digital form with the software Axio Vision. The cells were optically displayed on the microscope with a mercury vapor lamp (X-Cite 120 series) in a wavelength range of 400 - 600 nm. The representations of the cell nuclei and cell filaments were shown individually and were pictured with an overlapping function with a 2/3 "CCD sensor (6.45 μm x 6.45 μm pixels) with RGB color and respective UV filters. The reflector module FL P & C with a free setup of ≥ 22 mm contains a filter set with the modules 450 - 490 nm, 530 - 885 nm and 750 - 790 nm. The relative spectral sensitivity of the emission dye for the red dye Alexa Fluor 568 was at a wavelength of 603 nm and, for the blue dye DAPI, at 461 nm.

EXPERIMENTAL PROCEDURE

3.3 Working regulations

3.3.1 Plasma electrolytic oxidation

The titanium samples with grade 1 purity were cut into 1.5 cm x 1 cm rectangular plates, see Tab. 10. The TiO₂ layers were produced in different acidic, alkaline, and neutral aqueous electrolytes, as listed in Tab. 11. For the investigations into biocompatibility, electrolyte E5 was chosen with the aim of forming hydroxyapatite on the surfaces. The titanium samples were pretreated with Sur Tec®152 and Turco®7758 (Tab. 8) to remove impurities and the natural oxide layer. An experimental setup for performing the PEO-process with a ramp of 3 min and a subsequent holding time of 15 min was set for all samples. The oxidation process using a two-electrode circuit was carried out in an ice-cooled glass beaker where the temperature was held between 290 K and 303 K. A titanium plate was used as the permanent counter electrode and the titanium sample was the working electrode. The solution was stirred on a digital magnetic stirrer (IKA-Werke GmbH & Co. KG, Staufen, Germany). A commercially available power supply EA PS 8360 15T (0-360 V, 0-15 A, 1500 W, EA Elektro-Automatik GmbH & Co. KG Viersen, Germany) was used and the setup was set using the UTA 12 software (Fraunhofer IFAM). After the PEO-process, the samples were rinsed in demineralized water and air dried at room temperature.

Tab. 10: Chemical composition in atomic percent of pure titanium plates grade1 (cp-Ti)

Element	Fe	O	N	C	H
Atom-%	0.20	0.18	0.03	0.10	0.015

Tab. 11 Chemical contents of the used electrolytes

Electrolyte	Concentration/ components	Discharge voltages/ V
E1	0.3 M H ₃ PO ₄ , 1.5 M H ₂ SO ₄	100 - 280
E2	0.2 M Ca(C ₂ H ₃ O ₂) ₂ , 0.02 M NaC ₃ H ₇ O ₆ P	180 - 320
E3	1.5 M H ₂ SO ₄	80 - 220
E4	1.5 M H ₃ PO ₄	180 - 320
E5	0.5 M NaOH, 0.2 M Na-Tartrate	50 - 140

EXPERIMENTAL PROCEDURE

3.3.2 Photocatalytic measurement

Using a Cary®50 Conc UV/Vis-spectrometer (Varian Inc., Agilent Technologies, Santa Clara, USA), the photocatalytic activity was measured by observing the degradation of methylene blue (MB, 37 mM, AppliChem GmbH, Darmstadt, Germany) and rhodamine B (RB, 0.005 mM, AppliChem GmbH, Darmstadt, Germany) in an aqueous solution. The UV/Vis measurements of methylene blue were performed in the region from 450 nm to 800 nm because of an absorption peak maximum at 664 nm [26,176]. For rhodamine B the region of 400 nm to 700 nm was taken with an absorption peak maximum at 554 nm [177]. The PEO titanium samples were immersed in the dye solution and irradiated under UV light (black light, 25 W, Phillips, Germany). After a selected treatment time, the dye solutions were measured with the UV/Vis-spectrometer. To exclude adsorption or desorption effects, an untreated titanium plate was also measured. Furthermore, an additional PEO-treated sample was left in the dark, while the dye solutions were irradiated without a sample as references.

3.3.3 X-ray diffraction (XRD) and Rietveld refinement

The obtained diffractograms of the PEO-surfaces were examined by Rietveld refinement (DiffracPlus, TOPAS 4.2, Bruker AXS Karlsruhe, Germany). The refinement included the filtering of the phase compositions, the average crystallite sizes and the preferred orientations of the oxide phases on the produces surfaces. The phase compositions could be determined by the reflection intensities as well as the preferred orientations of the crystallites, which were determined by Rietveld refinement for the corresponding direction in the crystal lattice. The average crystallite sizes of the phases could be determined during the refinement.

3.3.4 Spectroscopic investigations on the plasma electrolytic discharges

The additions to the PEO-process model were supported by some of the spectroscopic measurements of the plasma discharges that appeared during the PEO-process. Therefore, an USB4000-spectrometer (Ocean Optics, Inc., USA) with a linear silicon CCD array detector (Toshiba, TCD1304AP, 3648 pixels) and a wavelength response of 200-1100 nm suitable for Vis and shortwave NIR was used. The spectrometer was focused on the titanium surfaces and one spectrum was measured for every one second during the whole PEO-process. At the start of the plasma discharges, the spectra of resulting gaseous phases were detected. The related spectral peaks were analyzed by hand.

EXPERIMENTAL PROCEDURE

3.3.5 Seeding of cell culture

The cell cultures were handled under sterile conditions and all consumables were sterilized before usage. The experiments were executed on an MG-63 osteoblast-like cell line (CLS no: 800125, Eppelheim Germany) and they grew at 37 °C in a humidified atmosphere with 5% CO₂ in 75 cm³ cell culture flasks for 2 days. Prior to the seeding procedure, the sample surfaces were sterilized by washing with 70% isopropanol and a subsequent UV-treatment for at least 30 min and were then washed with medium (Mc Coys 5A with L-glutamine). The cells were seeded at a density of 1 x 10⁵ cells/ mL into each well of the 12-well plates with 1 mL cell suspension. The seeding was conducted on the samples within the wells.

3.3.6 Cell adhesion with vertical flow assay

The strength of the cell adhesion was investigated with a special setup [178]. Using a syringe pump, a PBS solution was injected vertically to the samples through a tube with a previously investigated flow rate. The diameter of the cannula was 0.6 mm and the sample was set at 6 mm under the cannula. This distance remained constant due to the developed setup, using two titanium plates with the dimensions 10 cm x 10 cm and fixed with screws. The PBS (PBS, 1% (v/v) in H₂O) was prewarmed to 37 C and the syringe was filled with approx. 8-9 mL prewarmed PBS and attached to the pump. A flow rate of 1800 mL/h was set, the pump was started, and the water flow stopped after the whole tube was filled with liquid. Afterwards, the sample was taken out of the 12 - well plate and placed in the middle of the metal device and the flow of 5 mL PBS was started. The diameter of the syringe was 15.8 mm and the treatment time was 12-15 s. Afterwards, the samples were incubated for 20 min in 1 mL 2.5% glutaraldehyde. The cells were stained with carbol-fuchsin (1:2 in PBS). Of this staining mixture, 1 mL was added to each sample and incubated for 5 min at room temperature. Then, the cells were washed two times with 1 mL PBS for 5 min. The sample surfaces were dried, and images were taken.

4. RESULTS AND DISCUSSION

Chapter 1: Characterization

4.1 Oxide layer modification by plasma electrolytic oxidation with variation of the electrolytic system

This chapter is based on the investigations published in [93]. The plasma electrolytic oxidation was used to produce porous and crystalline titanium dioxide layers in different electrolytes. The plasma electrolytically oxidized titania layers were investigated with regards to their morphology and corresponding to the electrolytic system. Different morphologies and the influence of the electrolytic system on pore size and layer thickness were examined.

4.1.1 Electrolytic systems

To investigate the influence of the electrolyte composition on the morphology and the plasma electrolytic oxidation process five different electrolytes were used, as shown in Tab. 11. The titanium samples were prepared according to section 3.3.1. In the first step, the influence on the breakdown voltages was investigated, and Fig. 20 shows the measured breakdown voltages.

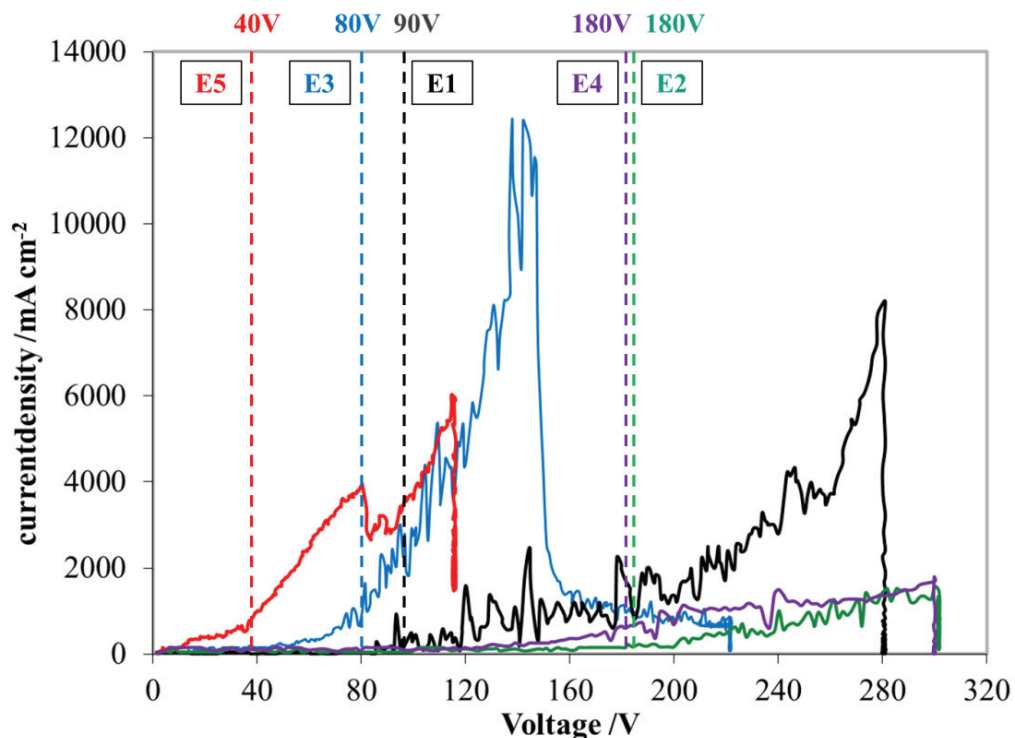


Fig. 20 Current density of the different electrolytic systems with the characteristic breakdown voltage where the PEO-process starts, “Reprinted with permission from Journal Surface and Coatings Technology, 315 (2017) 139–149. Copyright 2017 Surface & Coatings Technology.”

The graph shows the characteristic current flows of the plasma electrolytic oxidation process for each electrolytic system. During the voltage ramp and starting at the breakdown voltage the current density starts to fluctuate, which is related to the start of the micro-discharges. This fluctuation represents the inhomogeneous process and layer growth. The current density grows until the end value is reached and decreases at the holding time. Each composition of the electrolyte catalyzes a different breakdown voltage value. The acidic electrolytes E1 and E3 both have similar and low breakdown voltages between 80 and 90 V. In contrast to these two acidic electrolytes, electrolyte E4 shows the same breakdown voltage as E2 at 180 V. The last electrolyte, E5, has the lowest breakdown voltage of 40 V, this contains an organic compound (tartaric acid). Venkateswarlu et al. [179] described a dependency of the breakdown voltage on its conductivity and Ikonopisov et al. [44] developed an equation for this correlation, which shows the linearity to each other.

$$V_b = a_B + b_B \cdot \log \frac{1}{\kappa}$$

V_b is the breakdown voltage, a_B and b_B are constant values for the electrolyte composition and κ is the electrolyte conductivity. If the conductivity κ of the electrolyte decreases, V_b increases. The conductivities of the electrolytes were measured and are summarized in Tab. 12.

Tab. 12 Conductivities of the used electrolytic systems at room temperature, “Reprinted with permission from Journal Surface and Coatings Technology, 315 (2017) 139–149. Copyright 2017 Surface & Coatings Technology.”

Electrolyte	E1	E2	E3	E4	E5
Conductivity κ / $\text{mS}\cdot\text{cm}^{-1}$	631 ¹	16.81 ²	611 ¹	40.4 ²	101.9 ²

¹CRC Handbook of Chemistry and Physics, W. M. Haynes, 96th Edition, 2015-2016

²WTW Cond 315i/SET, Weilheim, Germany

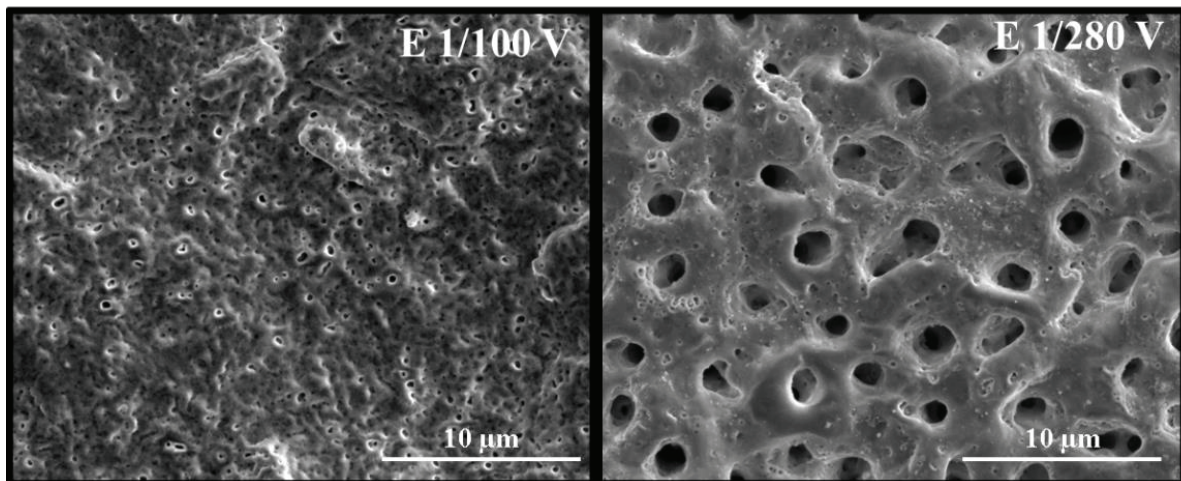
Electrolytes E1 and E3 show the highest conductivity above $600 \text{ mS}\cdot\text{cm}^{-1}$. Both electrolytes contain sulfuric acid, which increases the charge transfer, and a decrease in the breakdown voltage follows. H_2SO_4 can provide a slow metal dissolution rate and a subsequent fast increase in current density over a small voltage range. In contrast, the electrolytes E2 and E4 both contain phosphate-ions. Kern et al. [180] describe an inhibition effect of phosphoric acid on the plasma electrolytic oxidation process. Phosphate-containing electrolytes increase the breakdown voltage because of a less oxidizing behavior, while the ions promote metal passivation on the surface. These inhibit the micro discharges [53,180].

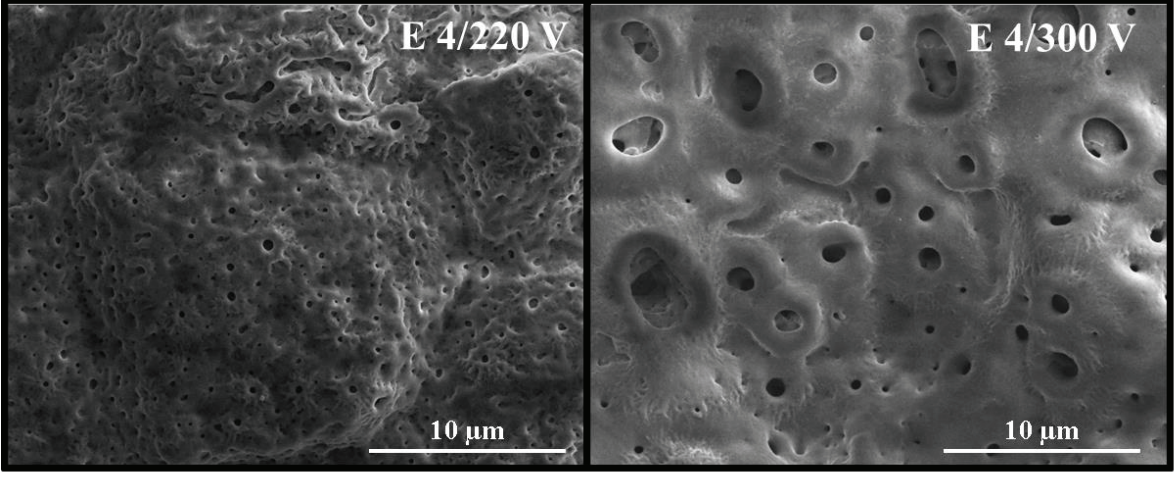
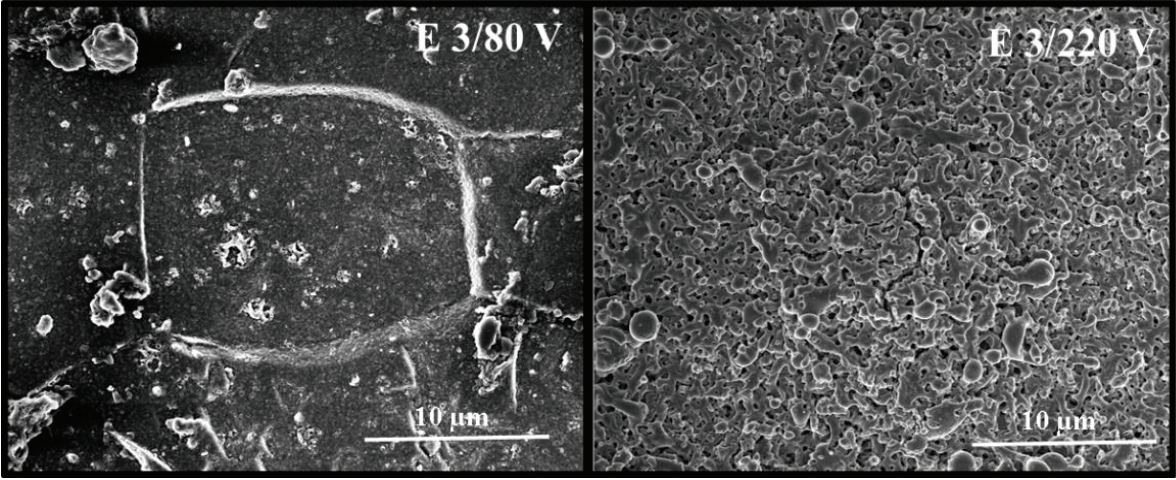
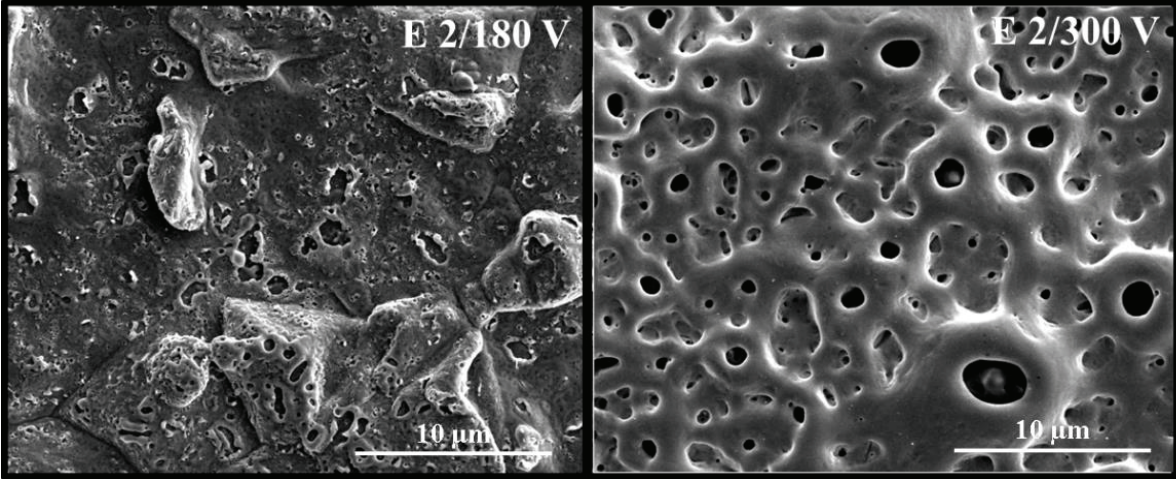
The extremely low conductivity of electrolyte E2 can be explained on the one hand by the phosphate it contains and on the other hand by the lower oxidation ability of alkaline electrolytes because of an increased gas evolution at the anode surface. Therefore, the dissolution of the metal is preferable to the growth of the oxide layer, and this leads to a higher breakdown voltage [181]. According to Venkateswarlu et al. [179], organic compounds can decrease the breakdown voltage like in electrolyte E5 with tartaric acid. This can be seen for electrolyte E5, which has a very low breakdown voltage of 40 V.

4.1.2 Morphology of the PEO oxide layers

4.1.2.1 Surface thickness, surface topography, pore sizes

Because of the differences in the breakdown voltages of the electrolytic systems, the resulting morphologies of the produced samples were investigated. Two different applied voltages were investigated for each electrolyte. One value close to the breakdown voltage and one high voltage were used to observe the differences between pore sizes and layer thickness. The highest voltage refers to the highest possible voltage of the power supply (EA PS 8360 15T (0–360 V, 0–15 A, 1500 W)). The SEM images of the surfaces and some FIB-cuts of the layer thicknesses are shown in Fig. 21 and Fig. 22. On the left side, the lowest applied voltages are illustrated, while the highest applied voltages are given on the right side.





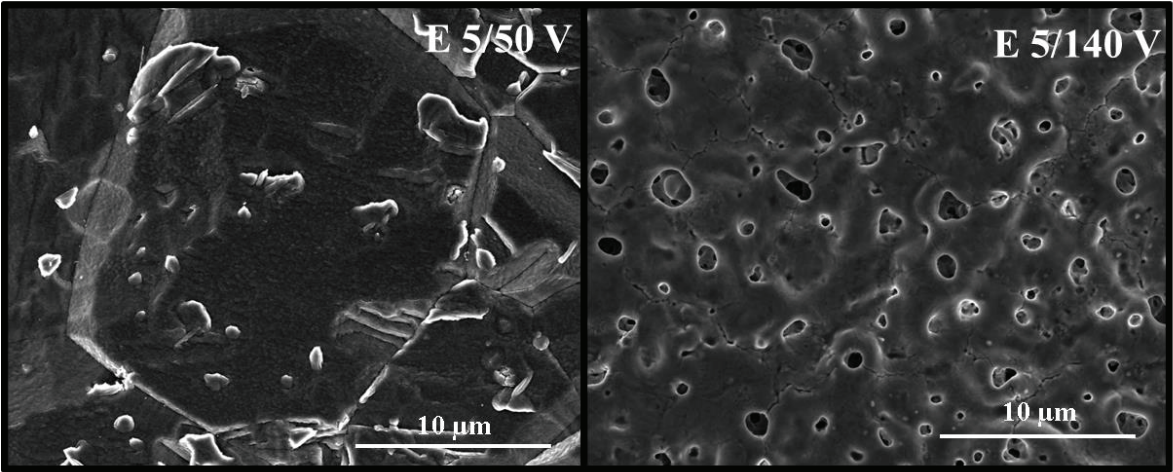
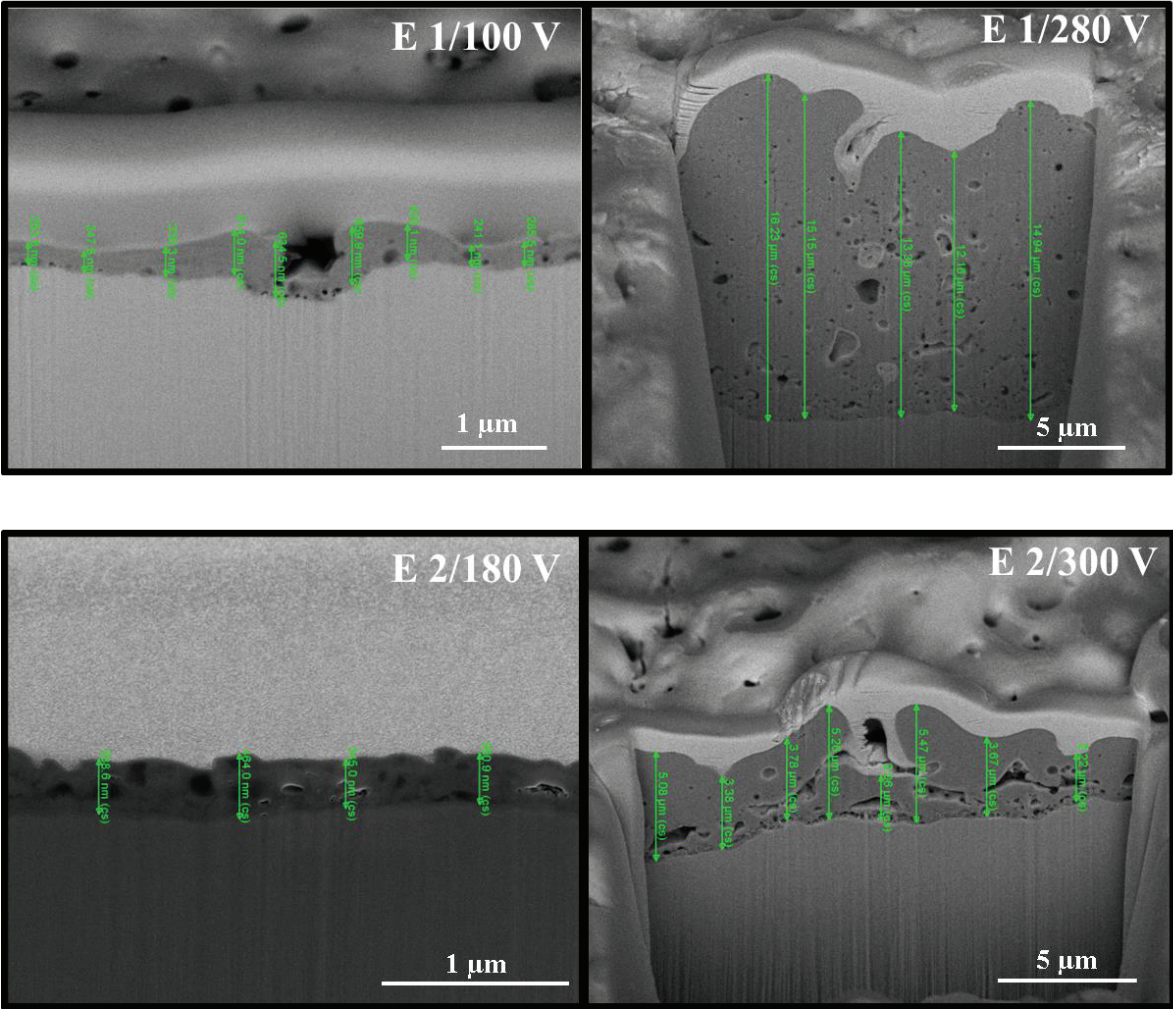


Fig. 21 SEM micrographs showing the surface topographies of the PEO-treated Ti-plates in the different electrolytes (E1 – E5), “Reprinted with permission from Journal Surface and Coatings Technology, 315 (2017) 139–149. Copyright 2017 Surface & Coatings Technology.”



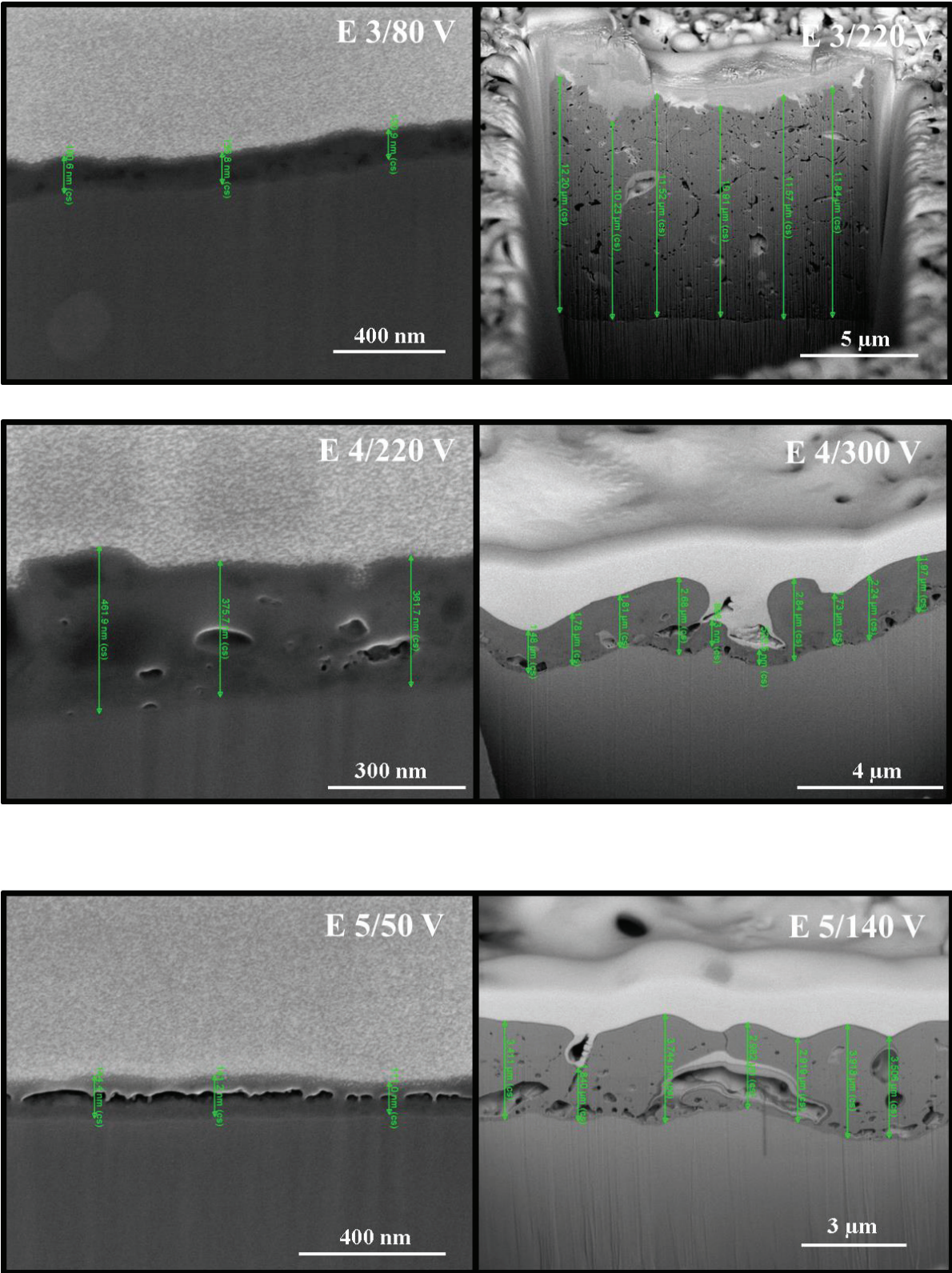


Fig. 22 SEM micrographs showing the oxide layer thickness of the PEO-treated Ti-plates in the different electrolytes (E1 – E5), “Reprinted with permission from Journal Surface and Coatings Technology, 315 (2017) 139–149. Copyright 2017 Surface & Coatings Technology.”

Chapter 1: Characterization

Surface morphologies with the typical porous and rough circular or elliptical pore shape formed on the titanium dioxide surfaces with the help of the PEO-process and the micro discharges. The morphology of the titanium dioxide layer for low applied voltages is not yet distinctive. The PEO-surfaces are covered with a large number of small pores. With higher applied voltages, more larger pores appear on the surfaces. This corresponds with the PEO-process and the different stages of the micro discharges. In the later PEO stages, the discharges become more intense, which leads to the bigger pore sizes [65,76]. Additionally, with higher applied voltages the energy input on the surface is much higher and greater pore sizes follow. With the increase in the voltage, the oxide layer grows continuously, which can be seen in Fig. 23, whereby the layer thicknesses from the lowest applied voltages are on the left side and the highest thicknesses are on the right side. The pore sizes and the layer thicknesses of the as-prepared PEO-samples are summarized in Tab. 13 and Fig. 23. They were analyzed with the image editing Freeware software ImageJ (National Institutes of Health, USA).

Tab. 13 Pore sizes and oxide layer thickness of the PEO-surfaces treated in the different composited electrolytes “Reprinted with permission from Journal Surface and Coatings Technology, 315 (2017) 139–149, Copyright 2017 Surface & Coatings Technology.”

Electrolyte	E1		E2		E3	
Applied voltage/ V	100	280	180	300	80	220
Pore size/ μm	0.43 ± 0.02	2.99 ± 0.5	0.77 ± 0.16	1.91 ± 0.7	-	0.96 ± 0.05
Oxide layer thickness/ μm	0.4 ± 0.17	14.15 ± 1.2	0.37 ± 0.14	3.86 ± 1.32	0.14 ± 0.01	11.38 ± 0.64

Electrolyte	E4		E5	
Applied voltage/ V	220	300	50	140
Pore size/ μm	0.51 ± 0.05	1.12 ± 0.21	-	1.27 ± 0.6
Oxide layer thickness/ μm	0.39 ± 0.06	1.79 ± 0.72	1.32 ± 0.13	3.19 ± 0.65

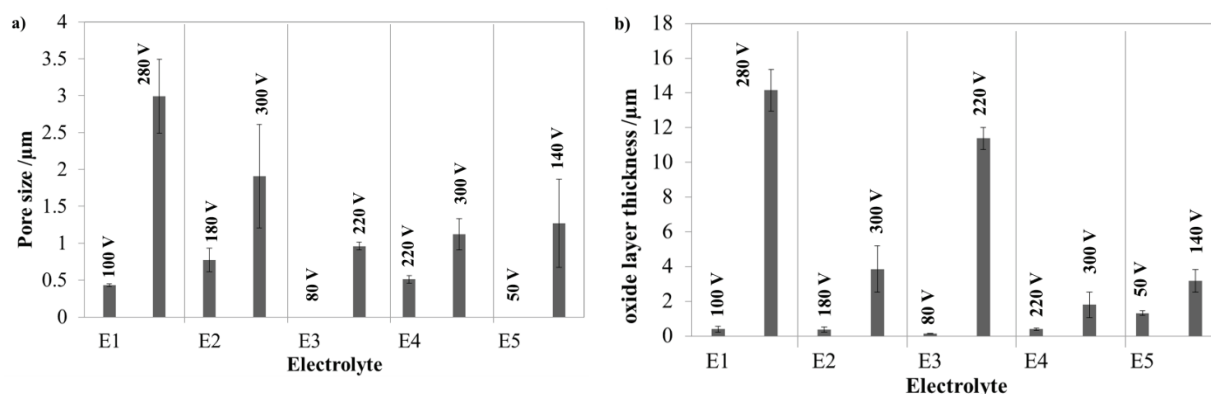


Fig. 23 Pore sizes and oxide layer thickness of the PEO-surfaces treated in the different composited electrolytes “Reprinted with permission from Journal Surface and Coatings Technology, 315 (2017) 139–149. Copyright 2017 Surface & Coatings Technology.”

The start of the micro-discharges on the oxide surface is enhanced by a significantly sharp rise in current density at a characteristic breakdown voltage until the end voltage is reached. After the end value has been reached, the current density decreases to a constant current flow and the oxide layer growth ceases. The growing oxide layer impedes the electron flow through the electrodes, which causes the local breakdowns. Because of a diffusion of H_2O and O_2 towards the bulk metal, the layer growth is kinetically slowed down. Some defects in the titanium surface lead to breakdowns and the characteristic pores [26,30]. This correlation between the applied voltage and the morphology and layer thickness of the PEO-surfaces has been reported in several publications [26,182,183].

With increasing applied voltages, an increase in pore size and number of pores could be determined for all of the electrolytes. The higher applied voltages resulted in a higher current density and also in an increase in the energy of the discharges, which produced more and larger pores and was also mentioned by Frauchiger et al. [165]. This also happens to the layer thickness. Sul et al. [181] described a linear growth with regards to the applied voltage with the following equation (α : growth constant nm/V):

$$d = \alpha \cdot V$$

A lower oxide layer thickness of $3 \mu\text{m}$ can be found for alkaline electrolytes E2 and E5, in contrast to the acid electrolytes, with a thickness of $10 - 15 \mu\text{m}$. The oxide layer growth rate in acidic electrolytes is higher than the dissolution rate. This results in a higher layer thickness. [184]. Alkaline electrolytes have a higher gas evolution at the anode surface due to the hydroxyl ions. This leads to a lower current yield due to the reduction of the surface area and a resulting lower oxide layer growth rate [185,186]. Electrolyte E4 only reached a layer thickness of $1.79 \mu\text{m} \pm 0.72 \mu\text{m}$. Phosphoric acid causes a lower current density which can

result in a lower layer thickness. For each electrolyte, a change in the appearance of the surface could be observed. In general, all surfaces have a characteristic rough and porous structure. The surface morphologies produced in electrolytes E1, E2, and E4 are quite similar to each other, with the expected typical “crater-like” structure. The pores are quite big and isolated from each other with compact titanium dioxide in between. All three electrolytes contain phosphate-ions (PO_4^{3-}) and the pores have a round shape, which is in contrast to the findings by Venkateswarlu et al. [179], who created a round, isolated pore shape for PEO-surfaces produced in borate ($\text{B}_4\text{O}_7^{2-}$) and silicate (SiO_3^{2-})-containing electrolytes. These anions are twofold negatively charged like phosphate ions, and the resulting morphology can be explained with the molecular charge of the components. The charged anions can influence the type of micro-discharge and thus the shape of the pores. For the electrolytes E3 and E5 the pores show a flower-like structure with a connection inside the pore network. The pores of electrolyte E5 have nearly the same shape but are slightly smaller and not as pronounced as in the other electrolytes. Electrolyte E5 contains the organic compound tartaric acid ($\text{C}_4\text{H}_4\text{O}_6^{2-}$). Venkateswarlu et al. [179] also used an electrolyte with an organic compound, namely citric acid ($\text{C}_6\text{H}_5\text{O}_7^{3-}$). Those surfaces look similar to those produced in electrolyte E5. Organic molecules can have a significant influence on the volcano structure and build a more plane and flatter surface. Unlike these structures, electrolyte E3 produces a non-typical PEO-surface. These pores can be described as having a stacked oxide layer with cavities between the layers. These cavities can behave like pores comparable to the results of Oh et al. [6], who described the same pore shape for a 1.5 M H_2SO_4 electrolyte with a stack-like structure of the pore layers.

With plasma electrolytic oxidation it is possible to produce individual morphologies of porous and simultaneously compact titania layers. The process allows pore size and oxide layer thickness to be adjusted for any desired application. The breakdown voltages for alkaline electrolytes can be found at a lower level, in contrast to acidic electrolytes, due to a lower conductivity and a higher gas evolution and the resulting reduction in the anode area. These two effects have an influence on the layer thickness. The phosphate (PO_4^{3-})-containing electrolytes, in comparison to the alkaline electrolytes (OH^-), form the characteristically round PEO-pores, whereby the pores in alkaline electrolytes become more linear. Sulfuric acid (H_2SO_4) produces a stacked cavity-containing pore structure. By altering the composition and nature of the electrolytic system, the morphology, layer thickness, and appearance of the pores can be changed.

Chapter 2: Crystallinity

4.2 Crystallinity of PEO oxide layers

This chapter is based on the investigations published in [93]. Due to a high energy input from the resulting plasma discharges the produced titania layers were investigated regarding their crystallinity. The electrolyte should influence the crystallinity of TiO_2 and the amounts of the related phases of anatase and rutile. These properties of the layers were varied with regard to a possible photocatalytic activity of the crystalline phases.

4.2.1 Degree of crystallinity and phase composition of PEO-layers

Su et al. [187] reported a correlation between the surface crystallinity of PEO-layers and the oxidative behavior of the electrolyte. The crystalline parts can be improved through more aggressive contents. The crystallinity of the as-prepared PEO-layers was examined using x-ray diffraction. The resulting pattern can be seen in Fig. 24 and were refined with Rietveld refinement (Diffrac Plus TOPAS, Bruker AXS GmbH, Karlsruhe, Germany).

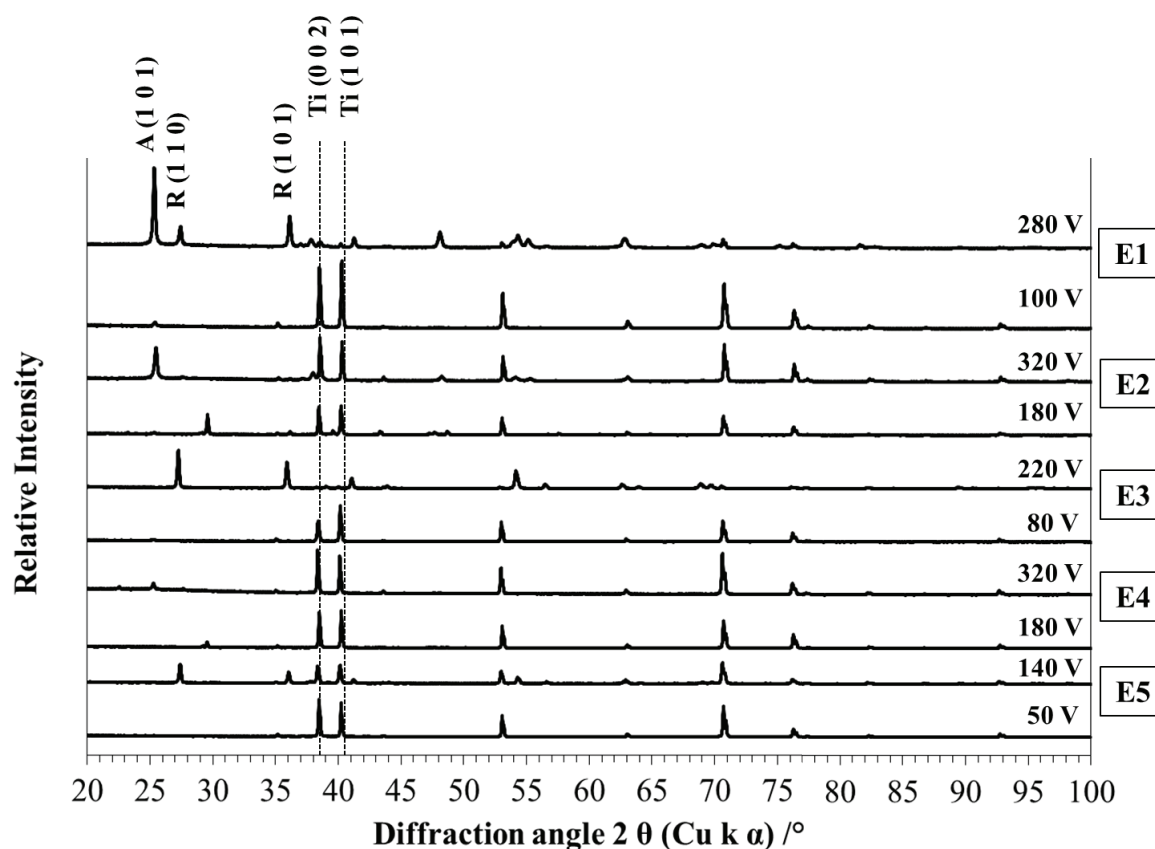


Fig. 24 XRD-pattern of PEO-layers produced in the different electrolytes with the highest and the lowest applied voltage (important reflection peaks are marked; A: Anatase, R: Rutile and Ti: Titanium), “Reprinted with permission from Journal Surface and Coatings Technology, 315 (2017) 139–149. Copyright 2017 Surface & Coatings Technology.”

Chapter 2: Crystallinity

The applied voltages as well as the electrolyte composition have a strong influence on the crystallinity of the PEO-surfaces. With a higher applied voltage, the reflection intensities of titanium decrease whereas the reflections of the crystalline TiO_2 phases appear. An increase in crystallinity due to the dominant anatase reflection at $25^\circ 2\theta$ (1 0 1) of the samples E1 280 V and E2 320 V can be seen. Also, the appearing rutile reflection at $27^\circ 2\theta$ (1 1 0) for samples E1, E3, and E5 increase with higher applied voltages. For all samples, a lower crystallinity at lower applied voltages could be detected. A linear increase in crystallinity with the applied voltage was reported in [25,28,187,188]. In general, an increase in crystallinity is a result of the high energy input [28,49,50,187–190] and the local rise in temperature [47,80] of the intensified discharges during the PEO-process. On the surface of sample E1 280 V, both crystalline phases anatase and rutile can be seen. From the measured x-ray data the phase composition of both crystalline phases was refined with the commercial available software TOPAS. The percentages of the phases are shown in Fig. 25.

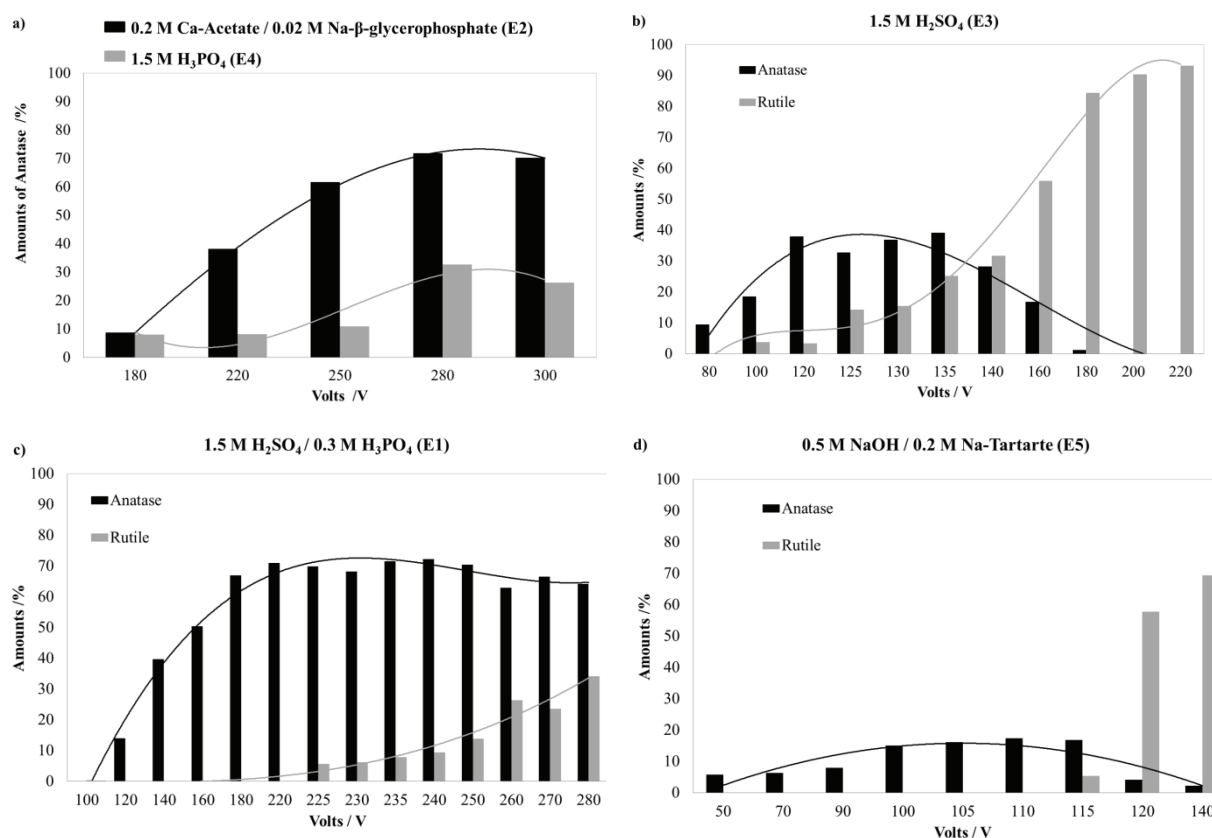


Fig. 25 Amounts in % of anatase and rutile on the treated PEO-surfaces for different voltages (remaining share up to 100% is titanium substrate), “Reprinted with permission from Journal Surface and Coatings Technology, 315 (2017) 139–149. Copyright 2017 Surface & Coatings Technology.”

Chapter 2: Crystallinity

The low oxidizing nature of the electrolytes E2 and E4 produces an anatase-covered oxide surface without rutile contents. In contrast to electrolyte E5 with a similar low conductivity, E5 produces a mainly anatase-covered surface at low voltages. Rutile is formed at 115 V in a very high amount. The pure sulfuric acid electrolyte E3 forms a large amount of rutile with low applied voltages, whereas a mixture of sulfuric acid and phosphoric acid produces mainly anatase amounts. With a higher applied voltage, some rutile amounts appear on the surfaces of electrolyte E1 and the oxide layer thickness increases (Fig. 23, Fig. 25). The increase in layer thickness is caused by an intensity regression of the main reflection peaks because the titanium substrate will be covered with TiO_2 , while the x-ray beam is mainly absorbed by the TiO_2 and primarily oxide is detected. The decreasing titanium amount in the XRD-pattern with higher voltages indicates a growing layer thickness comparable with the SEM micrographs. The increase in crystallinity and layer thickness of the PEO-surfaces may affect the lattice parameters of the include anatase and rutile phases. The refined lattice parameters are plotted in Fig. 26.

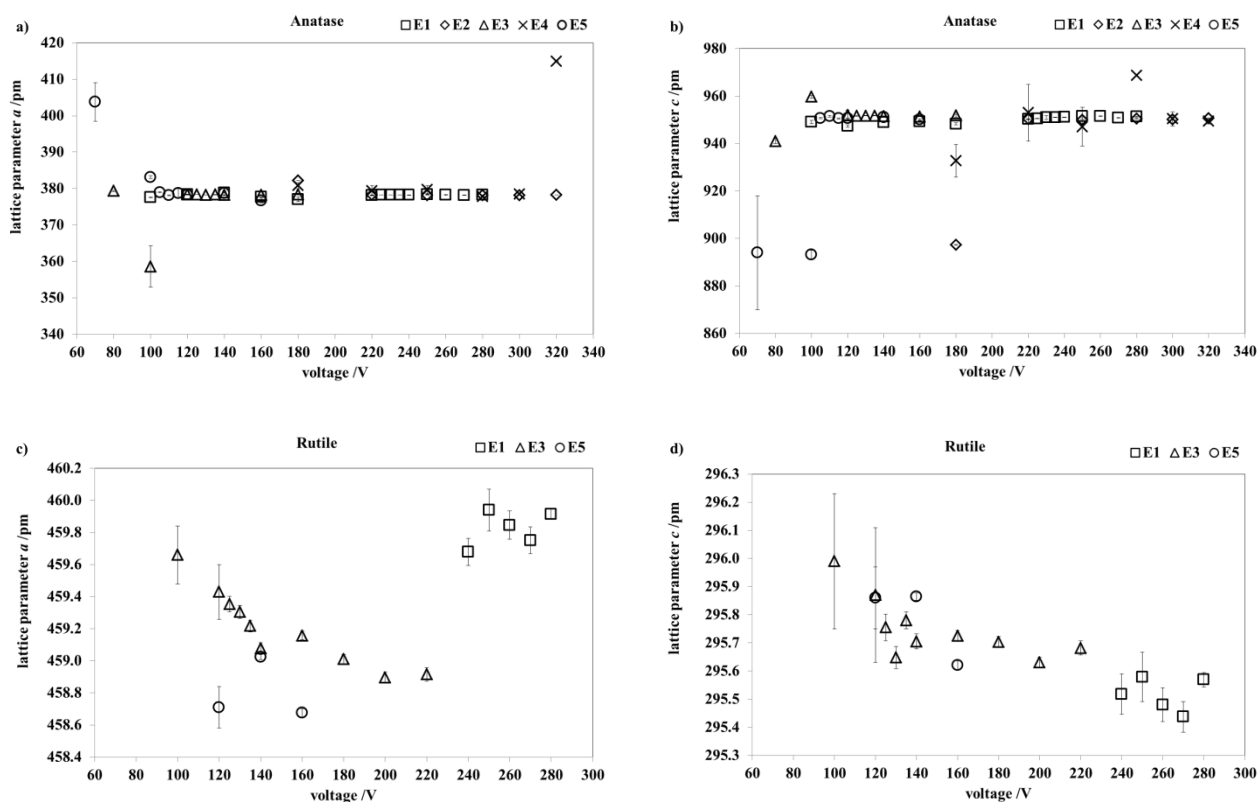


Fig. 26 Lattice parameter of anatase and rutile on the PEO-surfaces of the different electrolytes, “Reprinted with permission from Journal Surface and Coatings Technology, 315 (2017) 139–149. Copyright 2017 Surface & Coatings Technology.”

Chapter 2: Crystallinity

No significant change in the lattice parameters a and c of the anatase phase for all electrolytic systems was observed. However, an exponential change in the lattice parameters a and c for rutile was clear for all electrolytes. The increase in value for lattice parameter a is very clear for electrolyte E1, whereas lattice parameter c decreases. The changes appear in the upper voltage range. For anatase, a lattice expansion at small crystallite sizes has been reported [191–194]. Kuznetsov et al. [195] discovered a lattice expansion for the rutile phase with a decrease in crystallite size. This leads to an anisotropic size-dependent variation of the unit-cell. The crystallite sizes of electrolyte E1 are very small, between 20 and 30 nm, in contrast to the other electrolytes with a crystallite size of 35 to 70 nm (Tab. 14). These small crystallite sizes of all oxide layers suggest that the rutile phase is subject to lattice expansion.

Tab. 14 Average crystallite sizes ($L_{Vol}(IB)$) of rutile for the used electrolytes, “Reprinted with permission from Journal Surface and Coatings Technology, 315 (2017) 139–149. Copyright 2017 Surface & Coatings Technology.”

Electrolyte	Applied voltage /V	Middle crystallite size /nm
E1	230 - 280	21 - 38
E2	180 - 320	No rutile
E3	80 - 220	35 - 62
E4	180 - 320	No rutile
E5	50 – 160	45 - 70

In addition, from the results of the PEO-process a preferred orientation of the crystallites for both polymorphs and the titanium bulk material could be determined. The preferred orientations of the crystals increase the intensity of the main reflection in each direction. Titanium has a preferred orientation in $[0\ 0\ 2]$, $[0\ 1\ 2]$ and $[0\ 1\ 3]$ direction, anatase has a preferred orientation in $[0\ 1\ 1]$ and $[0\ 0\ 4]$ direction and rutile in $[0\ 1\ 1]$, $[1\ 1\ 0]$ and $[1\ 1\ 1]$ direction. Because of the complex behavior of the preferred orientations, spherical harmonics were used for the Rietveld refinement and the XRD-pattern, whereby the marked orientations can be seen in Fig. 27. The preferred orientation of titanium results from the rolling process of the pure titanium plate. The preferred orientation in $[0\ 0\ 4]$ direction of the anatase crystals is the result of a frequent crystal surface in $[0\ 0\ 1]$ direction, which is accompanied by the general extinction of the space group $I4_1/amd$. This preferred orientation of anatase is related to the orientation of titanium in $[0\ 0\ 2]$ direction. Comparatively, $[0\ 1\ 1]$ direction of anatase as well as of rutile also relates to the $[0\ 1\ 2]$ and $[0\ 1\ 3]$ directions of titanium. As a result, the growth of the TiO_2 crystals is dependent on that of the titanium bulk material. Rutile has a second orientation in $[1\ 1\ 0]$ direction which is one of the frequent crystal surfaces.

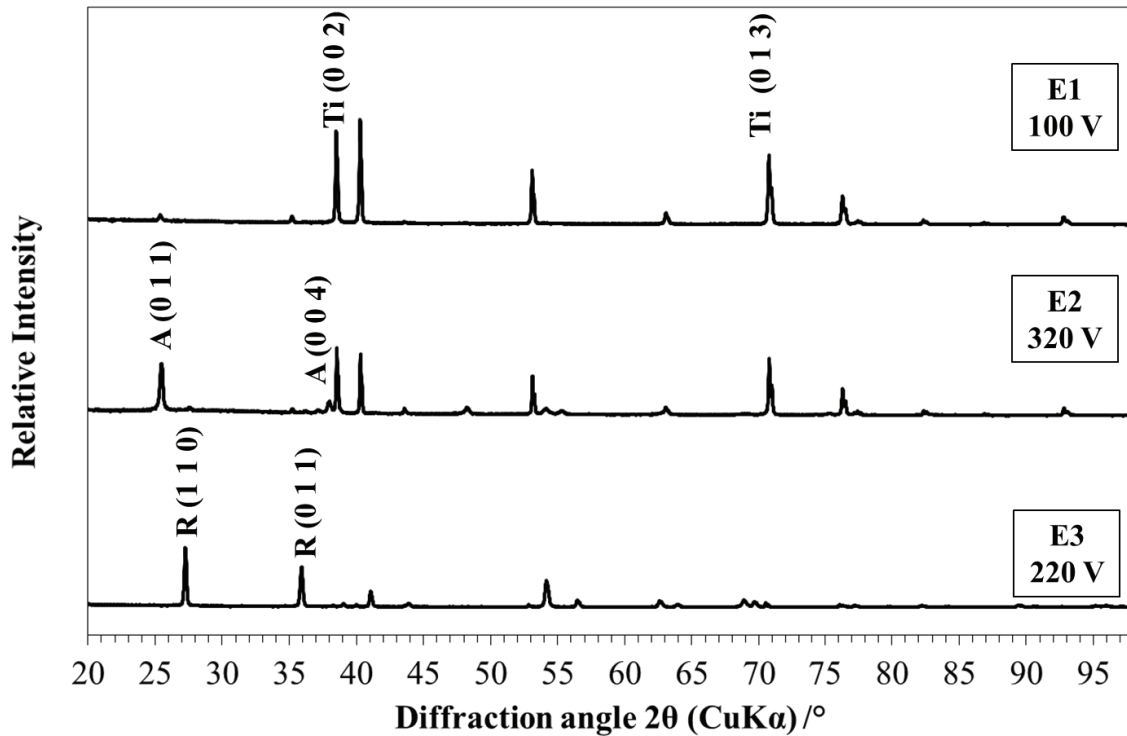


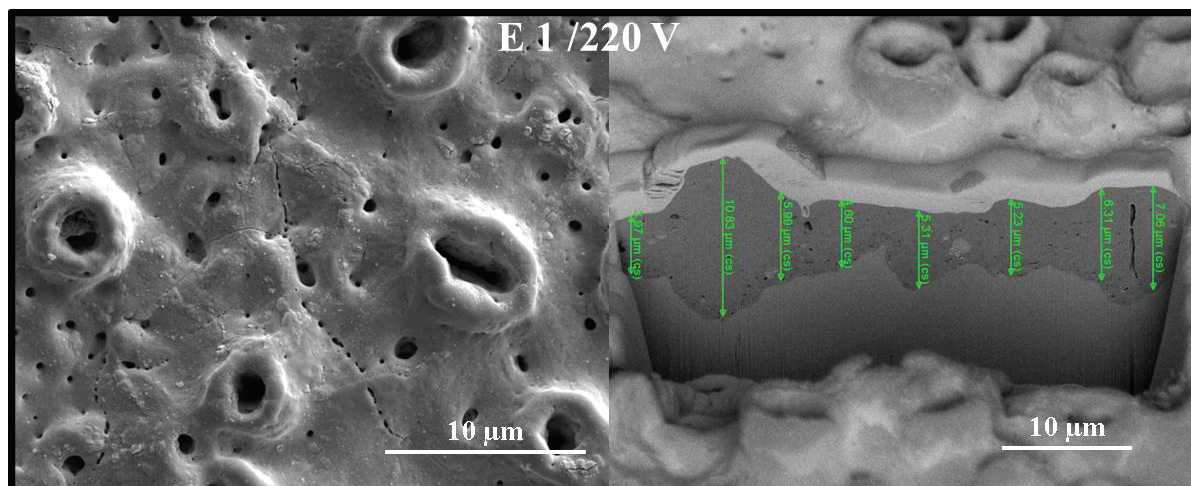
Fig. 27 Preferred orientations of titanium, anatase and rutile on the anodized TiO₂ PEO-surfaces, “Reprinted with permission from Journal Surface and Coatings Technology, 315 (2017) 139–149. Copyright 2017 Surface & Coatings Technology.”

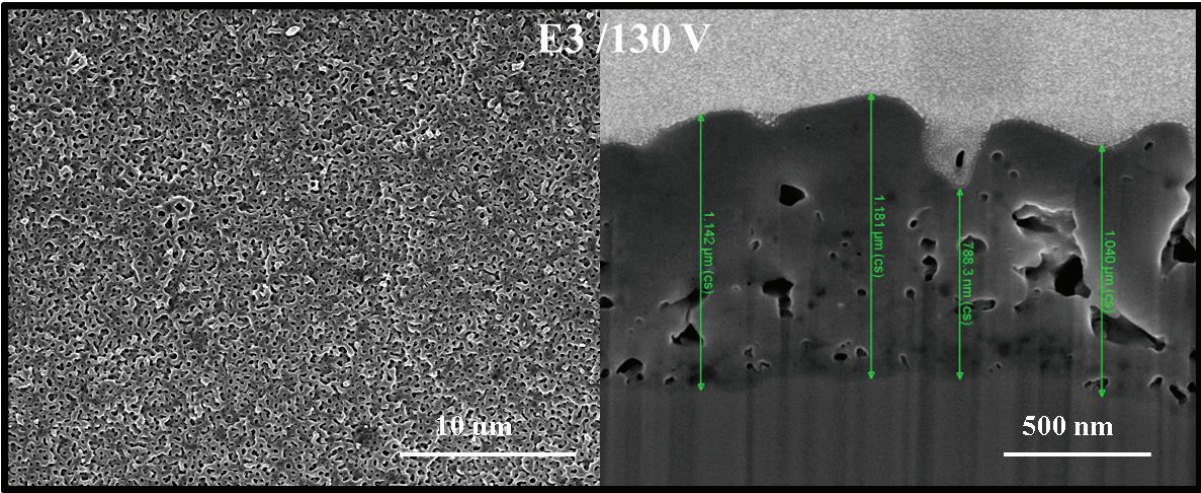
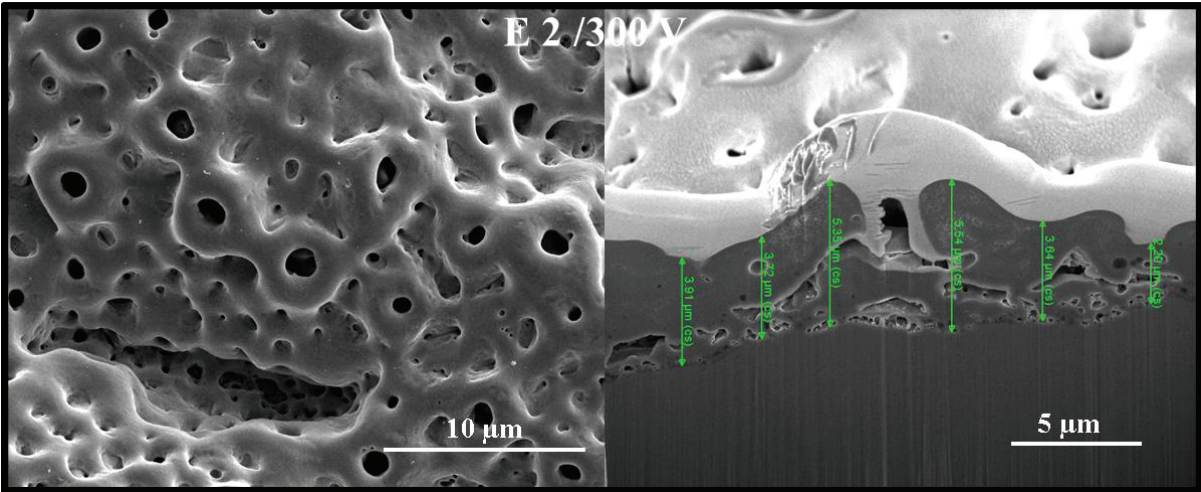
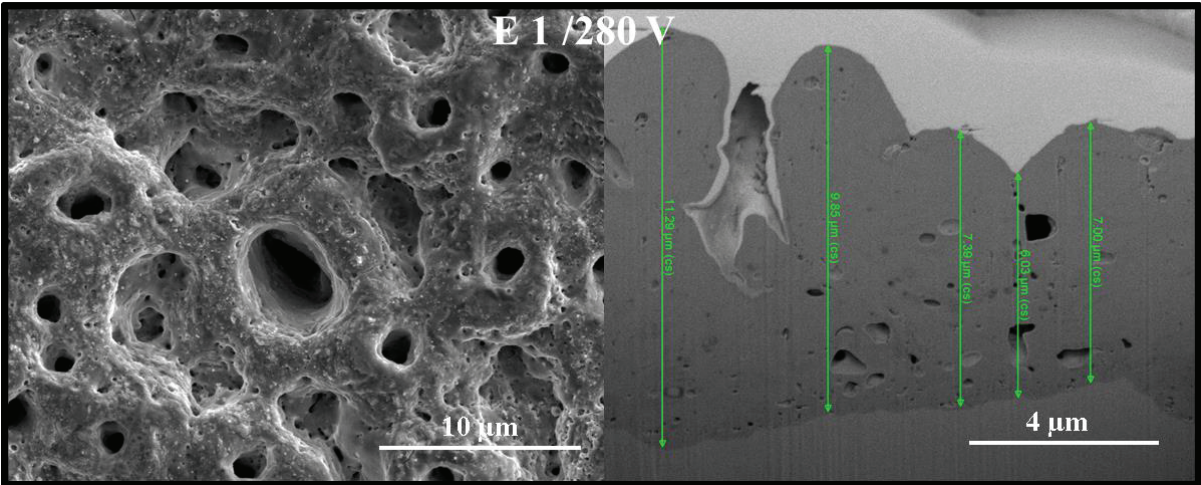
The variation of the applied voltage and electrolytic system influences the crystallinity of the PEO oxide layers with a high amount of anatase and rutile phases. The crystallinity can be controlled and increased with high applied voltages. A high amount of rutile can be produced in the oxide layer with the right electrolyte composition and a high conductivity. These rutile phases can improve a number of properties of the oxide layer, such as aging stability and especially the photocatalytic activity of TiO₂. Furthermore, the ratio of anatase to rutile can be optimized similarly to the photocatalytic active AEROXIDE© TiO₂ P25. Thus, a preferred orientation in crystallites for all phases titanium, anatase, and rutile was discovered in [0 k l] and [0 0 l] preferred directions of growth. Based on all these results, it is possible to tune the crystalline TiO₂ surface using plasma electrolytic oxidation within one synthesis step, and the high crystallinity rate on all measured surfaces can be an indication for a photocatalytic activity of the compact PEO-surfaces.

Chapter 3: Photocatalytic activity

4.3 Photocatalytic activity of PEO-layers

Chapter three is based on the investigations published in [196]. After the investigations into the crystallinity and phase compositions of the as-prepared PEO-layers in the various chosen electrolytes, the possibility of photocatalytic active reactions was investigated. For the examination, surfaces which had a good crystallinity and a promising phase composition of anatase and rutile inside the surface and which were almost identical to the commercially available AEROXIDE® P25 were chosen. For this reason, electrolyte E4 was not considered in the investigations because of the very low crystallinity and anatase content (Fig. 24 and Fig. 25). The titanium samples were prepared in a manner equal to that of all other PEO-samples, according to section 3.3.1, and the compositions of the electrolytes are shown in Tab. 11. The associated SEM-micrographs of the surfaces and the layer thicknesses of the chosen samples are given in Fig. 28. The SEM micrographs show the expected characteristic rough and pore-rich topography, as discussed in section 4.1.2, while the summarized pore sizes and layer thicknesses can be seen in Tab. 13.





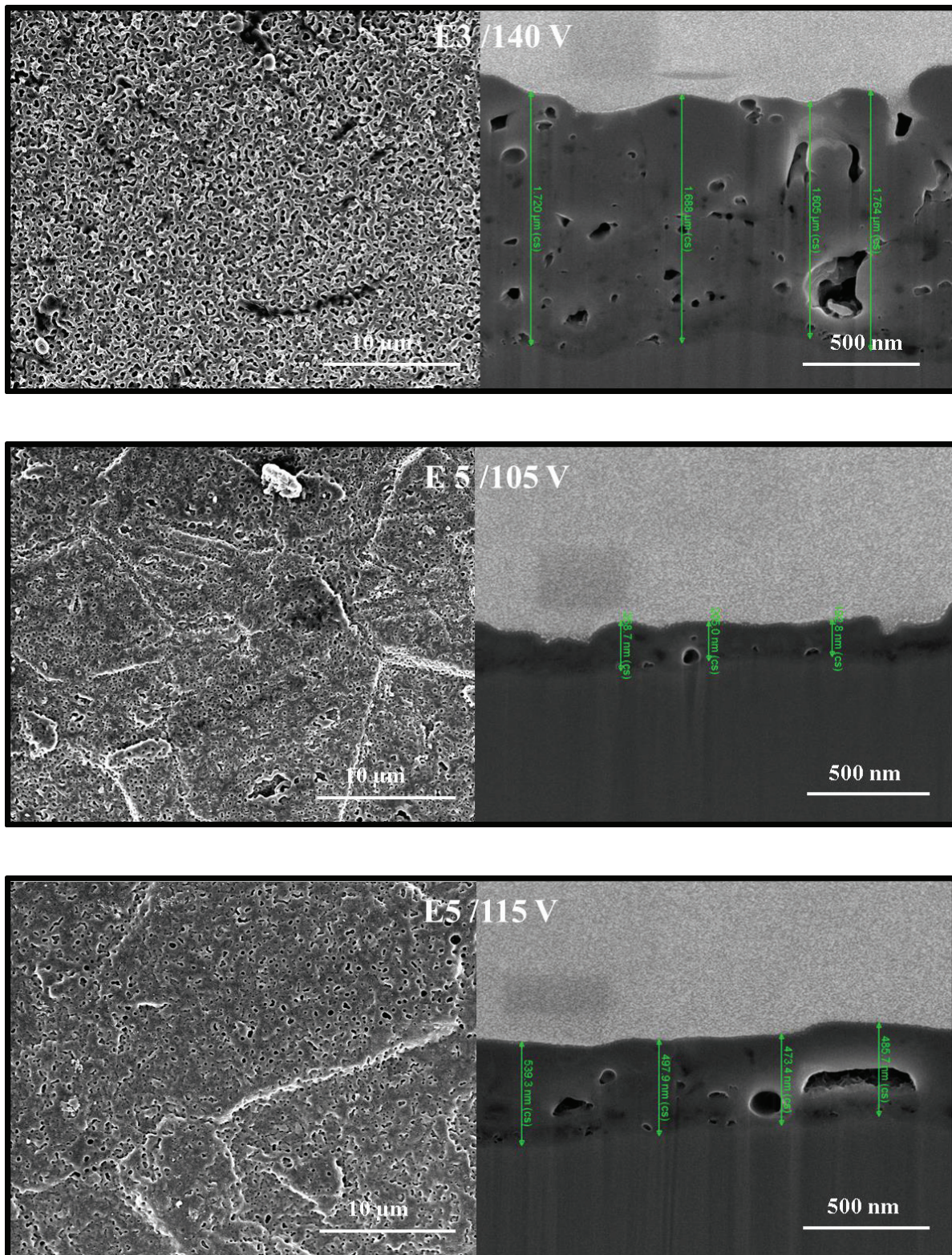
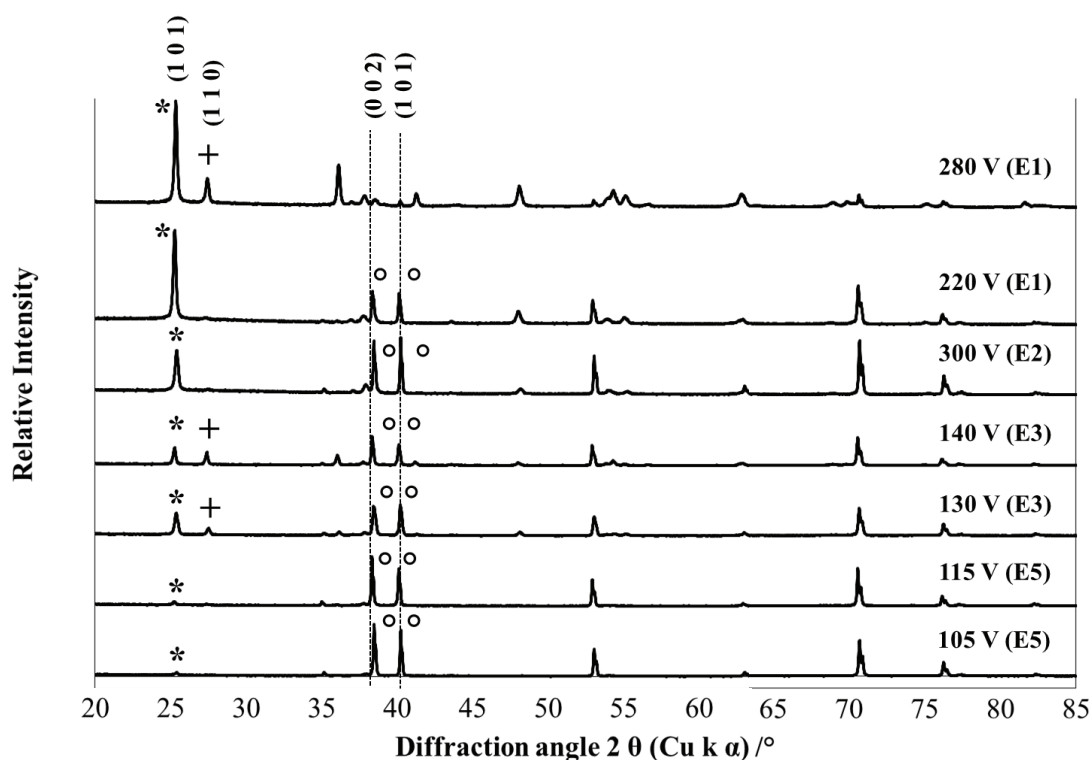


Fig. 28 SEM micrographs of the surface topographies of the PEO-treated titanium plates in the different electrolytes (E1 – E5): (left side) top view on the surface morphology with the characteristically pore-structures (magnification 10 μm) (right side) FIB cross-section of the as produced PEO-layers (different magnifications), “Reprinted with permission from Journal Surface and Coatings Technology, 344 (2018) 710–721. Copyright 2018 Surface & Coatings Technology.”

Tab. 15 Surface morphology and amounts in % of anatase and rutile of the PEO-treated surfaces (the remaining share up to 100% is titanium substrate) fabricated in different electrolytic systems

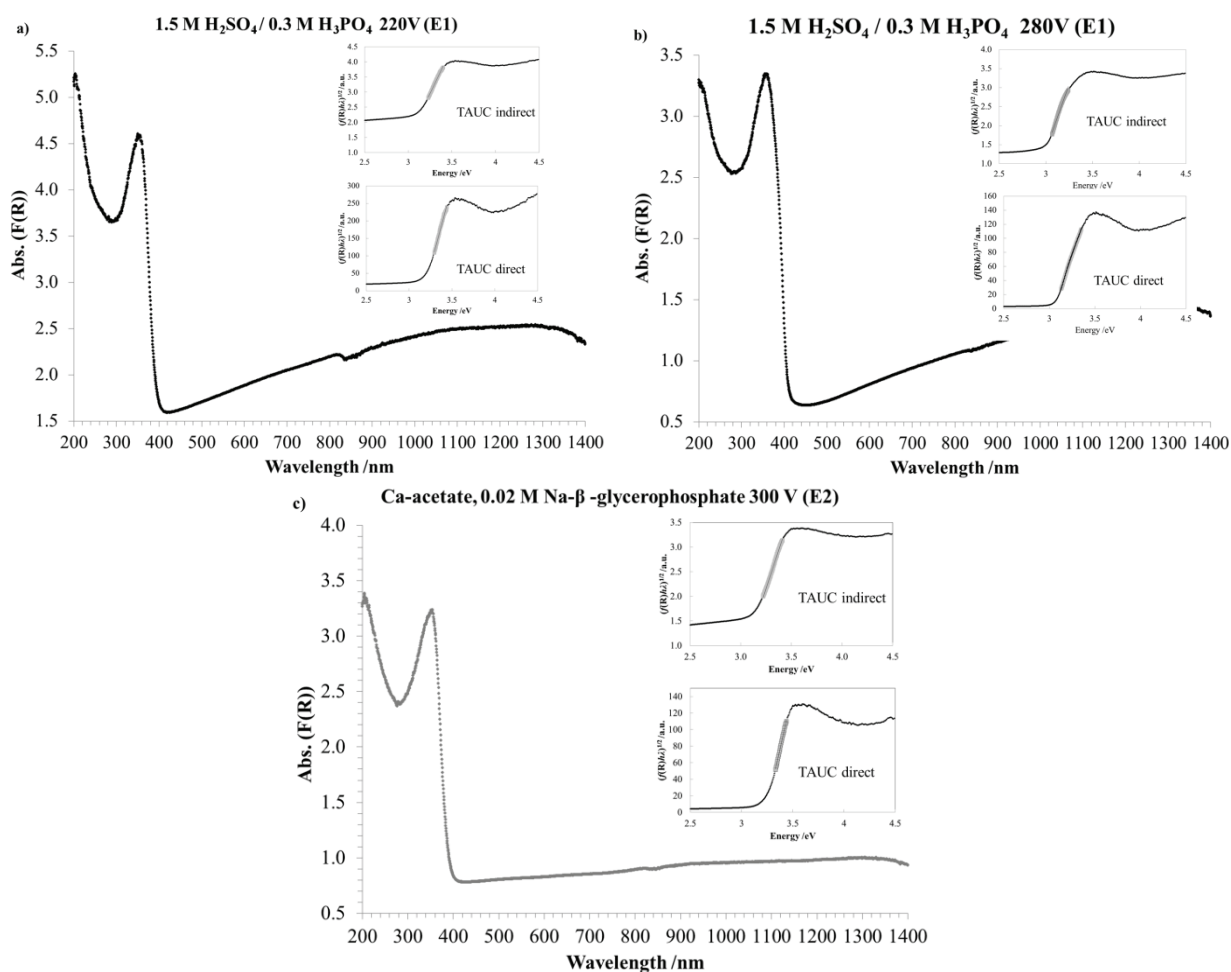
Electrolyte	Applied voltage /V	Pore size / μm	Layer thickness / μm	Phase amount
				anatase : rutile /%
E1	220	1.58 ± 0.31	6.29 ± 1.87	71(3)
	280	2.99 ± 0.51	14.37 ± 1.43	64(12) : 34(7)
E2	300	1.9 ± 0.7	3.86 ± 1.32	70(11)
E3	130	0.27 ± 0.09	1.04 ± 0.15	37(4) : 15(2)
	140	0.37 ± 0.11	1.69 ± 0.06	28(8) : 32(3)
E5	105	0.16 ± 0.02	0.22 ± 0.03	16.1(6)
	115	0.29 ± 0.09	0.5 ± 0.03	16.8(7) : 5(2)

The phase compositions of the chosen surfaces were measured, like the above described surfaces before from the XRD data with Rietveld refinement (Tab. 15). These samples were chosen because of an anatase-rich surface and a ratio of anatase to rutile ranging from 1:1 to 2:1. In the diffraction pattern in Fig. 29, crystalline parts could be easily identified by the main reflections of anatase $25.3^\circ 2\theta$ and rutile $27.4^\circ 2\theta$ for electrolytes E1 and E3. The highest rutile reflection can be seen for sample E1 280 V with a phase composition of 2:1 of anatase to rutile. This could indicate a high photocatalytic activity.

**Fig. 29** XRD patterns of PEO-layers produced in the different electrolytes with the highest and the lowest applied voltage (important reflection peaks are marked; * anatase, + rutile and ° titanium)

4.3.1 Band gap measurements of PEO-surfaces

The XRD results show a crystallinity of anatase and rutile phases on the surface of all produced PEO-samples (Fig. 29). Therefore, some band gap measurements were performed using UV-Vis diffuse reflectance spectroscopy. The expected band gaps of the included TiO₂ polymorphs were investigated for all the chosen samples, these are shown in Fig. 30. To interpret the reflectance spectra, two systems, the so-called TAUC-method [197] and DASF-method [198], were used. In the first step, the reflectance spectra were transformed into an absorbance spectra with the use of the Kubelka-Munk equation [199,200]. Out of these absorbance spectra, the band gaps were then calculated with the TAUC and DASF equations to determine the width and the band gap type (indirect or direct) of the titania layers seen in Fig. 30 and Fig. 31 [201,202].



Chapter 3: Photocatalytic activity

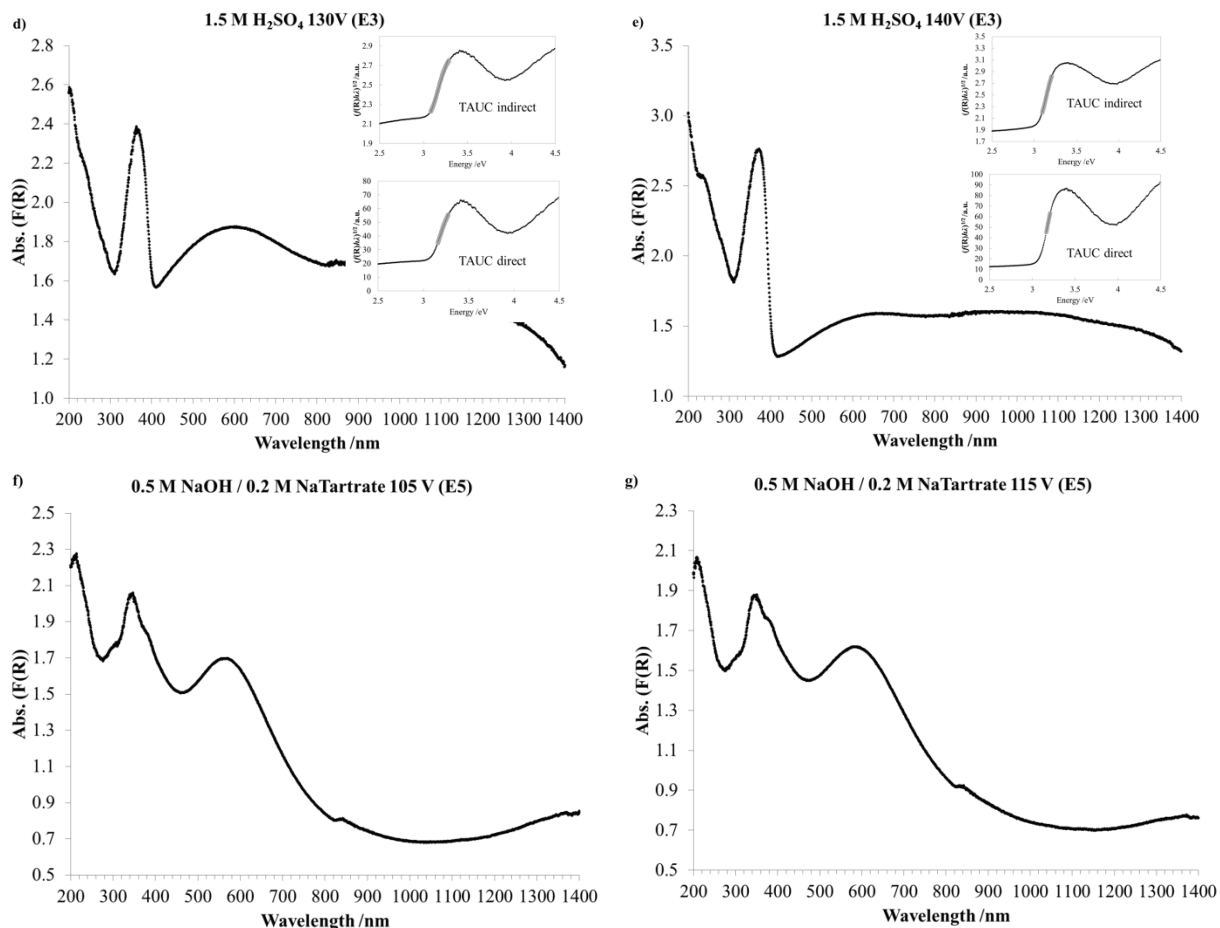


Fig. 30 UV/Vis absorbance spectra of the band gap measurement: Reflectance spectra, evaluated using the TAUC-method. Plots of all measured PEO-layers: a) and b) samples of electrolyte E1, c) sample of electrolyte E2, d) and e) samples of electrolyte E3, f) and g) samples of electrolyte E5

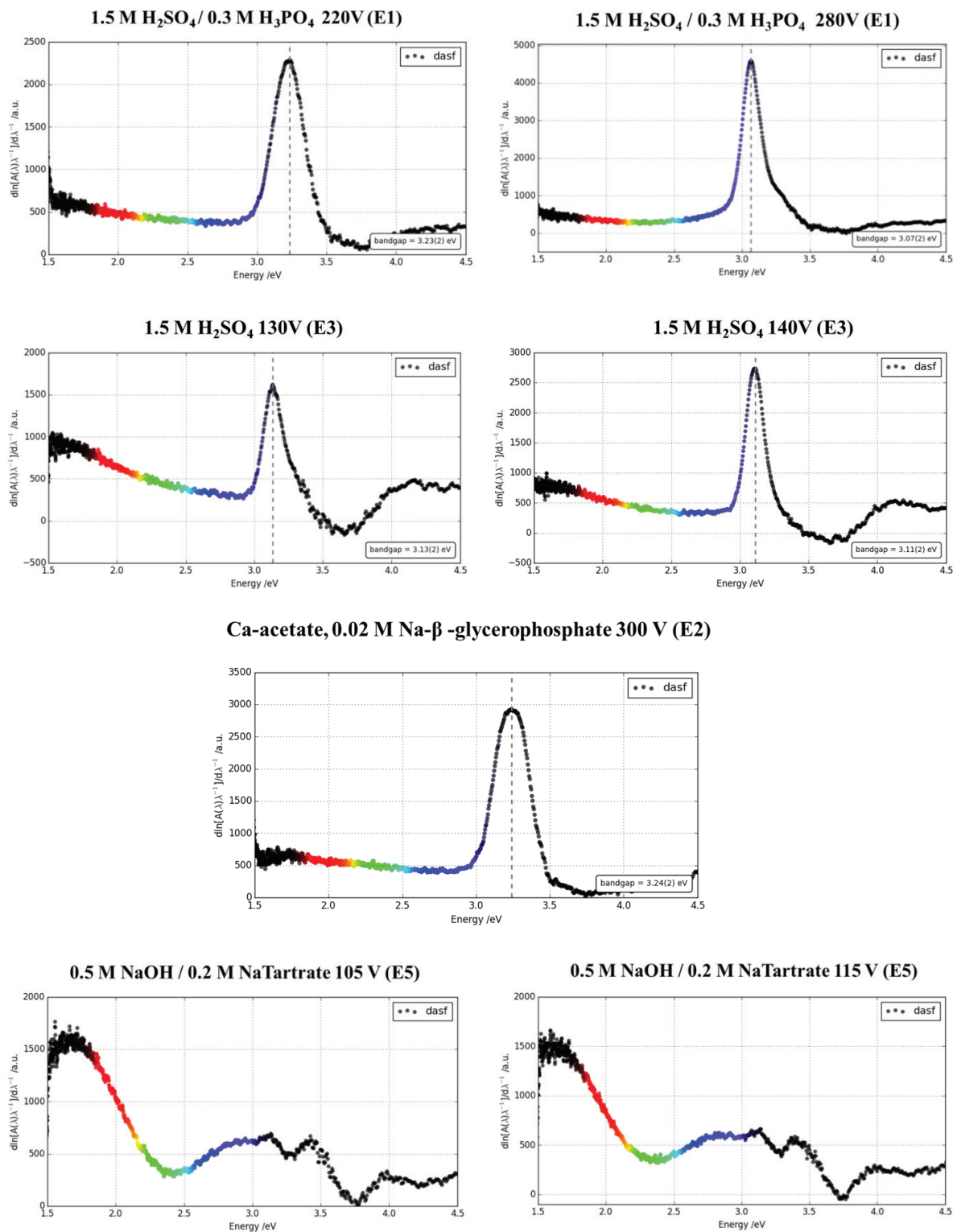


Fig. 31 DASF calculated band gap spectra of the PEO-layers for all electrolytes and the investigates applied voltages; the band gap was analyzed with the peak positions

The TAUC-plots of the samples prepared in electrolytes E1, E2, and E4 show clearly defined expected band gaps. In addition, the calculated DASF-plots have a band gap value for these three electrolytes, that are consistent with the calculation by Souri et al. [198]. Both plots are illustrated in Fig. 30. The samples prepared in electrolyte E5 cannot be refined due to a slight coloration of the surfaces. The rutile phase has a high influence on the band gap values. With a higher rutile content on the surface, the band gap shifts to the rutile value of $E_g = 3.0$ eV. The calculated band gaps of all samples are shown in Tab. 16, whereby the indirect and direct gaps of both methods are summarized.

Tab. 16 Defined band gaps with the TAUC and DASF method for the PEO-treated surfaces for all electrolytes and applied voltages, “Reprinted with permission from Journal Surface and Coatings Technology, 344 (2018) 710–721. Copyright 2018 Surface & Coatings Technology.”

Electrolyte	E1		E2		E3		E5	
Voltage /V	220	280	300	130	140	105	115	
TAUC indirect /eV	2.76(1)	2.80(10)	2.90(1)	2.27(3)	2.71(1)	n.d.	n.d.	
TAUC direct /eV	3.17(1)	3.05(10)	3.24(1)	2.96(3)	3.05(1)	n.d.	n.d.	
DASF /eV	3.23(2)	3.07(2)	3.24(2)	3.13(2)	3.11(2)	n.d.	n.d.	

n.d.: not definable

The PEO titania layers show a clear direct band gap, which is in contrast to the reported indirect band gap of TiO₂. The calculated indirect band gaps of the TAUC plots do not fit to the data from the literature, while the direct band gaps are closer to these reported values [15]. Madhusudan Reddy et al. [203] reported a direct band gap of anatase nanoparticles with a particle size of 5-10 nm, which results in an even smaller crystallite size. The crystallite sizes of the measured samples were refined to a size of 20-30 nm, these are summarized in Tab. 17.

Tab. 17 Average crystallite sizes ($L_{vol}(IB)$) of rutile and anatase on the PEO-samples, “Reprinted with permission from Journal Surface and Coatings Technology, 344 (2018) 710–721. Copyright 2018 Surface & Coatings Technology.”

Electrolyte		E1		E2		E3		E5	
Applied voltage /V		220	280	300	130	140	105	115	
Average crystallite size /nm	Anatase	30.9(3)	28.3(6)	29.4(6)	33.5(6)	34.1(5)	27.9(10)	25.4(9)	
	Rutile	-	38.1(10)	-	34.5(10)	40.4(10)	-	45.2(40)	

A small crystallite size results in an increased specific surface area and the band gap can shift to a direct transition. Semiconductors with a direct band gap can have a greater efficiency in energy absorption because they contain an allowable transition from the conduction band to the valance band. These materials can be much more purposeful for specific applications [203].

4.3.2 Methylene blue/rhodamine B degradation

For the investigation into the photocatalytic activity of the PEO-samples, two aqueous dye solutions were chosen. The widely used dyes methylene blue (MB) and rhodamine B (RB) were measured under UV irradiation by absorption spectroscopy and the degradation reactions of both dyes are shown in Tab. 18. The results from the photocatalytic experiments and the decrease in intensity are seen in Fig. 32 to Fig. 35. Two different dyes were chosen to compare the different degradations of absorption intensity and to exclude adsorption and desorption effects at the PEO-surfaces in the two different systems. As a reference material, one which shows a good photocatalytic behavior, the commercially available photocatalyst AEROXIDE® TiO₂ P25 was used. The P25 is available as a nanoscale powder oxide, while the PEO-surfaces represent oxide films. Despite the differences in texture, the P25 was used as a reference because it consists of pure parts of anatase and rutile and its photocatalytic activity is of the highest top standard. Furthermore, it is used in a wide range of studies researches because of its above-mentioned commercial availability and its wide-ranging investigated photocatalytic activity.

Tab. 18: Degradation reactions of methylene blue (MB) and rhodamine B (RB)

Dye	Degradation reaction	$\lambda_{\text{max}}/\text{nm}$
Methylene blue (MB)		664
Rhodamine B (RB)		554

Chapter 3: Photocatalytic activity

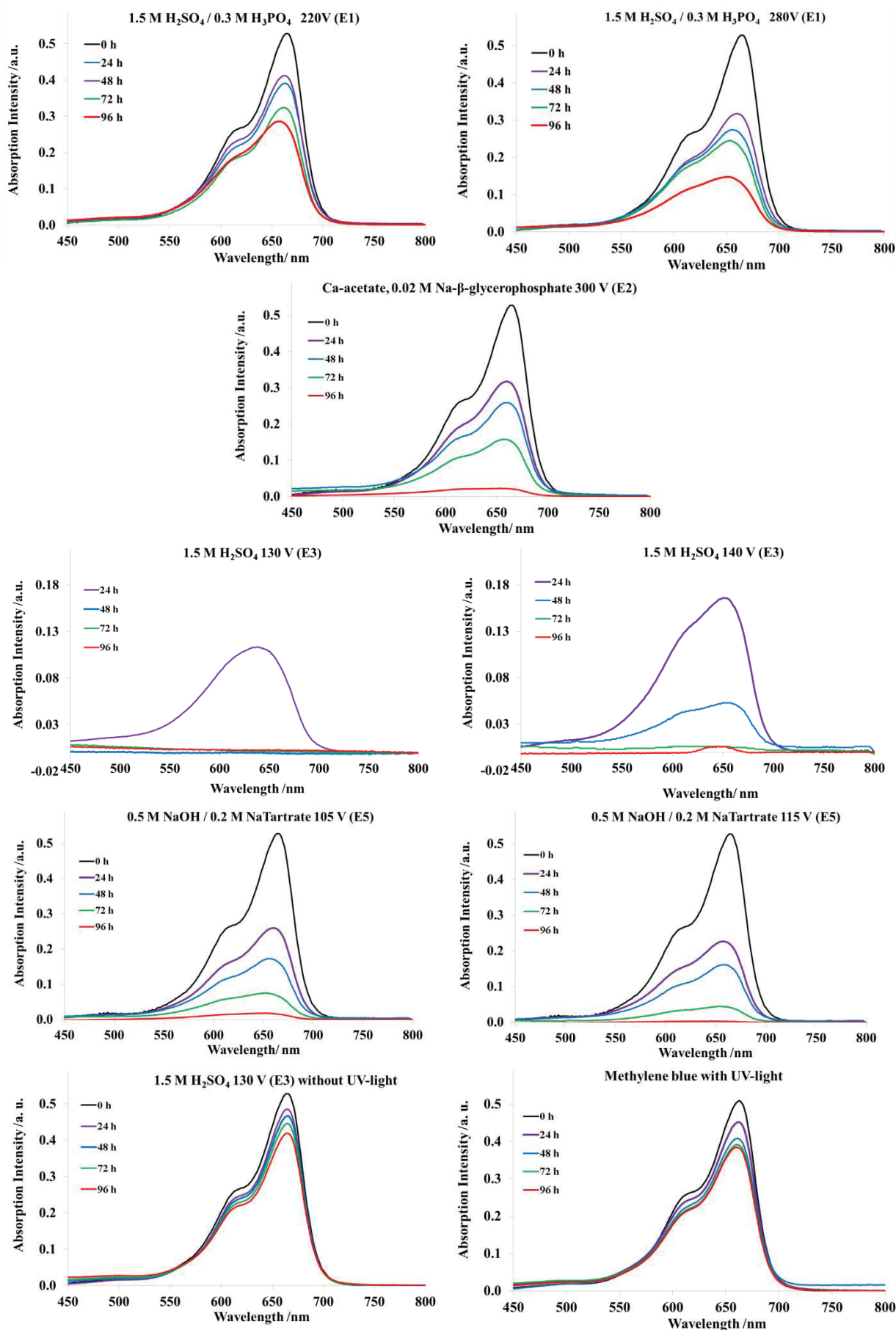


Fig. 32 Degradation curves for methylene blue for the maximum illumination time of 4 days for all electrolytes and applied voltages

Chapter 3: Photocatalytic activity

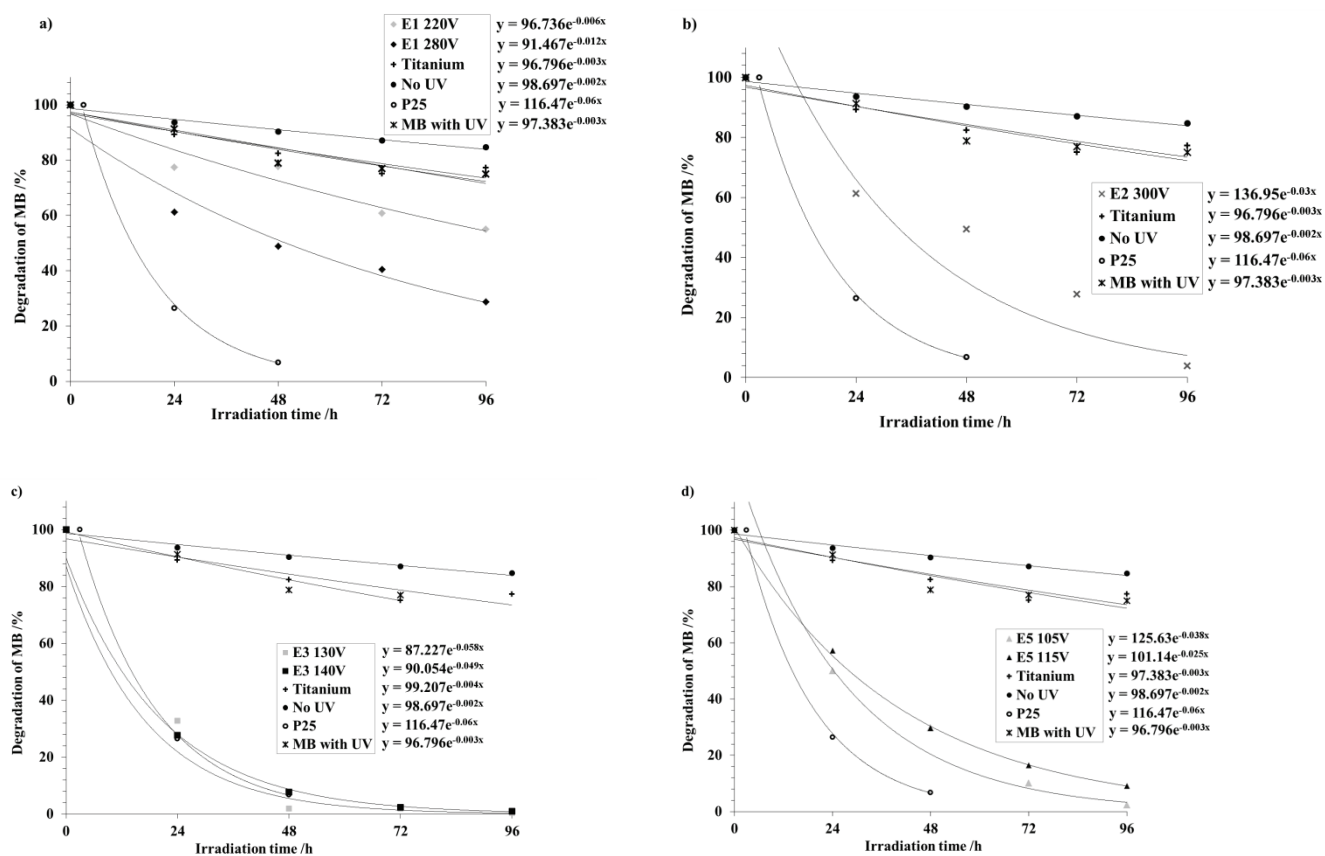


Fig. 33 Degradation rate of the absorption intensity of MB: Values of the measured absorption maximum at 664 nm for the used electrolytes and the applied voltages a) E1 b) E2 c) E3 and d) E5

Chapter 3: Photocatalytic activity

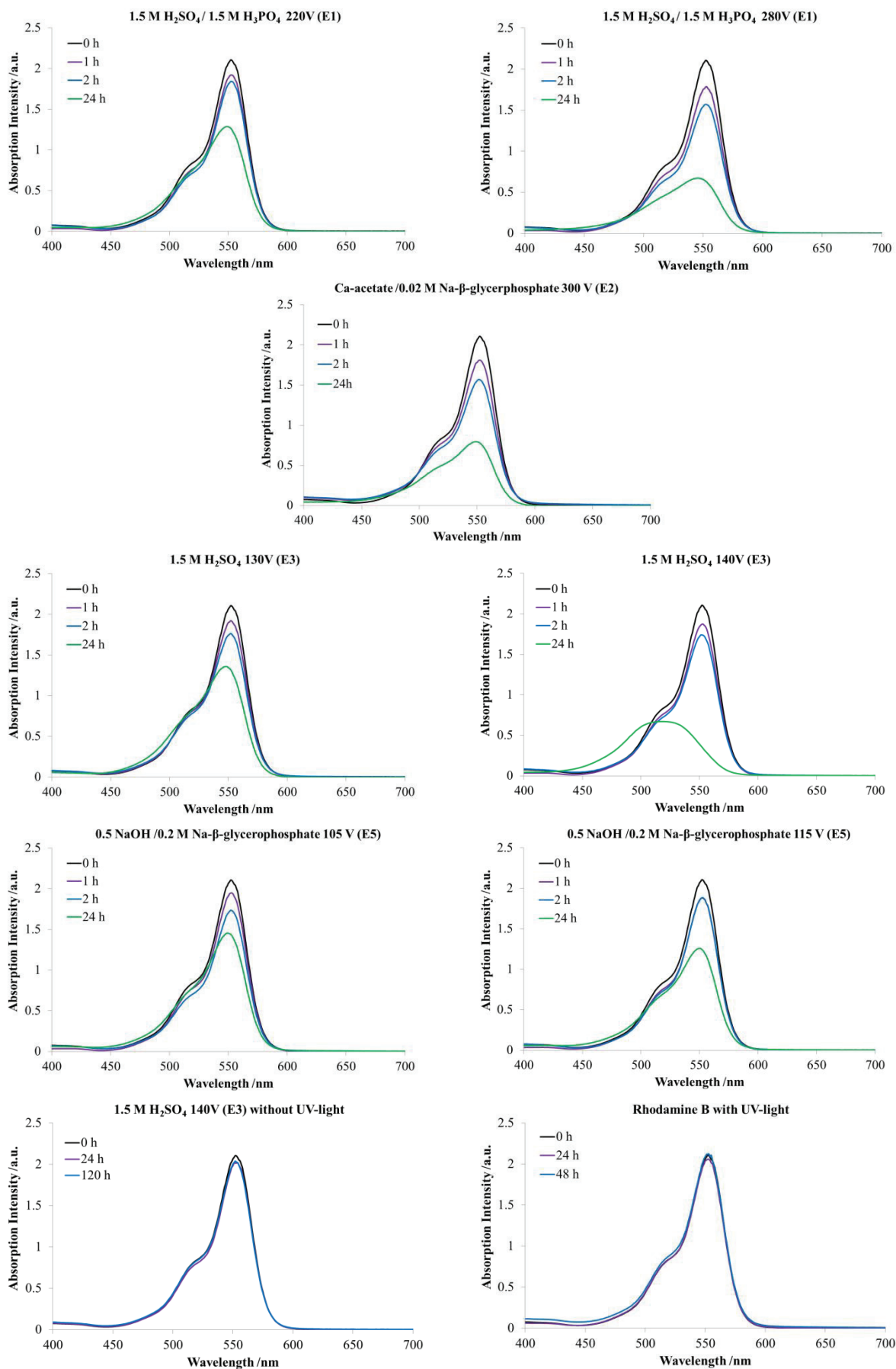


Fig. 34 Degradation curves of rhodamine B for the maximum illumination time of 24 hours and 5 days for the references for all electrolytes and applied voltages

Chapter 3: Photocatalytic activity

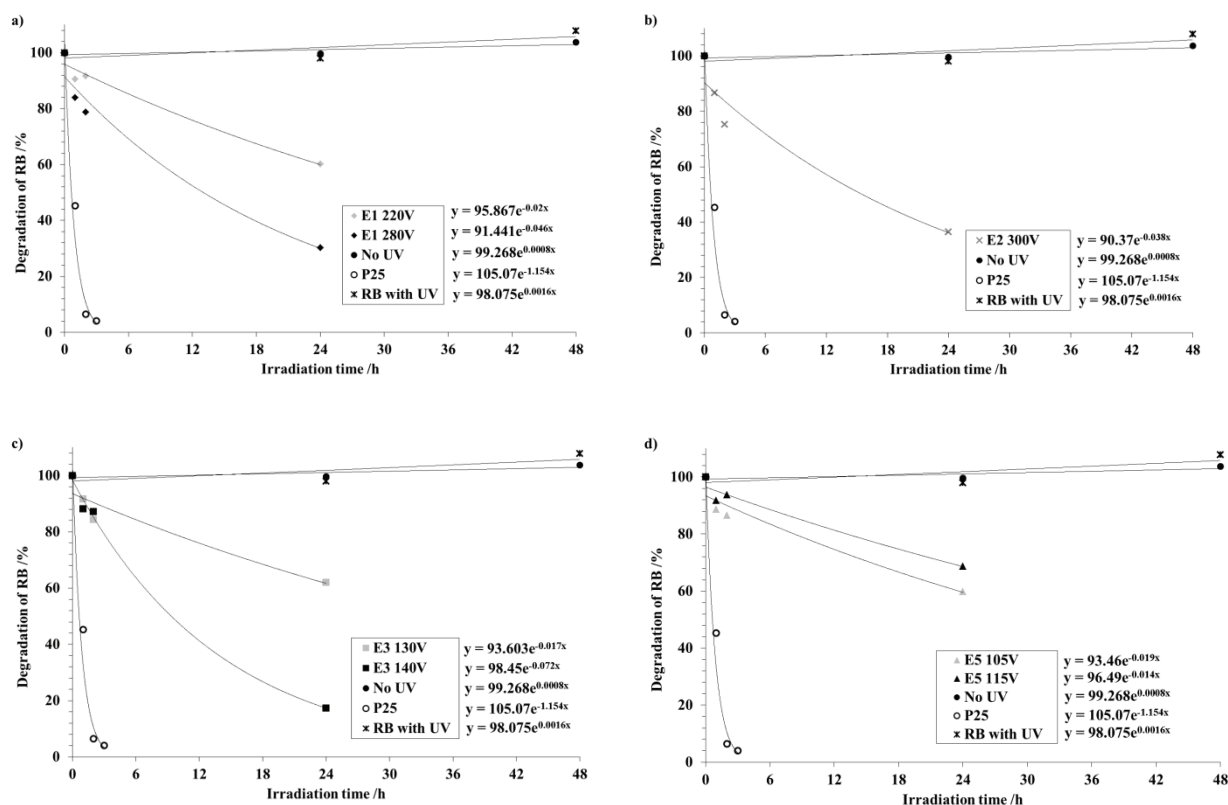


Fig. 35 Degradation rate of the absorption intensity of RB: Values of the measured absorption maximum at 554 nm for the used electrolytes and the applied voltages a) E1 b) E2 c) E3 and d) E5

The used reference AEROXIDE[®] P25 shows the highest degradation rate, as expected, with a disappearance of the absorption intensity already after already 3 hours. This fast reaction under UV-light depends on the interaction of the rutile and anatase quantities and the optimal crystallite size of almost 35 nm. There is an ongoing discussion regarding the photocatalytic measurements of adsorption as well as the splitting effects at the soaked surfaces of the used dyes. PEO-samples have a highly porous surface, as seen in the shown SEM micrographs shown here. To exclude adsorption and splitting effects at the surfaces two reference samples were examined. One PEO-treated sample without UV irradiation and a pure dye solution under illumination were both investigated. For both references, a slight degradation of the intensity appeared after the illumination times, which does not indicate a clear activity under UV-light. This allows any absorption and desorption effects of the dyes at the surfaces to be excluded.

The samples prepared in electrolytes E2, E3, and E5 showed the highest degradation rates in the methylene blue concentration after a 1-day illumination time. The same can be observed for the samples soaked in rhodamine B. After 24 hours, both dyes showed a clear degradation in intensity and therefore in photocatalytic activity. The samples prepared in electrolytes E1 and E5 showed a slightly lower activity in comparison to all other investigated samples,

which becomes clearer for rhodamine B solution. After 24 hours the absorption intensity of rhodamine B solution is lowered to 25% of the starting intensity. Mirelman et al. [27] reported a correlation between high quantities of anatase and high coating thicknesses of PEO-surfaces with a high photo degradation rate. This increases the surface area, and the absorption of UV-photons becomes more likely. The samples produced with higher applied voltages show the highest photocatalytic activity because of increased layer thickness and the presence of quantities of anatase and rutile amounts. The strongest photo activity is seen for sample E3 140 V and sample E5 115, both of which exhibit the two desirable properties of a high anatase content and an increased layer thickness. The samples of electrolyte E3 contain a rutile amount of 15% (130 V) and 31% (140 V) with a ratio of anatase to rutile of 2 : 1 (130 V) and 1 : 1 (140 V) against the optimal ratio of 3 : 1 in comparison to P25. In the case of electrolyte E1, the layer thickness becomes favourable for the activity, while for electrolyte E5 it is not. The PEO-surfaces produced in electrolyte E5 have a lower layer thickness in comparison to other electrolytes. However, there is a similar strong photocatalytic activity of surfaces for electrolyte E5. Sample 115 V E5 shows the presence of rutile already at a low layer thickness, and in this case the crystallinity of anatase and rutile predominates over the effect of the increased specific surface area, which predominates in samples of electrolyte E1. These effects lead to an indication that the presence of rutile phases plays an important role for the photocatalytic activity for PEO-surfaces. In this case, the crystallinity of the surfaces seems to be more purposeful.

Chapter 3: Photocatalytic activity

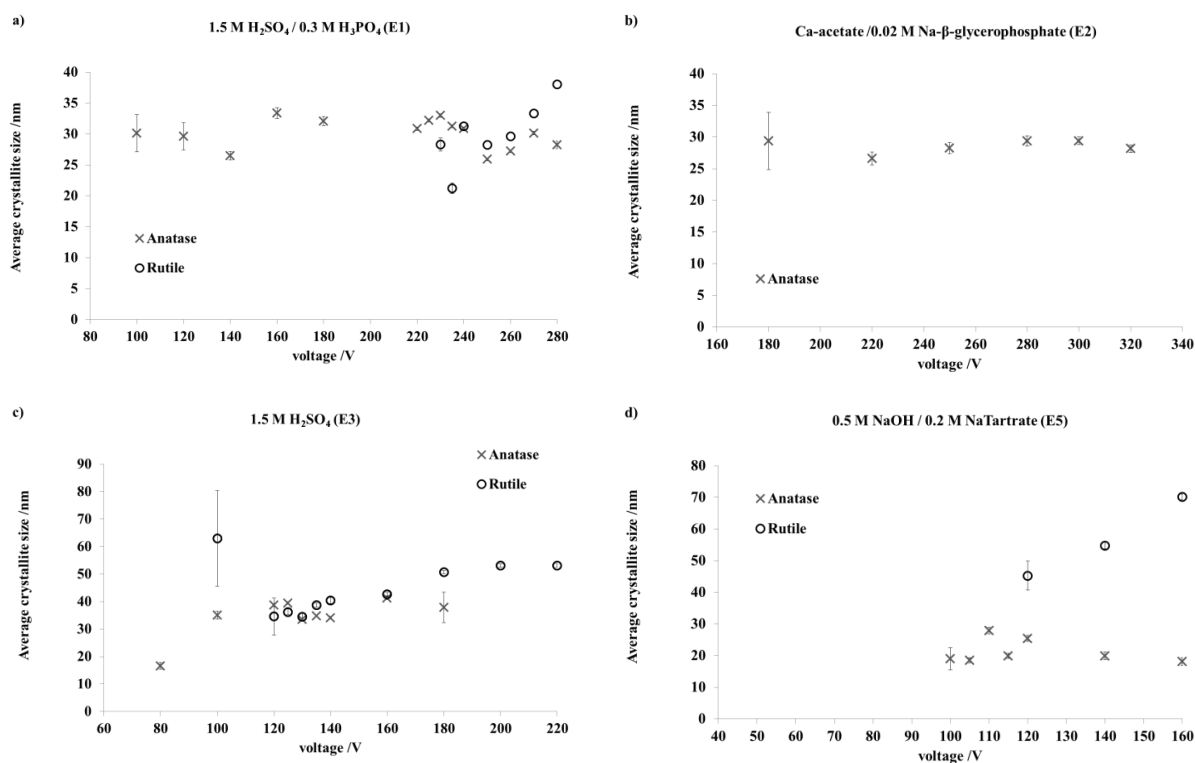


Fig. 36 Average crystallite sizes for anatase and rutile phases on the PEO-surfaces produced in the electrolytes for each applied voltage a) E1 b) E2 c) E3 and d) E5, “Reprinted with permission from Journal Surface and Coatings Technology, 344 (2018) 710–721. Copyright 2018 Surface & Coatings Technology.”

The high applied voltages and the resulting micro-discharges lead to a low crystallite size of the TiO₂ phases. It has been reported that an optimum crystallite size for TiO₂ to show high photocatalytic activity is between 30 and 40 nm [28,204]. The crystallite sizes of all produced PEO surfaces were investigated with Rietveld refinement and plotted in Fig. 36. The samples of electrolyte E3 demonstrate an average crystallite size of the anatase and rutile phases of nearly 35 nm, in contrast to the other PEO-samples with an average crystallite size below 30 nm or above 40 nm. Nanoparticulate crystallite sizes (approx. under 20 nm) gave fewer possibilities for photo-excited interfaces, thus resulting in less photocatalytic activity [205,206]. Therefore, the surface area of “higher” crystallite sizes decreases because of the adsorption of other molecules and the fact that the photo-excited charges cannot reach the surface [28,207]. The occurrence of high amounts of crystalline phases in connection with a crystallite size of 30 to 40 nm has the strongest effect on the photocatalytic behaviour of PEO-surfaces. Kominami et al. [139] have shown that, by increasing the crystallinity and improving the adsorption capacity by increasing the surface properties, it is also possible that brookite act as a photocatalyst. Brookite is the polymorph with the least photocatalytic behavior. In the photocatalytic tests, rhodamine B had a stronger photo degradation rate in contrast to methylene blue, already after 24 hours. In this case, it may be better suited for

checking the photocatalytic activity of PEO-layers after a shorter time period (Fig. 37), and therefore the illumination time could be reduced.

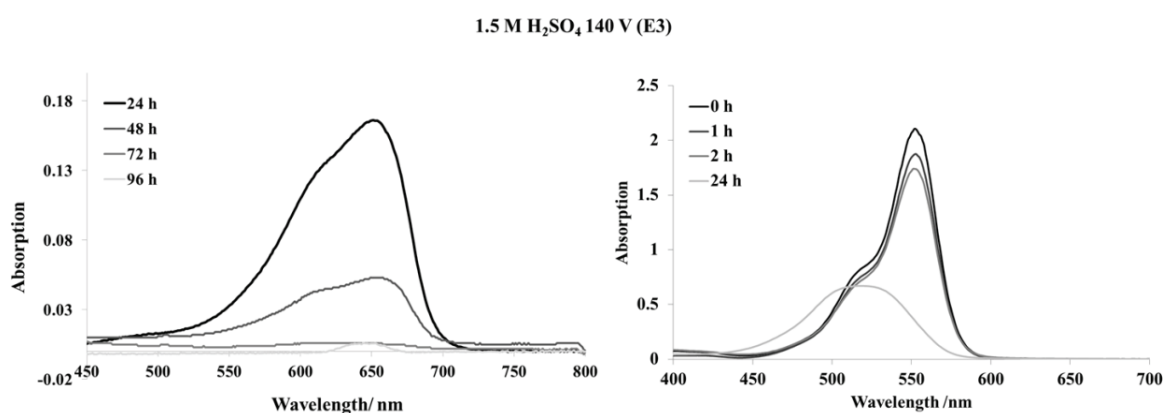


Fig. 37 Comparison of the two degradation spectra of sample E3 140 V (left side) MB (right side) RB, “Reprinted with permission from Journal Surface and Coatings Technology, 344 (2018) 710–721. Copyright 2018 Surface & Coatings Technology.”

The use of different electrolytic systems largely affects the crystallinity and phase composition of the PEO TiO₂ surfaces. Through the type of the electrolyte, the phase composition could be controlled between a ratio of anatase to rutile from 100% anatase to 75% anatase and 25% rutile phases. The different amounts of crystalline anatase and rutile influence the photocatalytic activity, such as the crystallite sizes of both phases. The measured band gaps revealed a direct transition contrary to the expected reported indirect transition of TiO₂, which can be shown by the DASF method. This direct transition resulted in a small crystallite size of 20–30 nm of anatase and rutile. As a result, the band gap shifts to a direct transition. All PEO-surfaces show a photocatalytic activity caused by the high crystallinity of the anatase and rutile phases, and also by the increased surface area. The specific surface area increases because of the small crystallite sizes and the high TiO₂ layer thicknesses as well as the porosity of the PEO-structure. It could also be seen that parts of rutile phases are more favourable for photocatalytic activity, in the cases of samples E1 280 V and E5 115 V. However, a combination of a high amount of anatase and the optimal crystallite size of 30 nm appears to be the most effective combination for increasing the photocatalytic activity. Both can be controlled using the PEO-process in a simple way.

Chapter 4: Biocompatibility

This chapter is based on the investigations shown in the submitted patent in [208].

4.4 Transfer of surface modification using PEO on titanium-coated polymer surfaces

Titanium is a highly biocompatible metal and is used in many applications in medicine, such as for bone or teeth implants. Due to the successful production of pore-rich titanium dioxide structures using plasma electrolytic oxidation and the production of crystalline anatase and rutile phases, the method was also applied to titanium-sputtered substrates. The biocompatibility was investigated with cell adhesion tests to prove the strength of the attachment to the PEO-surfaces. Because of its very suitable mechanical properties, such as a high temperature and chemical resistance, the polyetheretherketone (PEEK) was chosen as a polymer substrate was chosen. PEEK also has a wide range of applications in medicine as an implant material and it is available at a medical grade. Fig. 38 shows the planned application of titanium dioxide layers onto the PEEK substrates and the assessment of the biocompatible properties after plasma electrolytic oxidation.

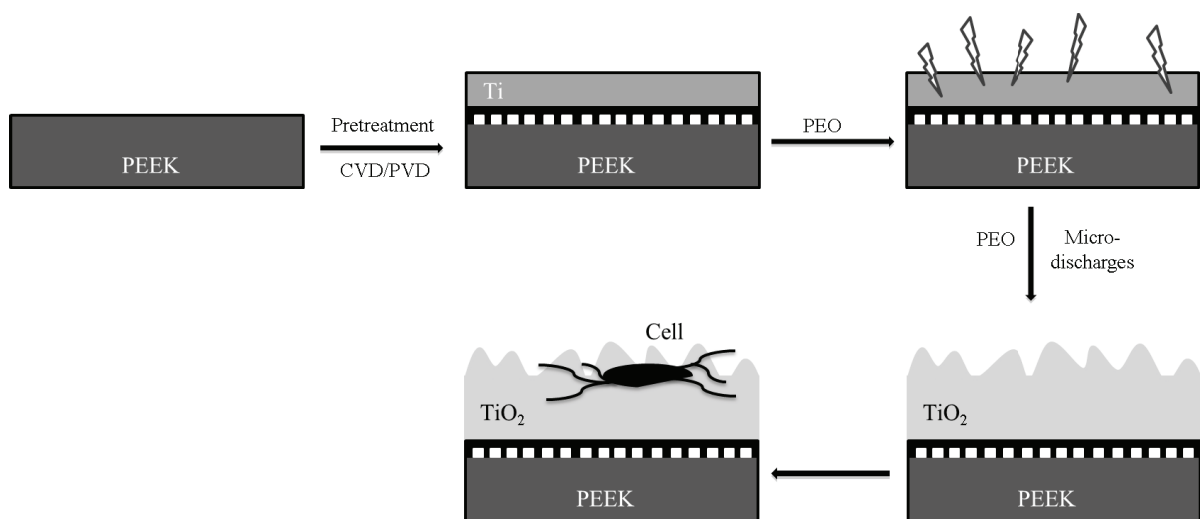


Fig. 38 Schematic illustration for the application of titanium coating and plasma electrolytic oxidation of polymer substrate followed by cell adhesion onto the oxide surface

4.4.1 Bonding strength of the polymer/titanium interface

The application of titanium onto polymer substrates requires a suitable bonding strength of the titanium to the substrate. To optimize the bonding strength, various pretreatments of the polymer surface were investigated. The widely used and certificated pull-off test was chosen to prove the strength of the bond to the surface and the test was conducted according to DIN EN ISO 4624 [231]. Different pretreated PEEK samples with applied titanium coating were selected to measure the adhesion forces of the polymer to the metal coating. This test requires a thermally curable epoxy adhesive (Araldite® 2000+, Huntsman, Swiss), which was attached to the surface, and a circular metal stud with a diameter of 20 mm was chosen. Surface contaminants at the studs were removed using Si-carbide abrasive paper (400 and 2400 grain size), and afterwards the studs were cleaned in isopropanol in an ultrasonic bath. The adhesive was hardened in an oven for up to 48 h at 120 °C. The mechanical strengths were measured by determining the needed force required to break the bond between the coating and substrate using an automatic pull-off machine (PosiTest AT-A, DeFelsko, USA). All pull-off forces for each pretreatment were an average of six single measurements, and four different pretreatments were chosen to strengthen the bonding of the titanium to the polymer surface (Tab. 19). An illustration of a stud applied to the surface can be seen in Fig. 39. The four pretreatment procedures were produced with a special plasma technique and were carried out in an ion-supported high-frequency (HF) plasma polymerization process in a plasma reactor with variable voltages and primer flow. For the subsequent biological investigations, the electrolyte E2 was used for the PEO-process due to the possibility of hydroxyapatite formation in the surface structure during the PEO-process, this is a component of the human bone structure.

Tab. 19: Pretreatment techniques for PEEK with the adhesion strength to the applied titanium layer

Pretreatment	Pull off strength /MPa
PEEK without pretreatment	1,71 ± 0,12
PEEK+ titanium layer without pretreatment	3,45 ± 0,45
Plasma activation	3,05 ± 0,90
Plasma etching	3,54 ± 0,46
SiO ₂ layer	4,55 ± 0,32
SiO ₂ layer (BIAS)	> 4,25 ± 0,29

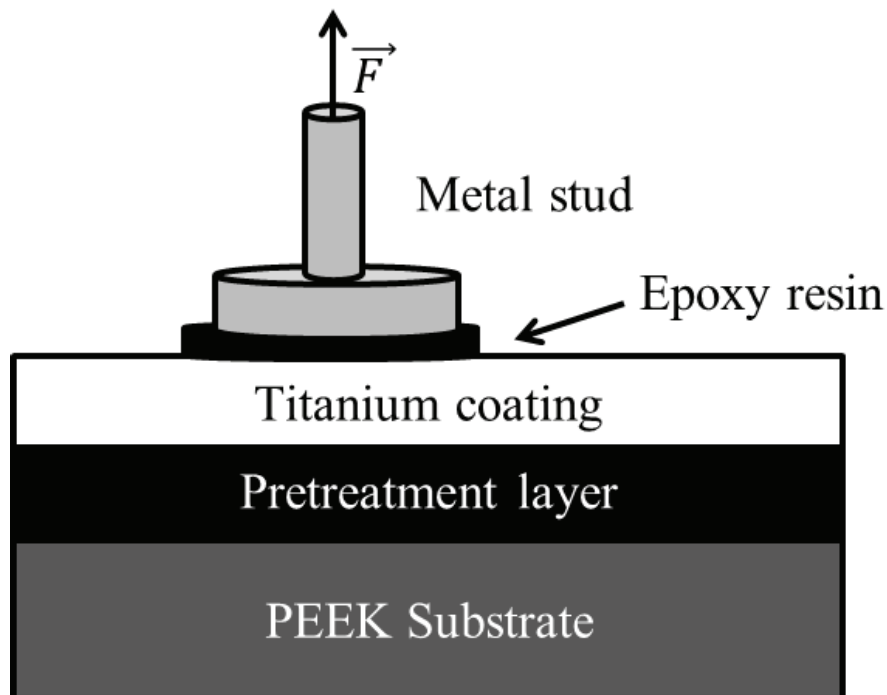
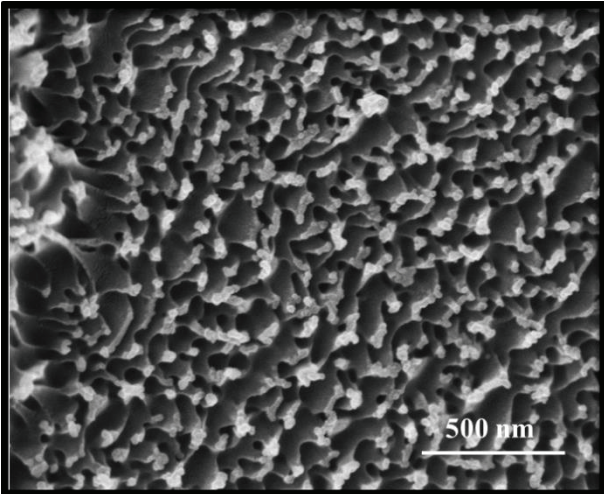
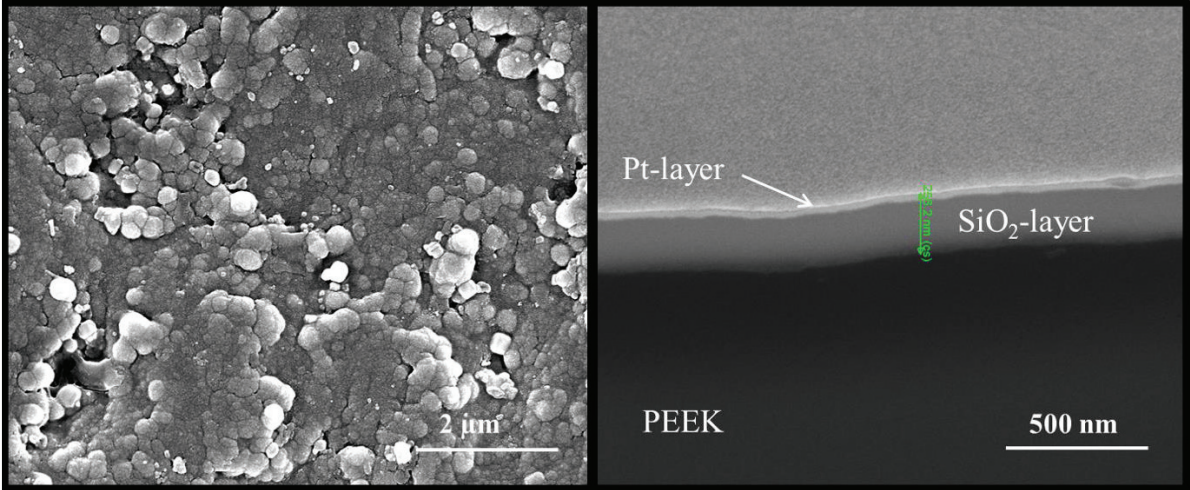


Fig. 39 Pull-off test arrangement for measuring thin film adhesion strength

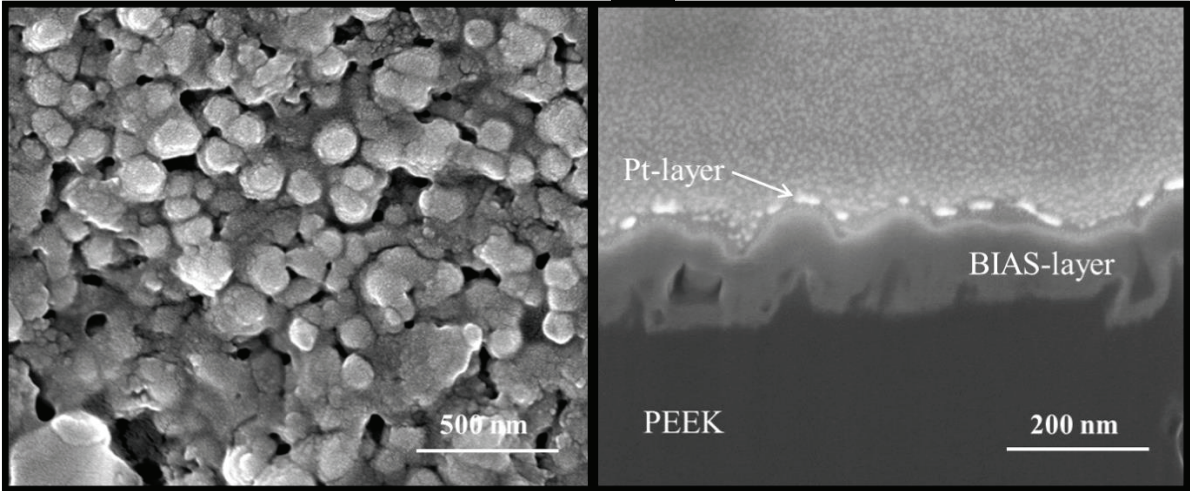
For the plasma activation technique, the PEEK molecules were activated into ion species with the plasma species generated in the reactor. With these activated ions, the titanium layer should be chemically bonded to the PEEK molecules. With the plasma etching process, the surface of the PEEK substrate was roughened on a micrometer scale, as seen in Fig.40. The last two pretreatments are performed in a similar way with hexamethyldisiloxane (HMDSO) and oxygen as a precursor. The difference in the process was the applied voltage, whereby the second process was carried out with very high voltage of 800 V, which is known as BIAS. For this BIAS SiO_2 coating, Fig. 40 shows a clear SiO_2 layer thickness with a mechanical anchoring to the PEEK substrate.



Plasma etching



SiO₂-layer

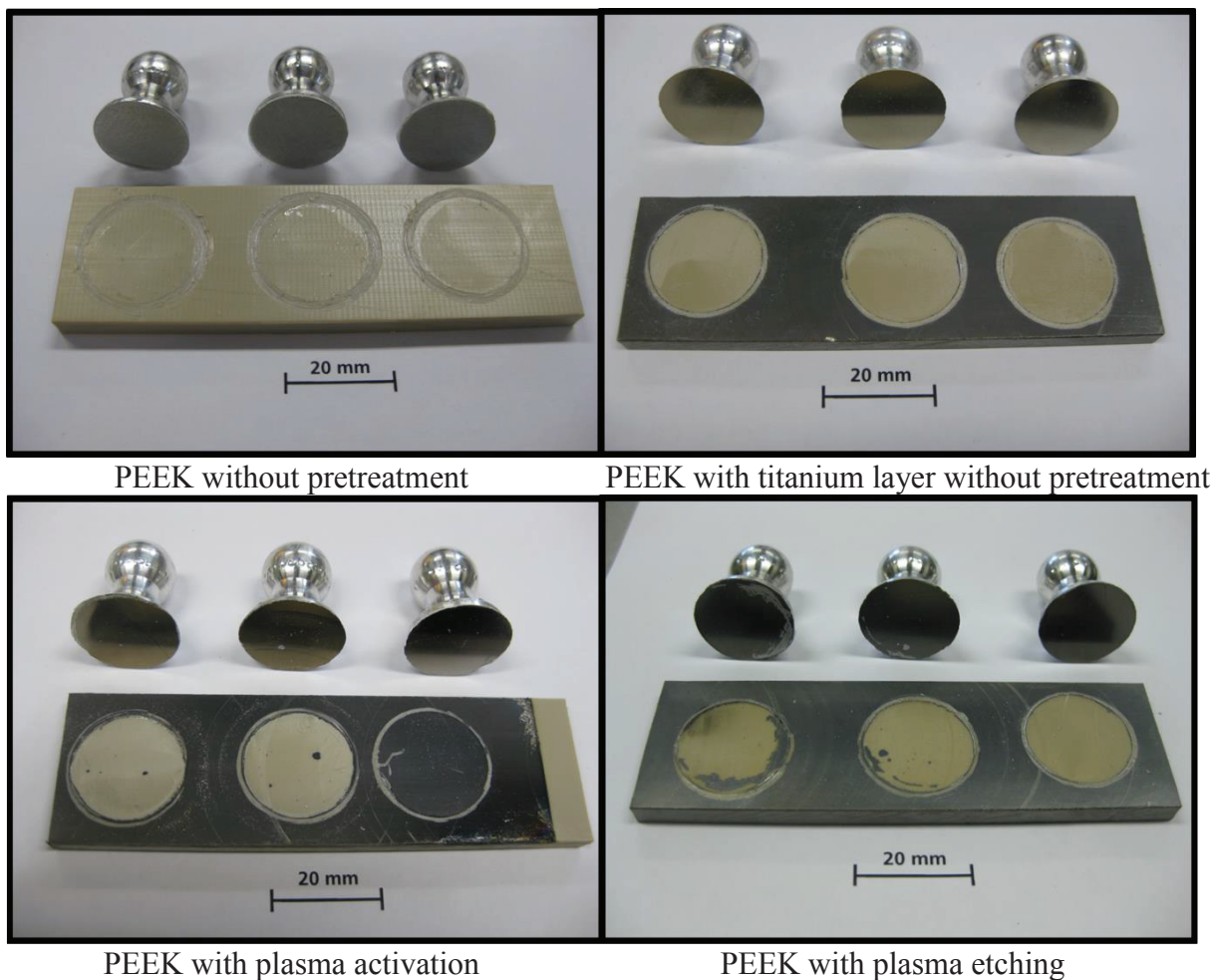


BIAS SiO₂-layer

Fig. 40 Pretreatment of the PEEK substrate with plasma etching (first row), SiO₂-layer (middle row), and BIAS SiO₂ layer with the mechanical interlocking in the substrate (last row)

Chapter 4: Biocompatibility

In Tab. 19 it can be observed that there is no difference in the pull-off strength of plasma activation and plasma etching to the PEEK substrate without any pretreatment with a measured pull-off force of 3.0 to 3.5 MPa. The plasma activation and etching process roughened the PEEK surface, which is why the roughness is not sufficient to strengthen the attachment of the titanium coating. In comparison, both SiO₂ layers show a relatively high pull-off force of approx. 4 MPa from the PEEK substrate. After the test, the pretreatments showed an adhesion break between the titanium layer and the PEEK substrate (Fig. 41). Hereby, the BIAS layer showed a clearly visible cohesion break with the PEEK substrate, as seen in Fig. 42, and should be marked as a value of over >4.25 MPa. The combination of SiO₂ bonding to the titanium atoms and the mechanical anchoring to the PEEK substrate seems to be the reason for the strong adhesion of titanium to PEEK. The cohesion break indicates an acceptable bonding strength of the BIAS layer as an adhesion promoter for medical applications. Therefore, this kind of interlayer was used for the subsequent PEO-process between titanium and PEEK.



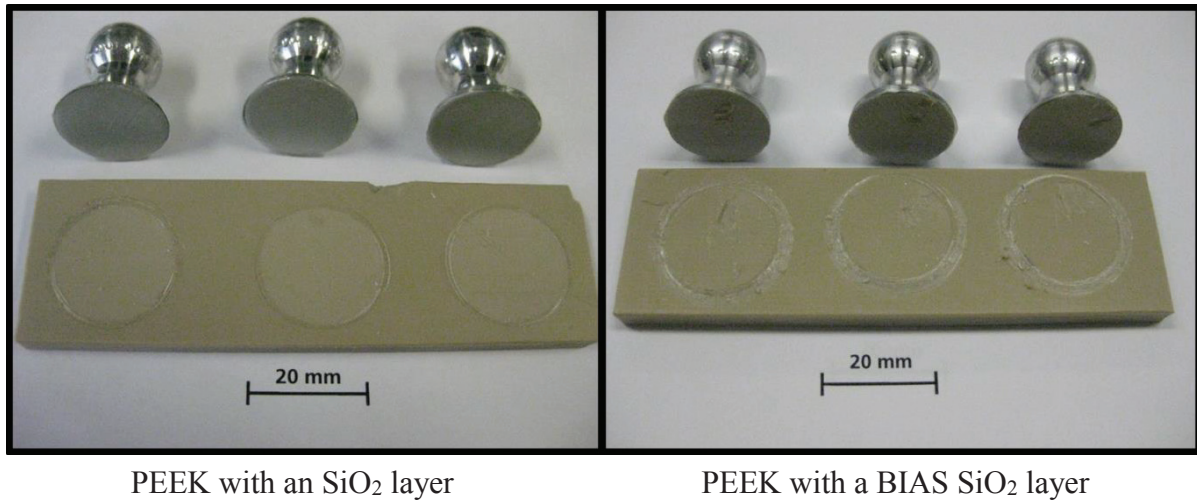


Fig. 41 Images of the pull-off tests of various pretreatment techniques of PEEK: Pretreated PEEK substrates at the bottom of the pictures and on top the pulled studs; the round areas are the pulled-off areas

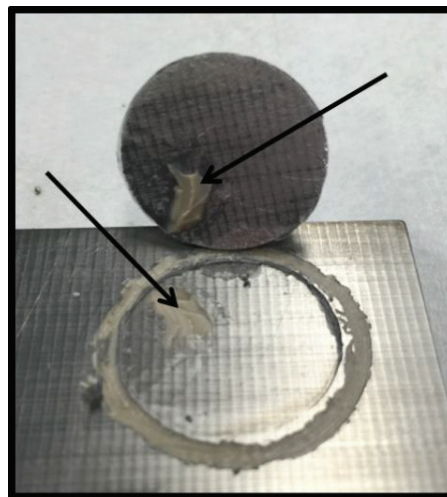


Fig. 42 Cohesion fracture in the substrate (marked with arrows)

4.4.2 Plasma electrolytic oxidation on titanium coatings on PEEK substrates

Before starting the oxidation process, the PEEK substrates were grinded with SiC-paper (grit: 320, 2400, 4000) and cleaned with isopropanol. The PEEK substrates were coated with titanium on one side, according to section 3.2.8, and the plasma electrolytic oxidation was performed on the PEEK substrates, according to section 3.3.1 at the PEEK substrates. The substrates were metallized in the plasma reactor within 2 h with a layer thickness of nearly 4 μm . This layer thickness value was chosen based on the micrographs of the layer thicknesses produced on the titanium substrates in Fig. 22. Thus, the layer thickness at 300 V for E2 reaches almost 4 μm , which is necessary to form the titanium dioxide layer without reaching the PEEK substrate during the PEO-process. For the following investigations on biocompatibility, only electrolyte E2, with the composition of 0.2 M $\text{Ca}(\text{C}_2\text{H}_3\text{O}_2)_2$ and 0.02 M

$\text{Na}_3\text{H}_7\text{O}_6\text{P}$, was used. This electrolyte is known in the literature to form hydroxyapatite in the oxide layer during the PEO-process [165,172,209].

For the oxidation processes, another experimental setup was used with a two-electrode circuit was used. The used measuring cell was made of a PTFE tube with a hole of 1 cm in diameter. This tube was placed on the titanium-sputtered side of the PEEK substrate and strongly pressed between two plates with four screws. The sputtered PEEK side was connected as the working electrode with a thin steel plate, and a platinum plate which was soaked into the electrolyte was used as the counter electrode. The PTFE tube was filled with approx. 11 ml of electrolyte solution. Afterwards, the titanium dioxide layers were produced using the plasma electrolytic oxidation procedure on the coated substrates. A schematically illustration of the PEO-setup is shown in Fig. 43.

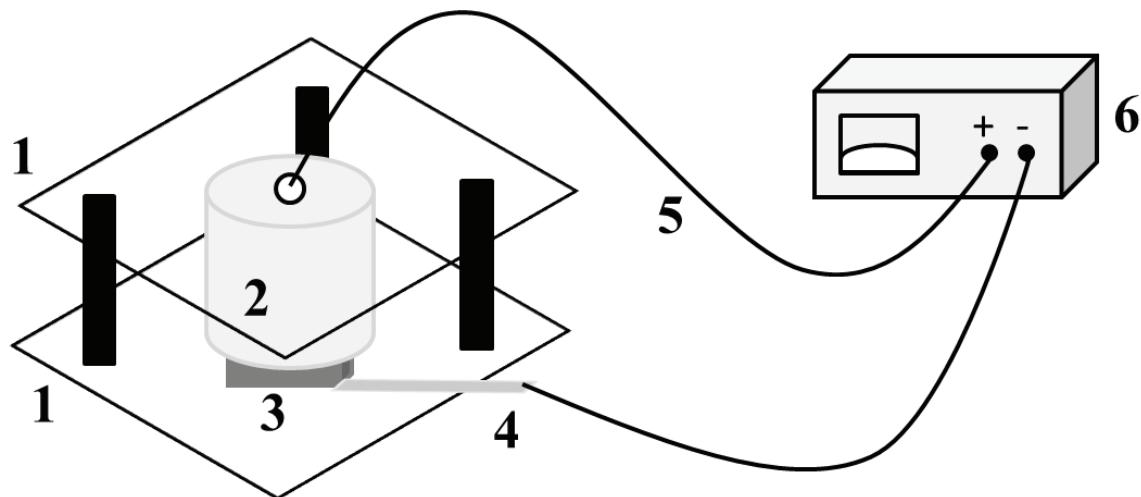


Fig. 43 Setup for the PEO-process at the coated PEEK substrates, 1) plates with screws for fixing, (2) PTFE tube filled with electrolyte solution, (3) PEEK substrate, (4) steel plate as a connection to the PEEK substrate, (5) cable to counter electrode, (6) power supply

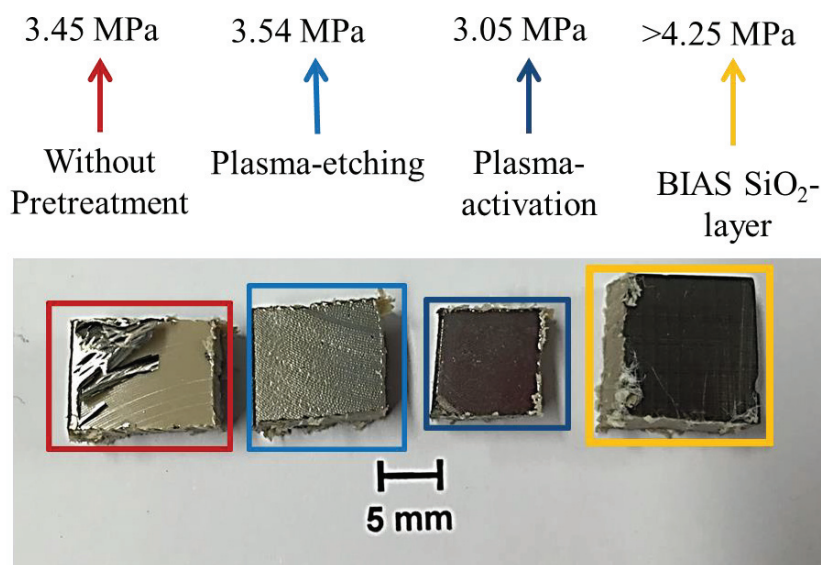
4.4.3 Aging resistance of the titanium coating

After a successful application of a resistant adhesion promoter to the PEEK surface, the aging resistance of the titanium coating was investigated for an aqueous solution and under human body conditions. For this, the simulated body fluid solution was used according to Kokubo et al. [210]. The solution contained similar inorganic ion concentrations as the extracellular body fluid and simulated human body conditions. The compositions in comparison to the blood plasma as well as the used amounts are listed in Tab. 20. The samples were outsourced in SBF solution for six months in a closed beaker filled in a warmed oven at 310 K.

Tab. 20 Comparison of the composition of simulated body fluid and human blood plasma with the as used chemicals

Ion	Concentration /mmol·dm ⁻³			Amount /g·L ⁻¹
	Human blood plasma	SBF	Chemical	
Na ⁺	142	142	NaCl	7.669
K ⁺	5	5	KCl	0.224
Mg ²⁺	1.5	1.5	MgCl·6H ₂ O	0.305
Ca ²⁺	2.5	2.5	CaCl ₂	0.278
Cl ⁻	147.8	103	NaCl, KCl, CaCl ₂	-
HCO ₃ ⁻	4.2	27	NaHCO ₃	0.350
HPO ₄ ²⁻	1	1	K ₂ HPO ₄ ·3H ₂ O	0.174
SO ₄ ²⁻	0.5	0.5	Na ₂ SO ₄	0.071
(CH ₂ OH) ₃ CNH ₂	Tris(hydroxymethyl)aminomethan: Buffer for pH			6.057

The four pretreated PEEK samples after six months are shown in Fig. 44. After six months, all the samples with a previous pretreatment of the PEEK substrates showed no visible spalling of the titanium coating. Without any pretreatment, the titanium coating clearly pulls off from the surface of the PEEK substrate. This indicates the necessity of pretreatment before an application of titanium. A pretreatment promotes a successful implantation due to a failure of wear to appear after implantation. PEEK includes ether- and carbonyl groups, which can improve the bonding of titanium ions. Titanium has a high affinity to oxygen molecules, which can catalyze the bonding of titanium to the functional groups of PEEK and the added SiO₂ layer.

**Fig. 44** Different pretreated PEEK substrates outsourced in simulated body fluid (SBF) for six months at 37 °C in an atmospheric oven

Plasma electrolytic oxidation is a high-energy performing surface treatment due to the resulting micro-discharges on the surface. These energy-rich discharges have a strong influence on the surface composition, which can also have an influence on the polymer substrate underneath the titanium layer. Therefore, the PEO-treated sputtered PEEK substrate was measured with XPS measurement with regards to the molecules on the surface. The XPS measurement can help to exclude a transport of PEEK molecules into the titanium oxide layer. Three samples were measured: A pure PEEK substrate, a titanium-sputtered PEEK substrate, and a PEO-treated PEEK substrate (electrolyte E2, 300 V). The XPS spectra can be seen in the following figures (Fig. 45 - Fig. 47), and the atomic compositions at the top of the surfaces are summarized in the following tables (Tab. 21 - Tab. 23). The important atoms are marked in the tables.

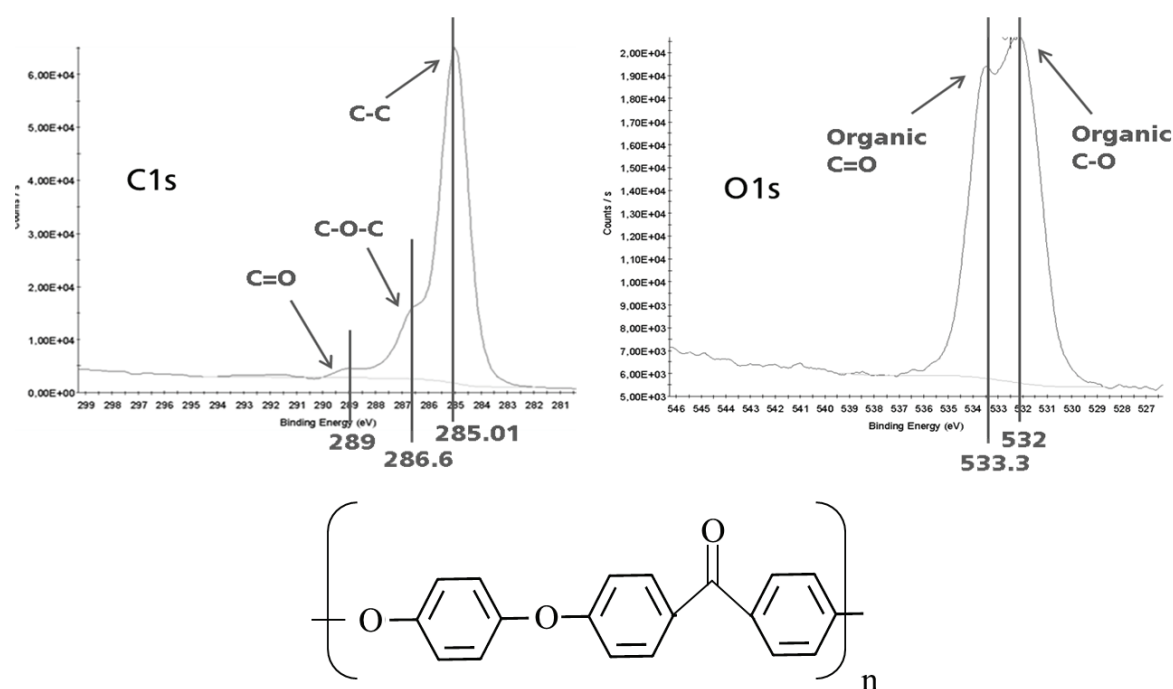


Fig. 45 XPS spectra of C1s (left) and O1s (right) mode of a pure PEEK-substrate and the molecular structure of polyetheretherketone (bottom)

Tab. 21 Atomic percent of the included atoms on the measured pure PEEK substrate: Marked columns show the important atoms for the sought substance

(at %)	C	O	N	Si	Ti	Ca	P	Cl	S	Na	K
Position 1	82.4	15.1	0.9	0.4	-	0.7	-	0.1	0.3	0.2	-
Position 2	82.5	14.2	1.1	0.5	-	1.0	-	0.2	0.2	0.2	-

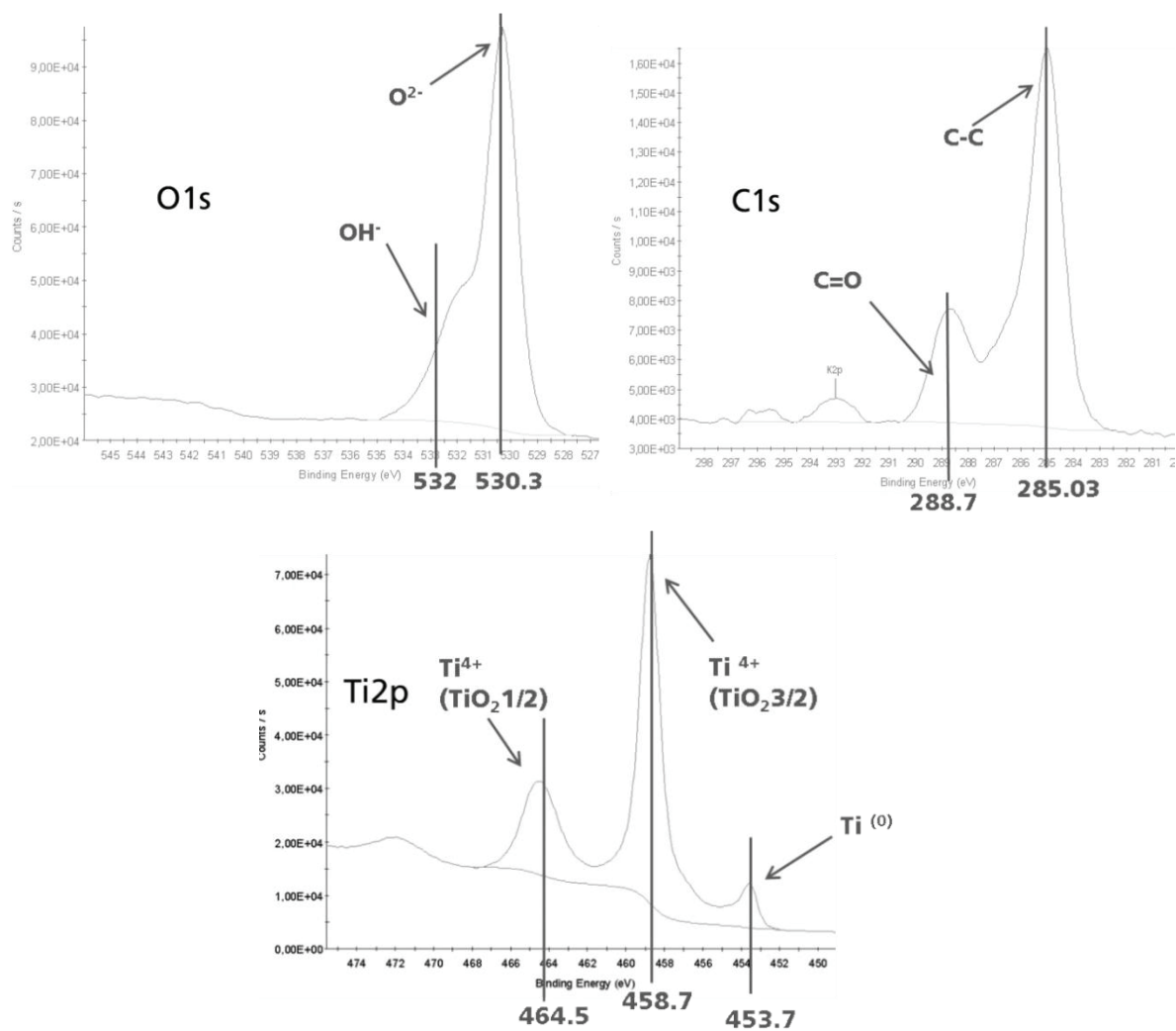


Fig. 46 XPS spectra of C1s (left), O1s (right), and Ti2p (bottom) modes of a PEEK substrate with an applied titanium layer

Tab. 22 Atomic percent of the included atoms on the measured PEEK substrate with the applied titanium layer: Marked columns show the important atoms for the sought substance

(at %)	C	O	N	Si	Ti	Na	K
Position 1	24.7	50.5	1.2	0.2	22.7	0.4	0.3
Position 2	24.6	50.1	1.3	0.5	22.8	0.4	0.3

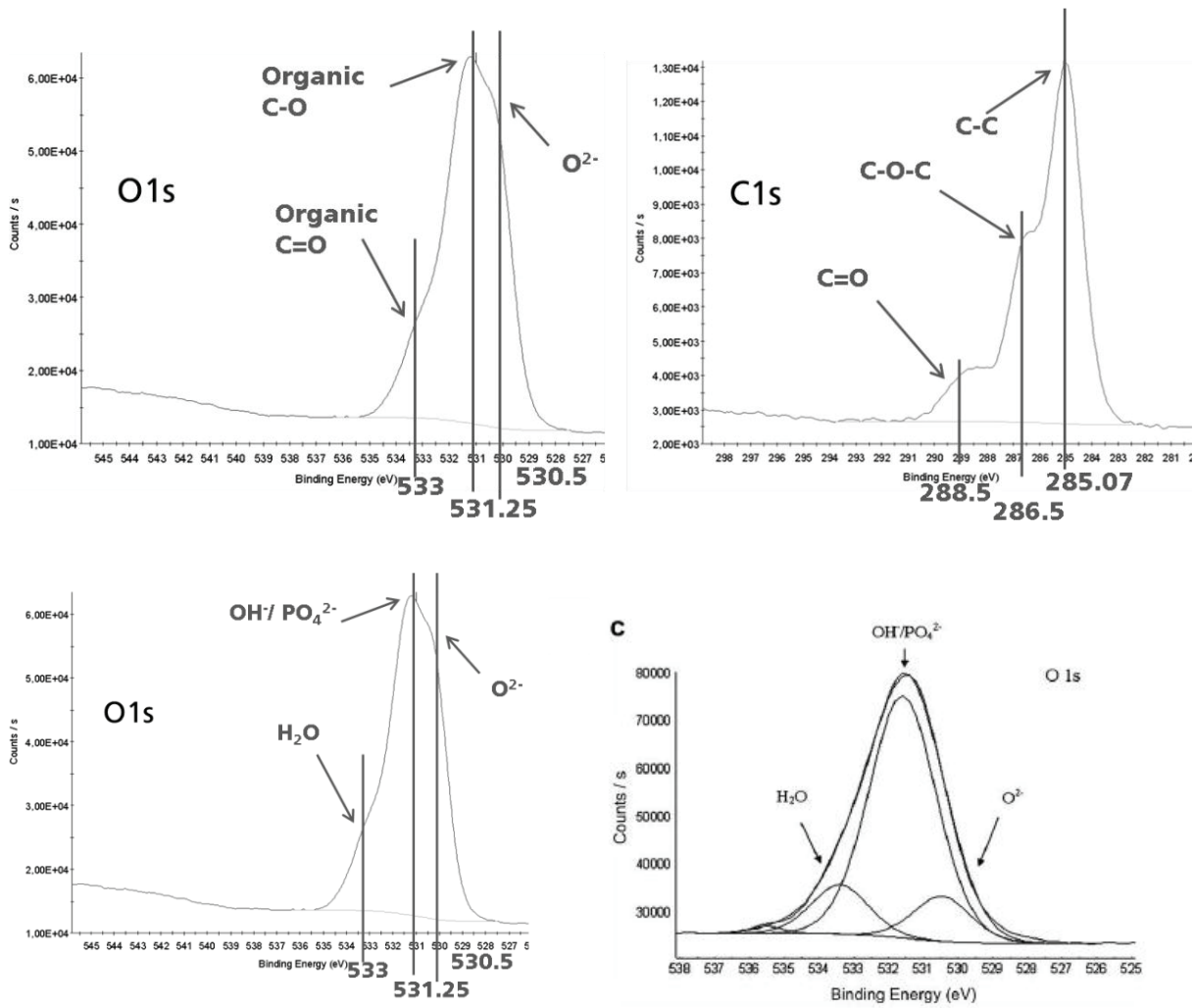


Fig. 47 XPS spectra of and O1s (left, bottom), C1s (right) modes of the PEEK-substrate with a PEO oxide layer and a reference spectra, according to Barker et al. [164] (bottom)

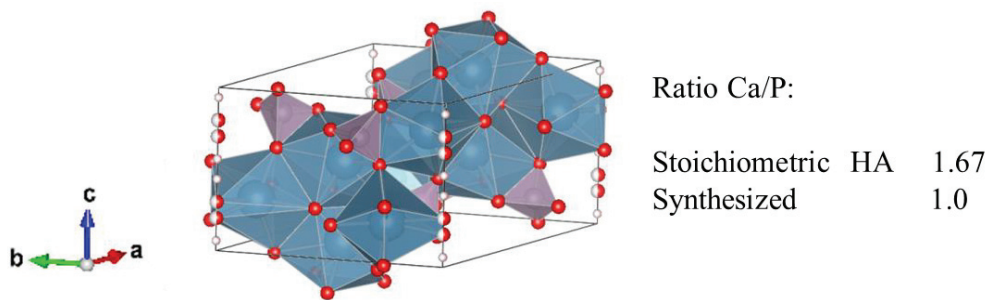
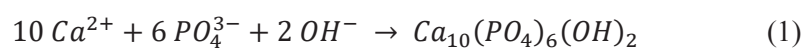


Fig. 48 Crystal structure of hydroxyapatite with the natural and synthesized ratio of calcium and phosphorus contained in the oxide layer

Tab. 23 Atomic percent of the included atoms on the measured PEEK substrate with the treated PEO-coating: Marked columns show the important atoms for the sought substance

(at %)	C	O	N	Si	Ti	Ca	P
Position 1	23.3	52.5	0.2	0.2	6.7	8.9	7.6
Position 2	23.4	51.5	0.6	0.3	10.7	6.3	6.5

The XPS spectra for the pure PEEK substrate show all structure related organic bonds. The characteristic carbonyl group at 289 eV and the ether bonds at 286 eV in the C1s spectra can be observed. The O1s spectra of the PEEK substrate show the related C-O bonding at 532 eV and the carbonyl group band at 533 eV. These peaks show the corresponding bonds in a PEEK molecule and should not be identified in the XPS spectra of the PEO-treated samples. However, an absence of other atoms, except oxygen and carbon, leads to a pure PEEK substrate. In the next step, a PEEK substrate with a sputtered titanium coating was measured and the resulting XPS spectra of the C1s, O1s, and Ti2p modes and the atomic-% of the contained atoms on the surface can be seen in Fig. 46 and Tab. 22. The spectra of the C1s and O1s modes show no organic compounds on the surface of the sample. The visible and measured carbon atomic percent represents an acceptable amount of impurities over the entire treatment time. The oxygen atomic percent in Tab. 22 show a titanium to oxygen ratio of 1:2 and the Ti2p spectra show Ti⁴⁺ bonds at 458 eV and 464 eV at top of the surface. A naturally formed titanium dioxide bonding can still be confirmed with the O²⁻-peak in the O1s spectra at 530 eV. The titanium spectra also show a metallic titanium peak at 453 eV, which relates to the sputtered coating. In the measurement of the PEO-treated PEEK substrates, there a C1s spectra similar to those of the pure PEEK substrate can be seen. On the other hand, the O1s spectra contain a shifted double peak with a shoulder at the left side of the peak. The shoulder at 533 eV normally relates to the organic C-O double bond. However, the peak at 530 eV relates to an O²⁻-species that is the part of the titanium dioxide layer. In comparison with some XPS measurements by Baker et al. [164], the shoulder at 533 eV relates to some H₂O on the surface, which can be explained by the occurrence of some stored water molecules inside of the PEO-pores due to the high hydrophilicity of titanium dioxide. The O1s peak at 531 eV shows the OH⁻ and PO₄³⁻ species at the surface. Therefore, the whole O1s spectrum isn't similar to the organic compounds of the PEEK substrate. The O1s spectra show the presence of hydroxyapatite at the PEO-surfaces, which can be also seen in Tab. 23.

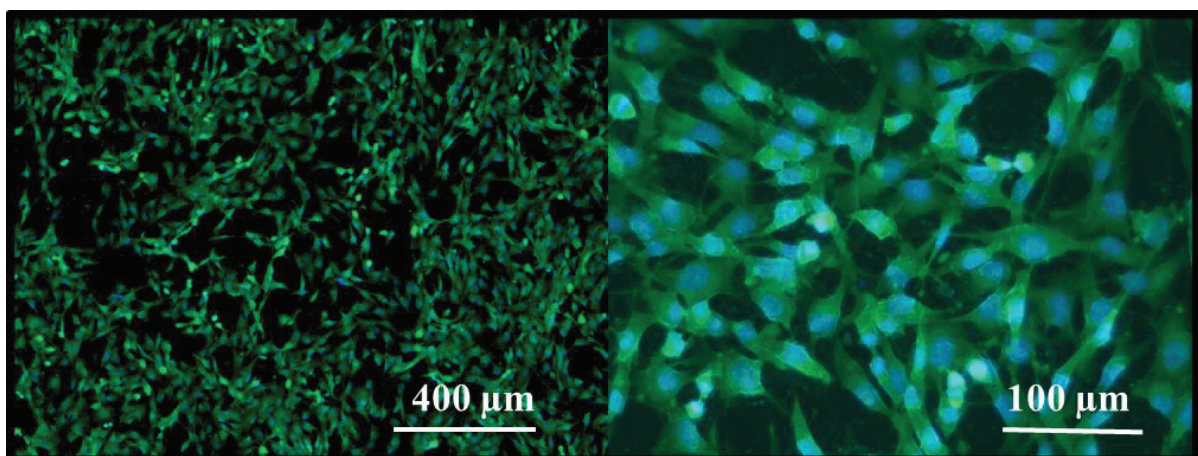


The surface contains calcium and phosphate atoms, which confirm the assumption of the presence of hydroxyapatite. the formation of hydroxyapatite HA is shown in equation (1) and illustrated in Fig. 48. The measured ratio of calcium to phosphate atoms is nearly 1.0 whereby natural stoichiometric HA has a ratio of Ca/P of 1.67 [211]. At the very least, the PEO-process produces HA in the titanium dioxide layer which can improve its biocompatibility.

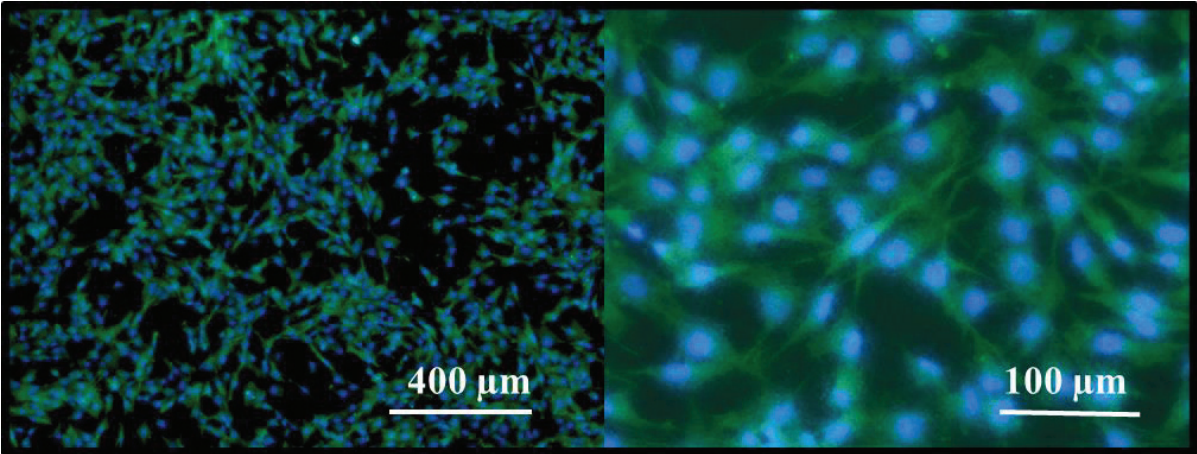
4.4.4 Cell morphology and settling on PEO-surfaces

The biocompatibility of the produced thin PEO-coatings on PEEK was first investigated with the application to humanoid osteoblasts MG-63. The morphologies and the amount of these applied bone cells were documented after 24 h of incubation time. The cell cultures were settled on the different surfaces and the cell counts were performed with nine similar samples at three different points on the sample surface. The cell counting area of each sample amounted to 0.6 mm^2 . The fluorescence micrographs of an exemplary sample of each status are shown in Fig. 49. Because of the auto-fluorescence of the PEEK substrates, the required micrographs have been produced in a different light mode of the used microscope. This auto-fluorescence is an inherent property of the polymer and is caused by some fluorescent additives [212].

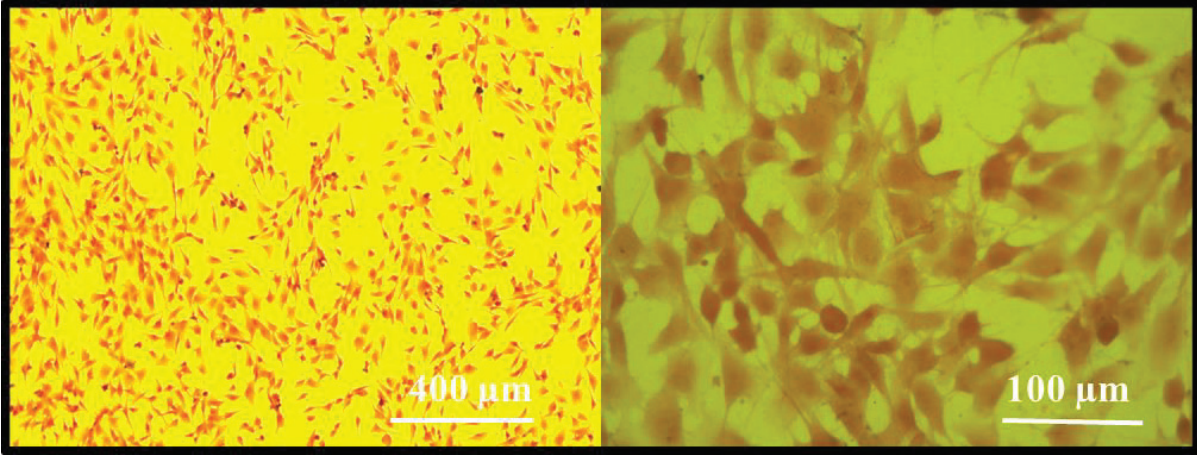
The PEEK samples were stained by adding 2 mL H+E (Hoechst 33342 special formulation) and 10 min of incubation time. In Fig. 49 the cell filaments are colored green while the nuclei are blue. In addition to the fluorescence micrographs, the cell spread along with the calculation of the cell's covered area was analyzed. Titanium substrates are used in medicine because of their good biocompatible properties, which is why titanium was used as a positive reference to show a desirable adhesion to the surface. The pure PEEK substrate was used as a negative reference. The seeded cell density was $1 \cdot 10^5$ cells per well. The PEEK samples had a greater height (5 mm) than the titanium samples (1 mm) and therefore 2 mL cell suspension was used instead of 1 mL for the thin titanium samples were used. The cell numbers and covered surface areas were measured with the commercially available software ImageJ (Version 1.48v National Institute of Health, USA).



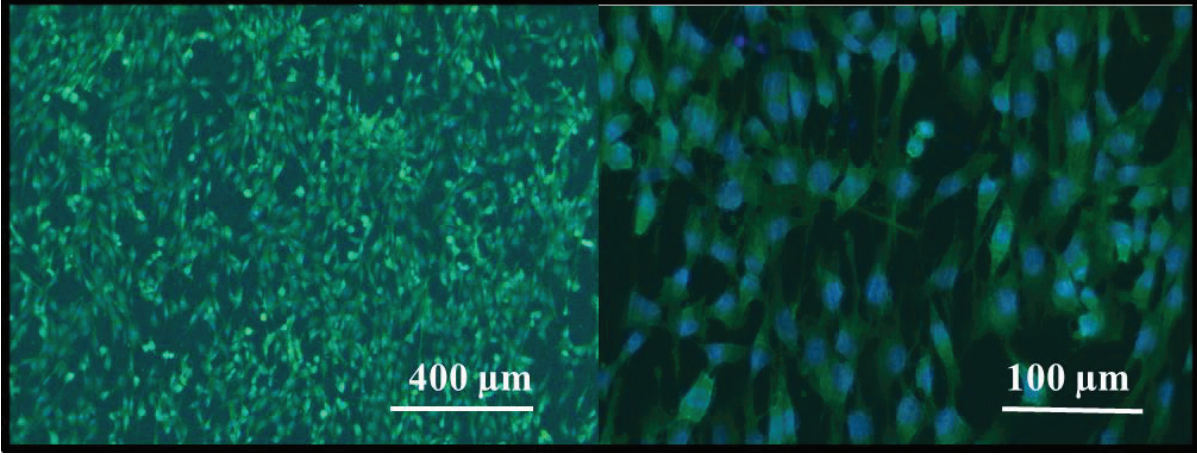
Titanium



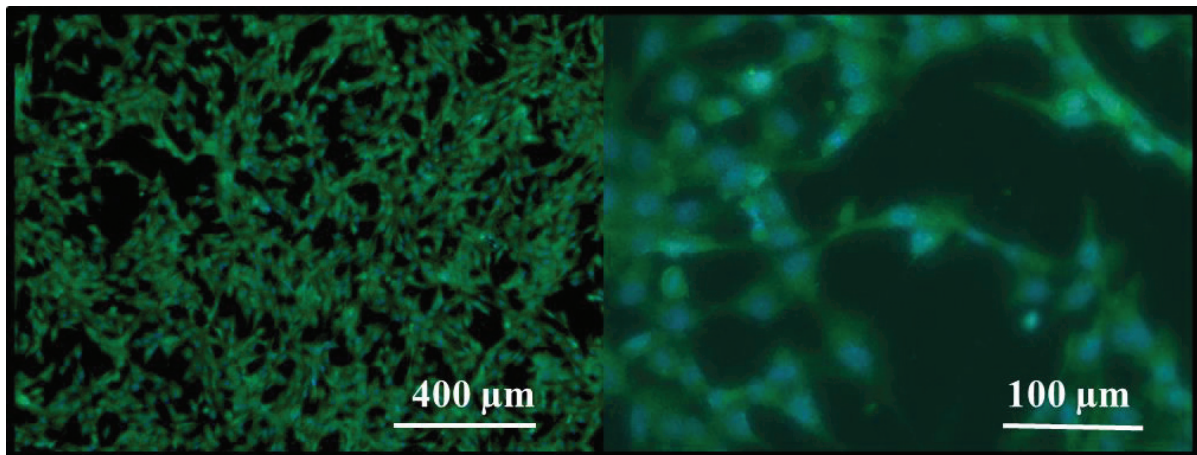
Titanium + PEO



PEEK



PEEK + Titanium



PEEK + Titanium + PEO

Fig. 49: Fluorescence micrographs of the attached osteoblasts at the different surfaces in two magnifications (left micrograph) 50x, (right micrograph) 200x; (nucleus: blue, cell body: green); micrographs show the five different conditions of the investigated surfaces: (first row) pure titanium substrate, (second row) titanium substrate with applied PEO-layer, (third row) pure PEEK substrate, (fourth row) PEEK substrate with applied titanium layer, (fifth row) PEEK substrate with applied PEO-layer

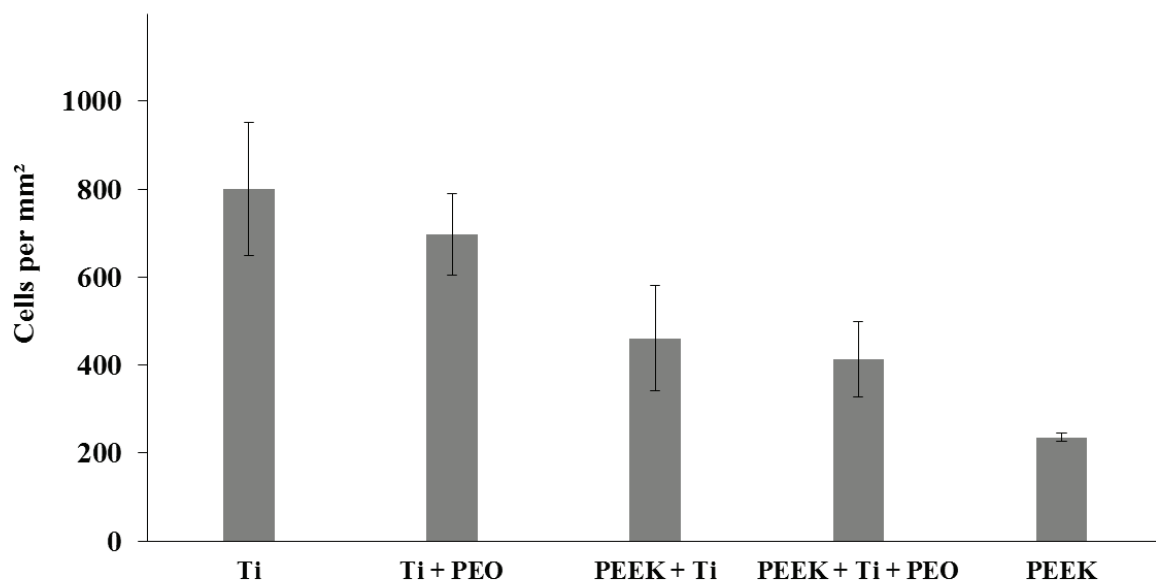


Fig. 50 Nuclei counting of the cell seeding on the five different surfaces; error bars show the divergence of attached cells on the different surfaces

On all surfaces, the cell morphology looked similar, and the cell bodies are completely spread across the surface while the cell filaments seem to be anchored with the surface. Apart from the PEEK surfaces, the cell number seems to be less than on the other surfaces, as can be seen in the micrographs. From the micrographs, no concrete statement about the difference of the surfaces can be made because of a complete spread of the cell filaments onto the different surfaces. Therefore, the number of cell nuclei was counted. The counting of the cell nuclei seen in Fig. 50 did not lead to a meaningful result for the cell attachment. The counting

showed a high cell number for the titanium and titanium PEO-surfaces. The PEEK surfaces with titanium and with PEO-coating showed an almost identical cell number to each other. Only the pure PEEK surfaces showed a clearly reduced cell number due to the lower biocompatibility of polymer substrates in contrast to metallic surfaces. The very low difference in cell number can be an indication that all surfaces have no negative influence on cell behavior. After the counted nuclei, the covered surface area of the samples was measured (Fig. 51).

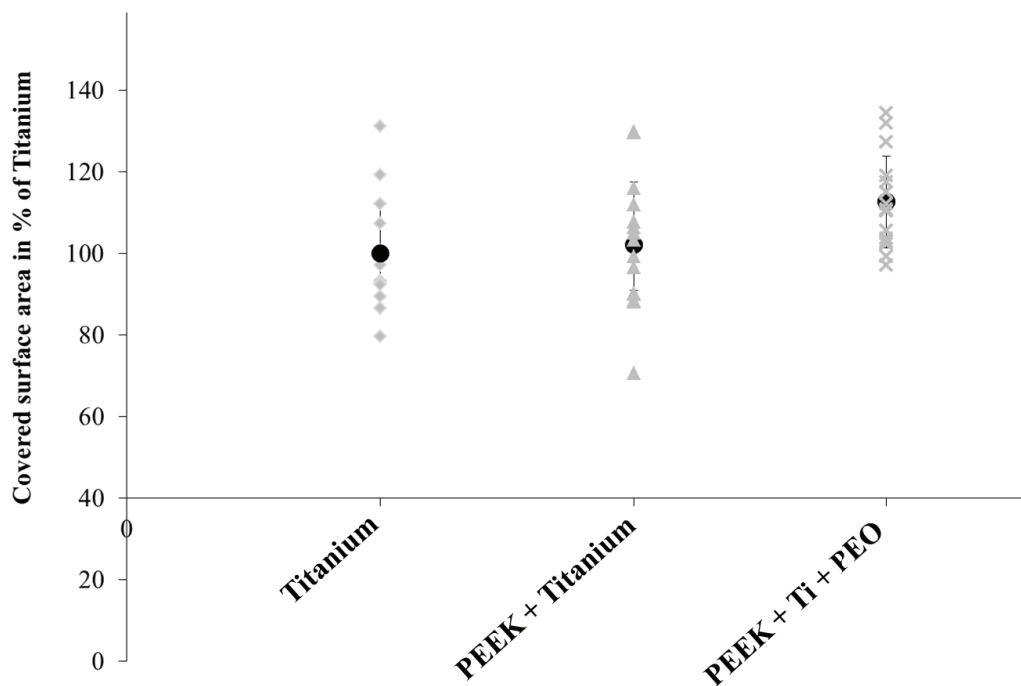


Fig. 51 Covered surface area in % of the examined PEEK samples

The covered surface areas of titanium-coated PEEK, PEO-treated PEEK, and a titanium sample as reference material were measured. Eight samples from each state were measured respectively. There were also no clear differences between each state, including the resulting error. All samples were in a range of $\pm 20\%$ of the covered surface area of the titanium reference. Regardless of the consideration of the individual value of the PEO-treated PEEK substrate in electrolyte E2 300 V, a higher covered surface area of the seeded cells of +15% can be seen. This slight tendency can be explained by the fact that the composition of the titanium dioxide layer includes some HA phases, which are similar to those of the bone structure. The proteins of the osteoblasts first come into contact with the surface for adhesion first. Furthermore, Kim et al. [213] found an improved cell adhesion on PEO-treated surfaces with amounts of HA in comparison to pure titanium surfaces. Electrolyte E2 produces

amounts of HA on the PEO-surfaces, and this hydroxyapatite can have a positive effect on cell adhesion.

More or less structured and rough surfaces enable the cells to attach to the surface structure as well as to adhere stronger at those surfaces. Urselmann et al. [214] compared the cell morphologies at different metal surfaces and found that the cell filaments on smooth surfaces show a small star-like structure, whereby the cells have to spread across the whole surface for adhesion similar to surfaces of titanium and PEEK. On rough surfaces the cells spread irregularly and can anchor to the surface structures, which are represented by the PEO-pores [215]. In addition, a long-termed adhesion can be achieved with a structured and rough PEO-surface [216].

4.4.4.1 Strength of cell-adhesion on PEO-surfaces (vertical flow assay)

Due to incomplete results of the cell counts, a different test for evaluating the cell adhesion was chosen. Hereby, a newly developed method (vertical flow assay) was used [178]. The setup of the vertical flow assay has been investigated in a previous study by N. Suter and B. Heim [217,218]. The setup used is shown in Fig. 52. As according to section 3.3.6, a PBS solution was pressed through a tube with a constant flow rate by means of a syringe pump vertical to the sample surface. The optimal flow rate and the distance of the cannula to the sample was set as 1800 mL/h and 6 mm, respectively, and were developed in a previous study [218]. At a low distance of 3 mm and a low flow rate of 1200-1500 mL/h, the sample surfaces were rinsed irregularly, and the errors were spread across a high range of values.

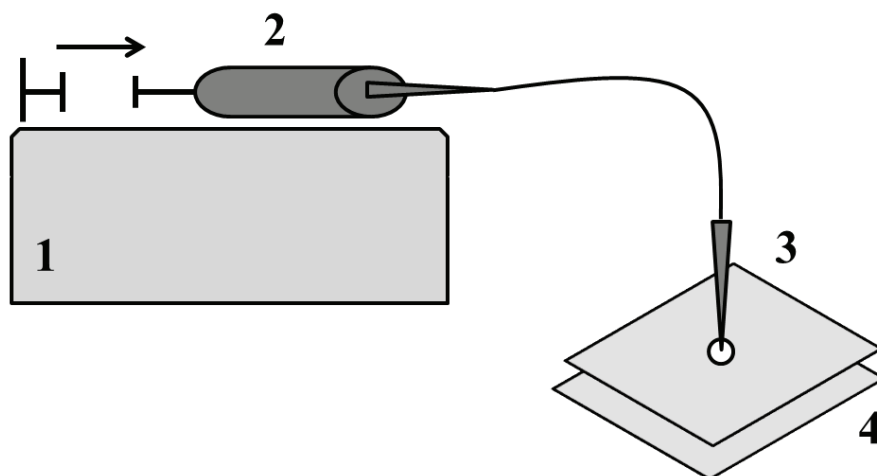


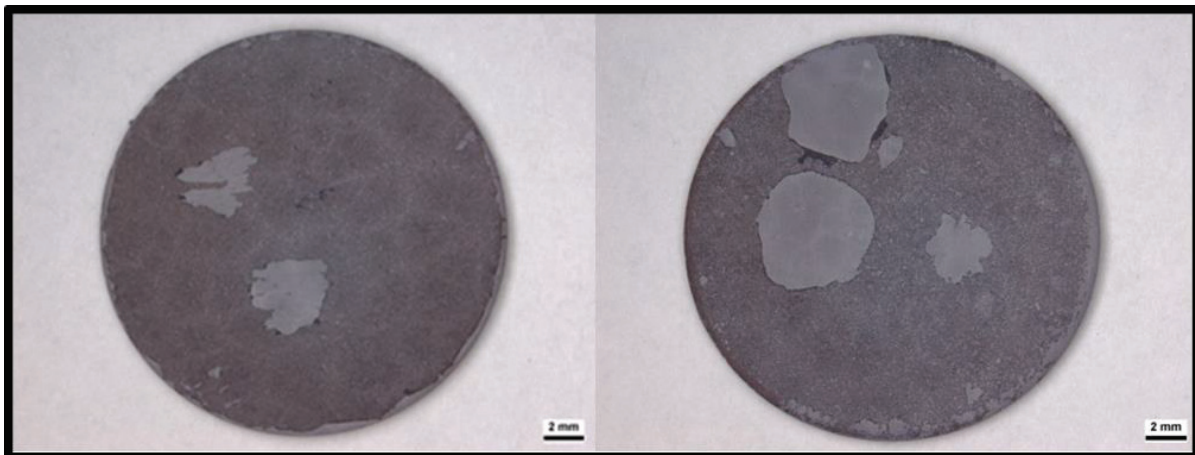
Fig. 52 Setup of the vertical flow assay established in a research work and master thesis (1) syringe pump (2) syringe with PBS solution (3) cannula (4) titanium holder with cell sample according to [217,218]

Chapter 4: Biocompatibility

For the vertical flow assay, the same cell cultures of osteoblasts MG-63 were used as for the fluorescence investigations, with a seeded cell number of $1 \cdot 10^5$ cells per mL. The cells were incubated for 48 h in a humanoid atmosphere. The cytoskeletons were colored with the red dye carbol-fuchsin and the cells at the surfaces were imaged with a Carl-Zeiss ImagerM1 microscope with EXFO fluorescence light and an Axio CamMRc camera. The images were investigated with the software AxioVision and a 10x objective, and the rinsed area was measured with the commercially available software ImageJ (Version 1.48v National Institute of Health, USA). For each status, nine different samples in three different passages were prepared and the rinsed areas were measured. The related micrographs are shown in Fig. 53 and the corresponding graph is shown in Fig. 54.



Titanium



Titanium + PEO

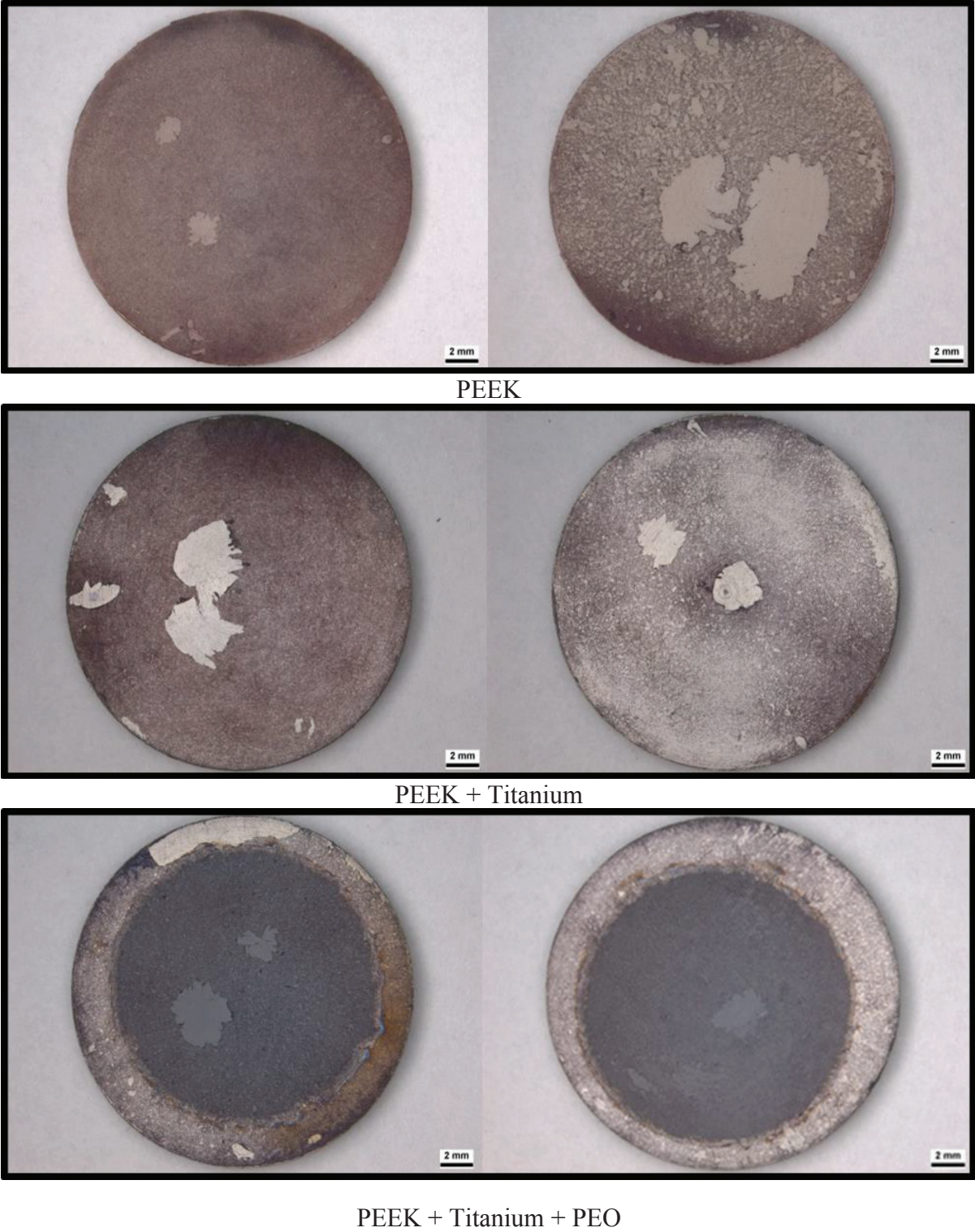


Fig. 53 Rinsed samples of all investigated combinations and the references with the vertical flow assay; brighter spots show the rinsed area of cells: (first row) pure titanium substrate, (second row) titanium substrate with applied PEO-layer, (third row) pure PEEK substrate, (fourth row) PEEK substrate with applied titanium layer, (fifth row) PEEK substrate with applied PEO-layer

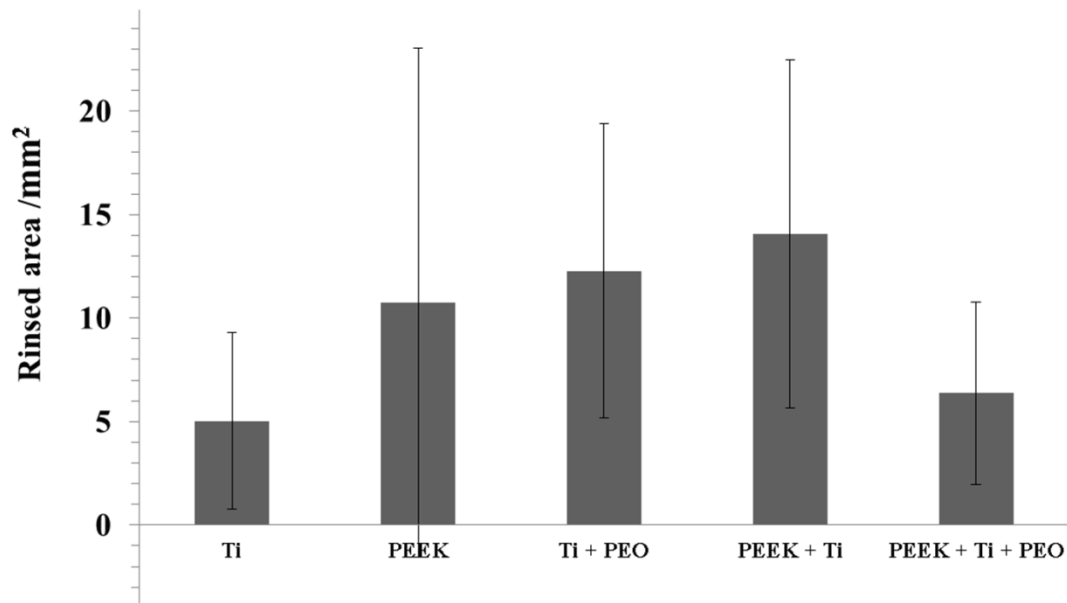


Fig. 54 Rinsed area of the investigated samples during the vertical flow assay for different stages of pure titanium and PEEK

The micrographs of the rinsed surface areas and the investigation into the area sizes show differing results. With a large rinsed area, it can be concluded that the cell adhesion on the surface is decreased, while with a small area the adhesion strength increases. The measured areas within a sample series scatter across a wide range, which leads to a very high error. All errors are not significant for the measured values in a comparison of all samples. This becomes clear in case of the PEEK substrates, where the error ($\pm 12.3 \text{ mm}^2$) becomes higher than the measured value of 10.7 mm^2 . A strong fluctuation around the measured value can be observed, which leads to a very high error. For the PEEK samples, the very high error can be explained with a resulting worse cell adhesion to the PEEK surfaces because of the more or less smooth and plane surface and a lower biocompatibility. In a comparison of PEEK with titanium coating ($14.07 \pm 8.43 \text{ mm}^2$) and pure PEEK, an improvement in cell adhesion with the PEO can be seen because of a more stable value in the rinsed area. In the comparison of the rinsed titanium surfaces ($5.01 \pm 4.26 \text{ mm}^2$) to the titanium samples with a PEO-coating ($12.27 \pm 7.11 \text{ mm}^2$), no improvement with a PEO-coating could be achieved. However, the related error for the titanium samples is also almost as high as the measured value. Furthermore, the cells on the titanium samples in Fig. 53 look somewhat peeled in other positions next to the rinsed areas. This leads to a lower cell adhesion in comparison to the PEO-treated surfaces. The last important area value belongs to the PEO-treated PEEK substrates ($6.37 \pm 4.42 \text{ mm}^2$). These values scatter at every measurement, which leads to a

very high error. In a comparison with the pure PEEK substrate, with its high error rate and high number of rinsed areas, an improvement in cell adhesion using the PEO-coating on PEEK can be concluded.

The PEO-pores in electrolyte E2 300 V reached a size of nearly 2 μm (Tab. 13). Tian et al. [215] observed an increased cell adhesion on micro-structured TiO_2 surfaces with a pore size of approx. 3 μm , which is quite similar to the pores of the examined PEO-surfaces. For a pore diameter under a value of 70 nm, Leoni et al. [219] showed a decreased adhesion because of an affinity of the MG-63 cells, which have a size of 30 μm , to settle at pores with a likewise diameter [220]. In addition, a production of porous structures concludes with an increased hydrophilic character of the surfaces, which leads to an increased adhesion of cell proteins and cells [215,221]. The PEO-surface contains hydroxyl- and oxygen groups, as well as the HA species. At the surfaces, in addition to these chemical bonding possibilities for the cell proteins, the mechanical anchoring of the cell filaments plays an important role in adhesion strength. Cells produce small filopodia to anchor to the pores [220]. Zinger et al. [220] were able to show that a combination of micro- and nano-structuring the titanium surfaces can have a positive effect on cell adhesion. The properties of both chemical bonding and micro-structures are present at the PEO-surfaces and offer optimal conditions for cell adhesion.

Human cells react to surface structures and prefer rough and porous surfaces over the nearly smooth surface of the pure PEEK substrate. This can be shown in the case of a slight improvement in adhesion strength of the titanium-sputtered PEEK substrates and the PEO-treated PEEK surfaces in contrast to the pure PEEK surface. An improvement in the cell adhesion onto polymer substrates can be achieved with a coating of titanium and a subsequent PEO-treatment. Thus, a short conclusion can be drawn for the biocompatibility of PEEK. This can be improved with a titanium coating and a subsequent PEO-coating. In some medicine applications, where an elastic property of the polymer substrates is necessary, the biocompatibility can be improved with a PEO-coating on polymer substrates.

Chapter 5: PEO model

This chapter is based on the investigations published in [222].

4.5 Investigations for the understanding of the PEO process model

A lot of publications are focused on the investigations of the modification, morphology, and chemical composition of PEO-surfaces [5,223–225]. On basis of the investigated PEO-structures and the crystalline layer compositions, the whole oxide layer was examined regarding its internal structure. These results should create a deeper understanding of the layer formation and the influences of the plasma discharges on the oxide layer formation.

4.5.1 Investigations into the oxide layer crystallinity

To investigate the oxide layer structure and the crystallinity throughout the layer one sample with a high content of anatase and rutile was chosen. The sample oxidized in 1.5 M H_2SO_4 and 0.3 M H_3PO_4 at 280 V contains both polymorphs at a ratio of a 64(12)% : R 34(7)% (Fig. 25). A cross-section was taken from the prepared PEO-sample. Before preparation, the sample was embedded in the three-component embedding resin Demotec 10 (Demotec, Nidderau, Germany; 3 parts powder, 2 parts syrup and 1 part liquid). Afterwards, the cross-section was extracted from the epoxy resin and was then embedded again between two pure titanium holders. To achieve a very smooth surface of the cross-section, the whole sample was mechanically grinded and polished. The schematic for the sample preparation is shown in Fig. 55.

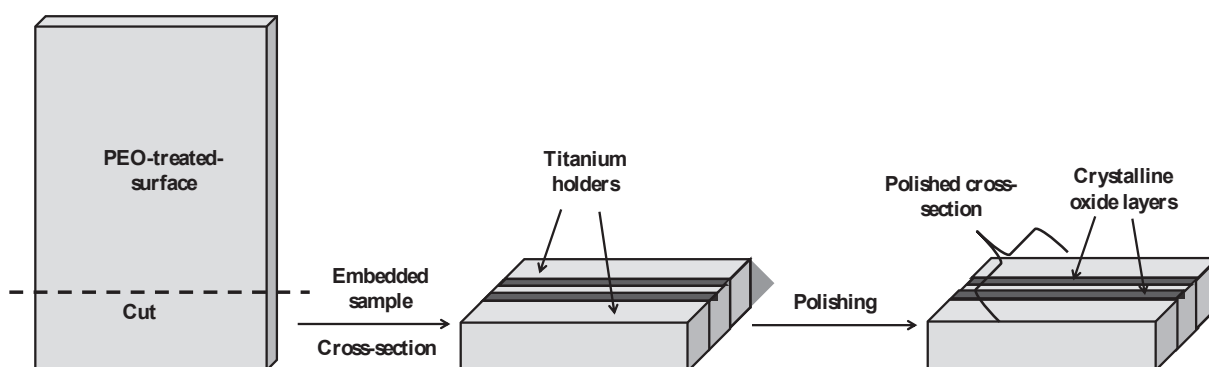


Fig. 55: Mechanically cut and ion-polished cross-section of the PEO-treated titanium sample embedded around two titanium holders, “Reprinted with permission from Applied Surface Science, 443 (2018) 467–474. Copyright 2018 Applied Surface Science.”

Chapter 5: PEO model

For a deeper view into the layer phase composition structure, the cross-section was scanned using the Raman spectroscopy mapping method. The chosen He-Ne-Laser (633 nm) was scanned over the cross-section in 1 μm steps and 11 rows up to 121 scans. Therefore, the laser generated a mapping through the oxide layer from the bottom to the top. In Fig. 56 and Fig. 58, the mapping through the layer and the resulting Raman spectra can be seen. A theoretical Raman spectrum of anatase and rutile is shown in Fig. 57. The spectrum was obtained by measuring the pure powder AEROXIDE® TiO_2 P25 which contains amounts of anatase and rutile phases [226].

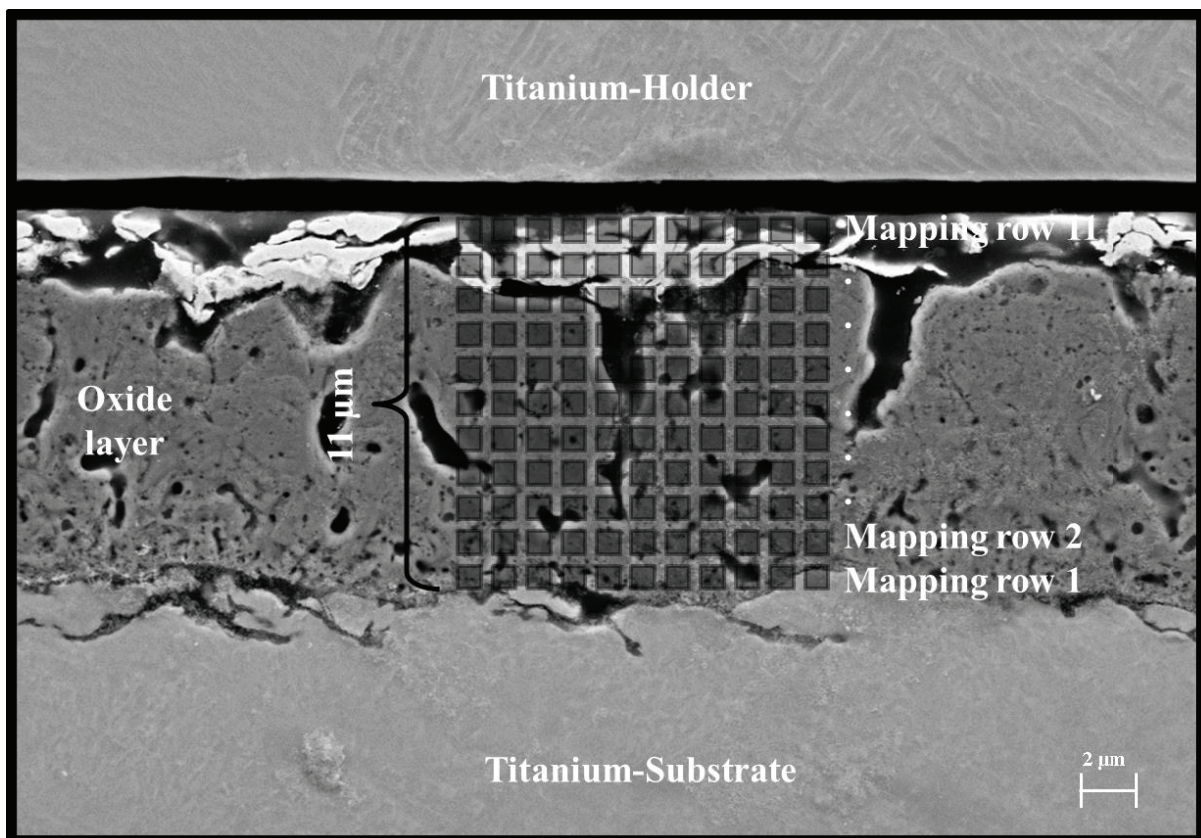


Fig. 56 SEM micrograph of the embedded PEO oxide layer and the Raman scanned area with 11 mapping rows from the bottom to the top of the oxide layer, "Reprinted with permission from Applied Surface Science, 443 (2018) 467–474. Copyright 2018 Applied Surface Science."

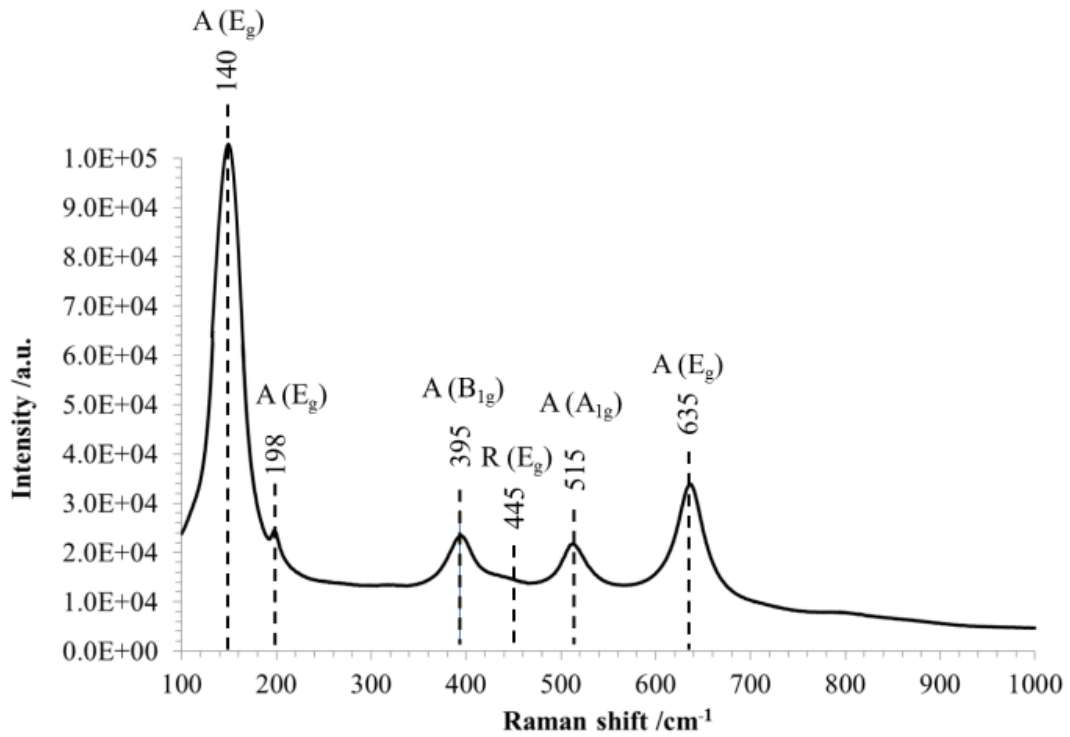


Fig. 57 Theoretical Raman shifts of crystalline anatase (A) and rutile (R); symmetry classes: (E_g) double degenerated (A_{1g}) symmetric and (B_{1g}) antisymmetric

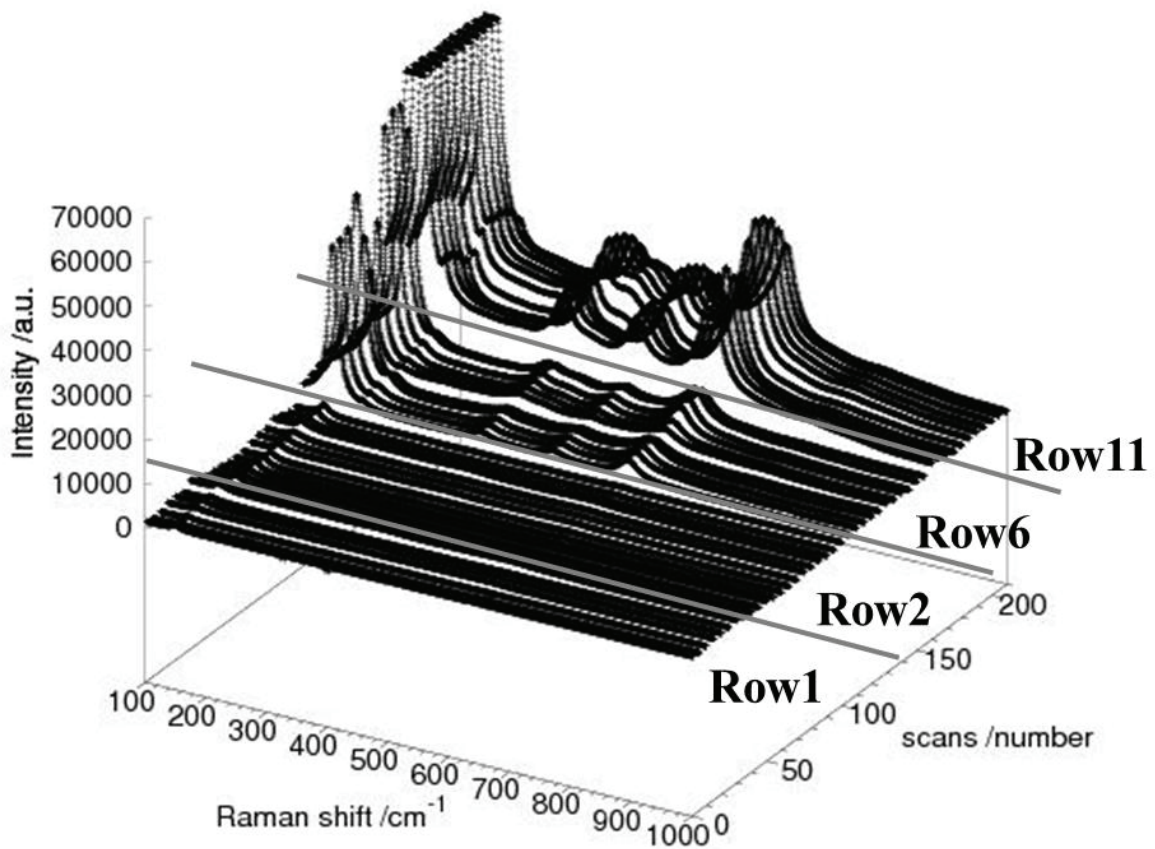


Fig. 58 Raman mapping of the PEO oxide layer from the bottom to the top of the layer with an increase in anatase (140 , 198 , 395 and 635 cm^{-1}) and rutile (445 cm^{-1}) peaks, “Reprinted with permission from Applied Surface Science, 443 (2018) 467–474. Copyright 2018 Applied Surface Science.”

The Raman spectra from row 1 to row 11 in Fig. 58 show a clear increase in intensity for all anatase and rutile peaks. The highest intensity, and thus the highest crystallinity in the surface region can be seen for the mapping row 11, which is the last mapping row on top of the oxide layer. The first mapping row is measured at the bottom of the oxide layer, and the Raman spectra show a very low intensity maxima in these regions. This leads to an amorphous or lower crystalline TiO₂ structure in this region. This assumption of a nanocrystalline or nearly amorphous oxide layer in the lower part can be confirmed by the first Raman mapping row in Fig. 59. For small crystals, the surface effects predominate and the variance of bond lengths is increased, resulting in a diffuse background and broadened peaks. Titanium is a passivating metal, which forms thin amorphous passivation layers while the metal dissolution decreases during the anodization process. The oxide layer of titanium grows from the bottom to the top [59]. This thin amorphous layer grows without any interaction with the micro-discharges, which appear at a later stage during plasma electrolytic oxidation [65]. The PEO-process comprises four different stages, whereby the first stage simulates the growing of the thin anodization oxide layer. In the second stage, the dielectric breakdowns occur, with the resulting micro-discharges at the surface. At stage III and IV, the discharges become more intense [65,76]. With this knowledge it can be seen that the PEO micro-discharges appear during the later stages of the oxidation process and have a longer impact on the already formed layer. This leads to a higher energy input on top of the layer because of the discharges and their high temperatures [47,53].

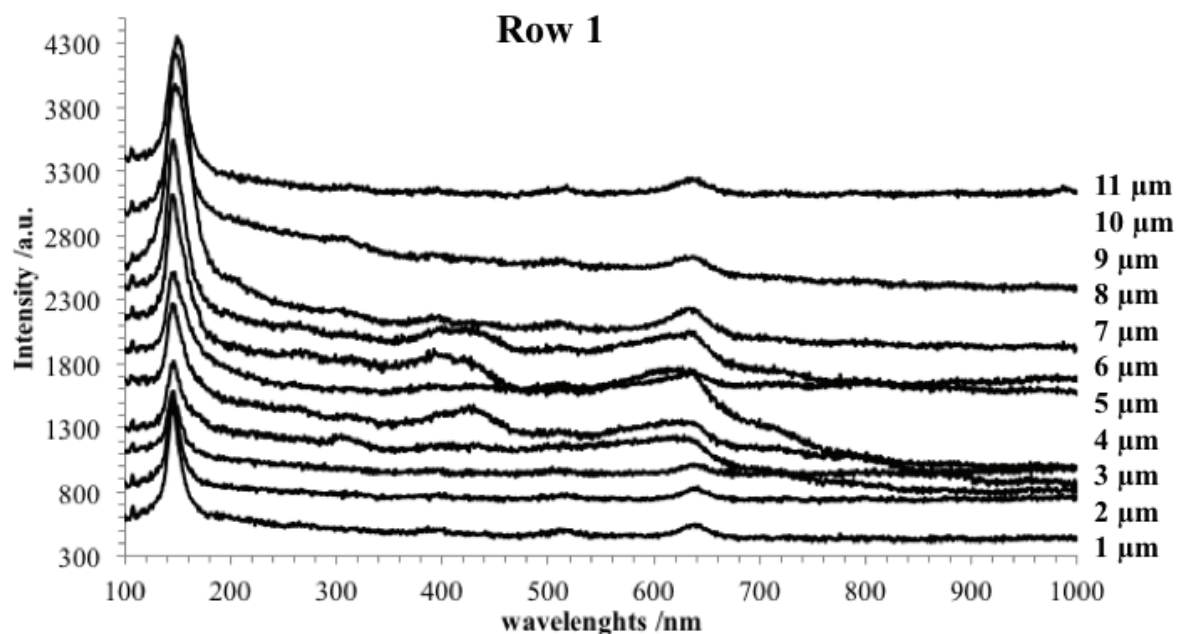


Fig. 59 Raman spectra of the bottom of the amorphous part of the oxide layer

4.5.1.1 PEO layer structure and phase composition

The Raman spectra show the first layer structure of the PEO oxide layer. To look deeper inside the layer, the entire structure and into the phase composition, the EBSD method was chosen. The corresponding software AzTec compares the measured Kikuchi pattern with theoretical ones to identify the crystal phase (α -Ti, Anatase, Brookite, Rutile) and orientation (Indexing). The scan of the layer revealed an increased and predominant distribution of rutile diffraction on top of the layer, showing the corresponding Kikuchi pattern of rutile phases with reasonable intensities fitting to the theoretical pattern. Towards the bottom of the layer, only anatase and brookite diffractions with a poor agreement between measured and theoretical pattern could be detected. The EBSD micrographs with the resulting orientations of the crystallites for all three spatial directions are shown in Fig. 60.

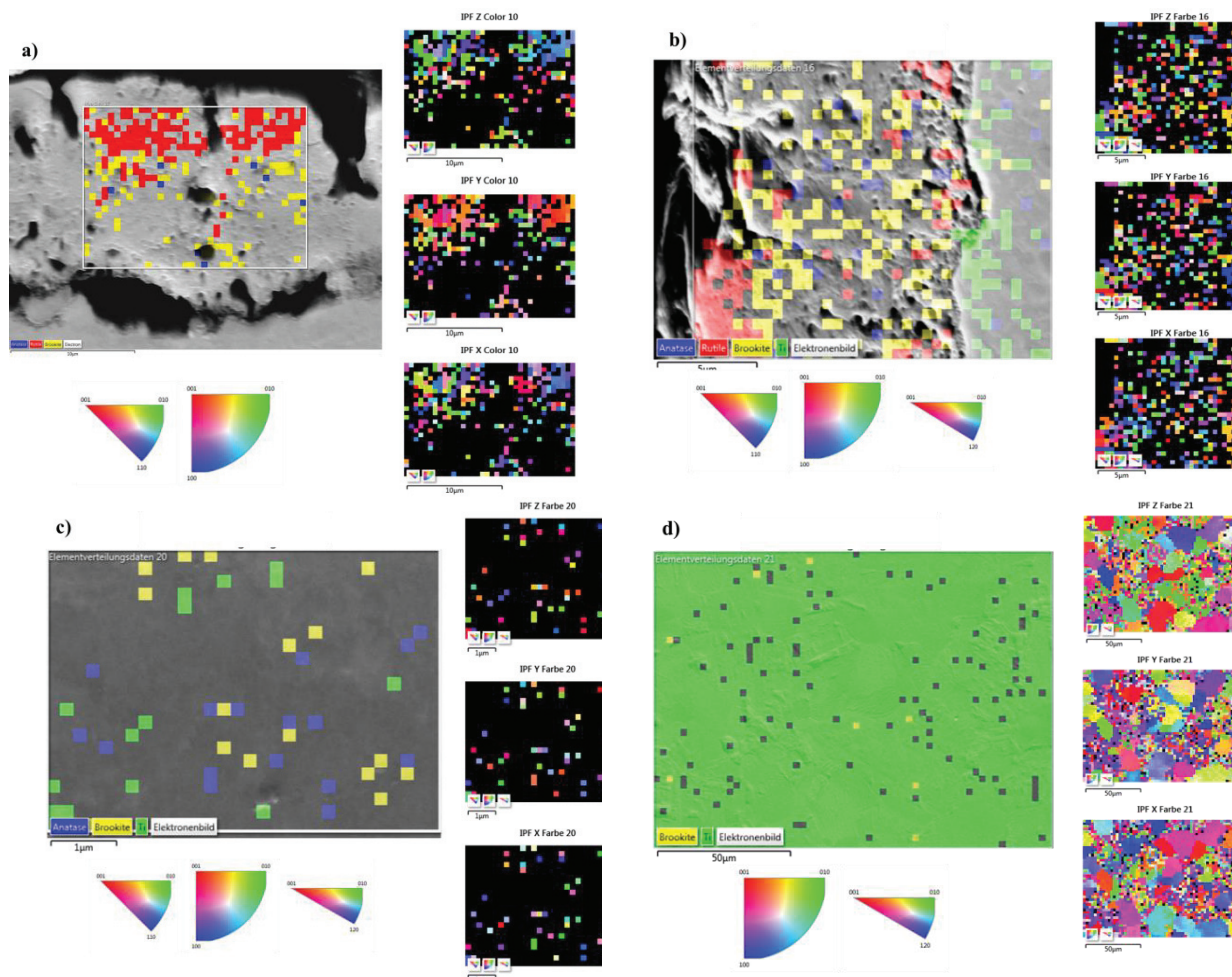


Fig. 60 EBSD micrographs of the PEO oxide layer and the titanium substrate; a) upper oxide layer, b) whole surface area, c) titanium substrate, d) titanium holder

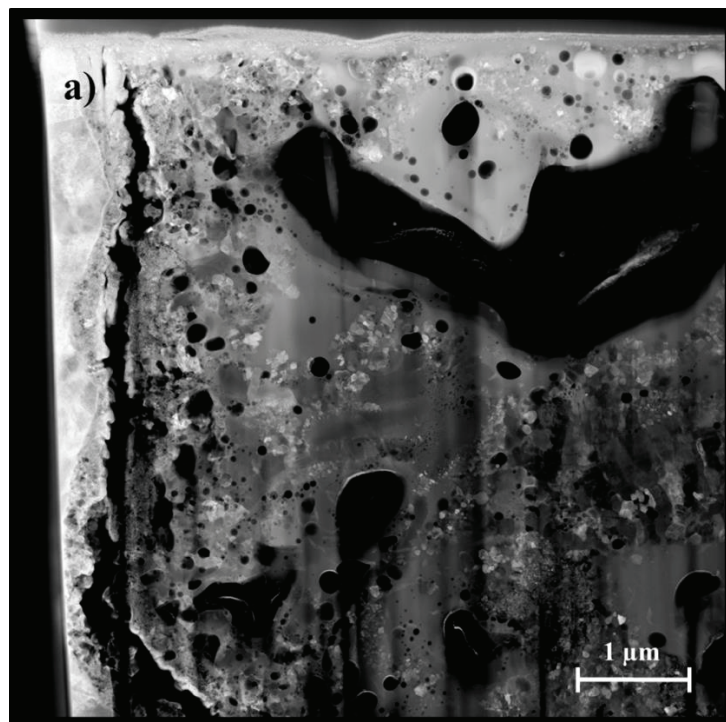
In the lower parts of the oxide layer, the signal strength decreases and only a low number of Kikuchi pattern for anatase or brookite phases showing a low intensity could be detected. This could be an indication of a predominant amorphous part with partially crystalline phases. Towards the boundary layer of the oxide, mainly pore structures occur, which impairs the polymorph band indexing and influences the signal quality. The introduced electrons leave the oxide through the pores, whereupon the scattered background decreases sharply. The brookite diffractions should be carefully interpreted. The brookite structure is unsymmetrical and includes nearly 60 possible reflectors (bands). In this regions of brookite detection there are only 8 bands with a deviation of 1° match to the theoretical pattern. The poor quality of the measured pattern in this region of the oxide layer and the strong deviations from the theoretical brookite pattern make it more likely that actually overlapping rutile and anatase crystallites were measured. In the undefined regions (black), some polymorph bands, as well as partially no polymorph bands, could be detected. These bands cannot be assigned to any of the three oxide crystal structures (Ti^{4+}). This can be a consequence of overlapping crystals or an insufficient ratio of band contrast to scattered background. Here, it is not possible to distinguish between produced bands with a bad contrast (small grain size), an amorphous material or an increased surface roughness (pore structure), whereby the scattered background increases and the band signal is no longer recognizable.

The indexing of the all measured spots is rather low compared to the surrounding titanium holder as seen in Fig. 60 d). This poor indexing could normally be explained by an unsatisfactory pretreatment of the cross-section before the EBSD measurement. To exclude an unsatisfactory pretreatment, the titanium substrate was measured, which should have a comparable surface roughness comparable to the oxide layer. The indexing ratio of the substrate in Fig. 60 c) has the same resolution as the oxide layer. For the titanium substrate, a few crystalline bands could also be detected. Every sample surface underwent the same preparation conditions and the excellent indexing ratio of the titanium holder results in a sufficient preparation for the titanium metal phase. Therefore, the poor indexing of the titanium substrate is not caused by the surface roughness and the band qualities of the corresponding Kikuchi pattern are similar to those of the lower part of the oxide layer. The upper part of the oxide layer shows an adequate indexing and therefore the preparation of this region is at least sufficient for the EBSD measurement.

Overall, the explanation for the poor indexing of the lower part of the oxide layer and the titanium substrate is a small crystallite size of the TiO_2 phases. The average crystallite sizes were analyzed with Rietveld refinement (Diffrac Plus TOPAS, Bruker AXS GmbH, Karlsruhe, Germany) and they are plotted in Fig. 36 as 30 - 40 nm for sample electrolyte E1 at 280 V while titanium also showed a small average crystallite size of 100 nm. The contrast between band and background in the Kikuchi pattern is low and the electron beam spreads across several crystallites. The signal cannot be assigned unambiguously to a titanium dioxide phase. However, the larger average crystallite sizes of the rutile phases of 40 nm offer a better resolution and a higher crystallinity in this area can be concluded.

4.5.1.2 Mechanism and growing process of PEO-layers

Due to the results of the previous Raman- and EBSD measurements, another high-resolution method was chosen to obtain more information about the crystallinity throughout the layer. A part of the cross-section was prepared as a TEM lamella with a thickness of approx. 50 nm, according to [175]. The lamella was scanned via the scanning transmission electron microscopy (STEM), and the corresponding micrograph can be seen in Fig. 61.



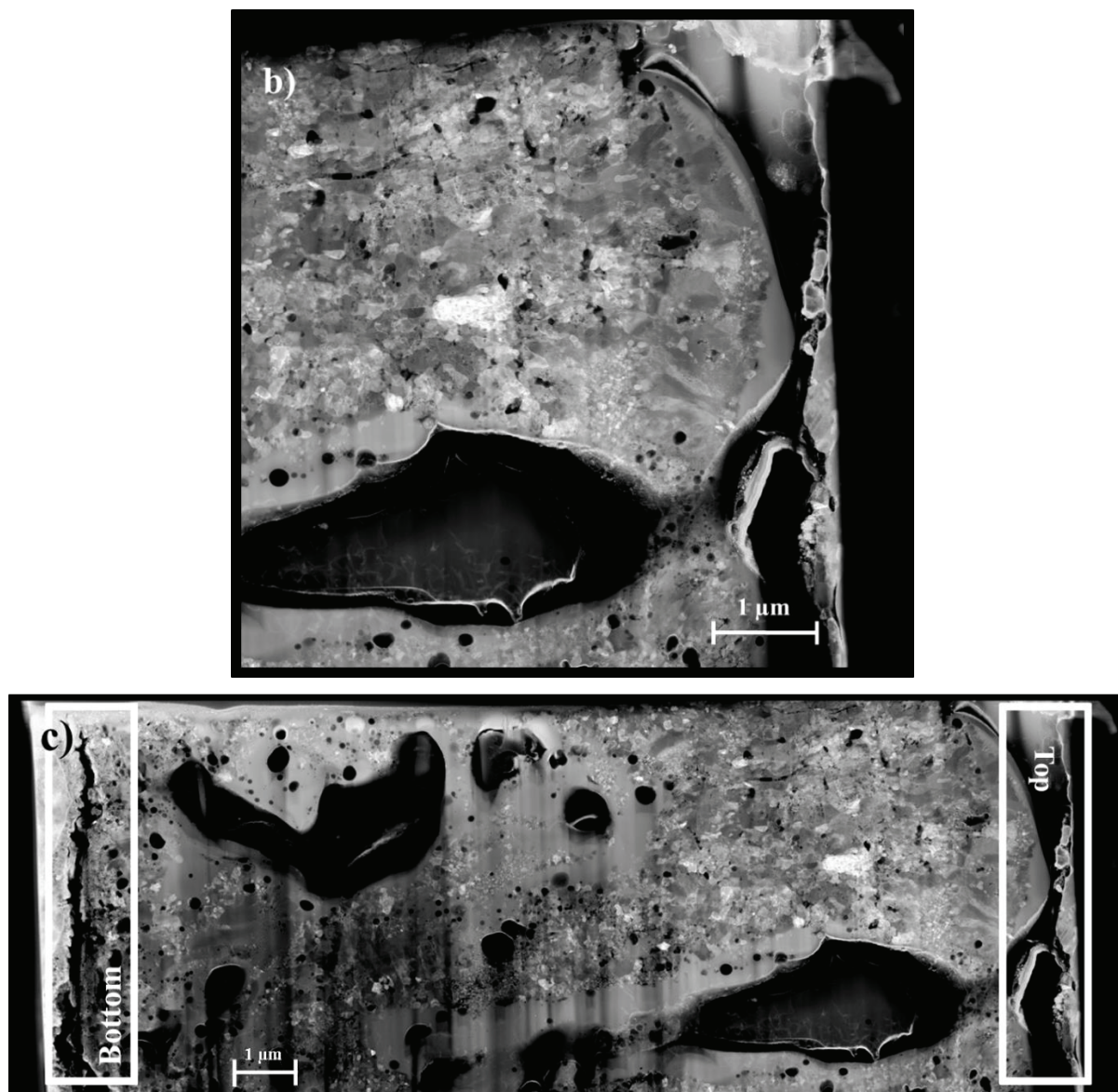


Fig. 61 STEM micrographs of a TEM lamella of the PEO oxide layer with the characteristically pore structures: a) Titanium substrate and the crystalline boundary layer of the oxide layer, b) crystalline upper part of the oxide layer, c) entire PEO-layer, (left) lower part of the oxide layer, (right) upper part of the oxide layer, “Reprinted with permission from Applied Surface Science, 443 (2018) 467–474. Copyright 2018 Applied Surface Science.”

The scanning of the cross-section shows clear crystalline parts throughout the whole oxide layer. The upper part of the PEO-layer at the right side of the micrograph shows areas with quite large crystallites, whereas in the part at the boundary layer on the left side smaller crystals could be identified. The differences in crystallite sizes can also be observed in the Raman spectra in Fig. 58. Therefore, the reduction in the intensity results from the decrease in the average crystallite size. In the middle part of the oxide layer, the formed PEO-pores can be seen. Around these pores, gray regular areas are visible, which may indicate an amorphous TiO_2 phases or one large single crystal around the pores. TEM diffraction pattern around the pores did not show any reflection, which indicates an amorphous phase composition and allows a single crystal to be excluded.

The results of all measurements of the cross-section of the PEO-layer lead to a number of conclusions regarding the layer formation and the resulting structures. In most cases, the crystallinity of the oxide layer depends on the energy input from the micro-discharges [25,28,187–190]. The layer growth starts with the applied voltages, whereby amorphous TiO_2 growth results in a moderate crystalline oxide layer. After the increase in voltage, the plasma breakdowns follow and the characteristic PEO crater-like structure is formed on the surface [30,40,182,183]. In this stage, the titanium dioxide is liquefied and bulges until the TiO_2 crystallizes at these sites and the craters are formed. The molten TiO_2 solidifies due to a high cooling rate at the coating/substrate interface in the cold surrounding electrolyte [83,94]. Following this effect, there is a recrystallization at the TiO_2 surface due to the intensifying micro-discharges. The crystals achieve more time for organization and growing during this process, and larger crystals can be formed in the upper part of the oxide layer. In the lower part of the oxide layer, crystalline parts with smaller particles can be seen. These particles are also achieved through the plasma breakdown fractions. The channels of the PEO-pores can become very deep and can reach the bottom near to the boundary layer to the titanium substrate. In Fig. 62 shows an FIB cut into a PEO-pore that reaches to the bottom of the oxide layer. This sample cut was created with the focused ion beam (FIB) method as described in section 3.2.1.

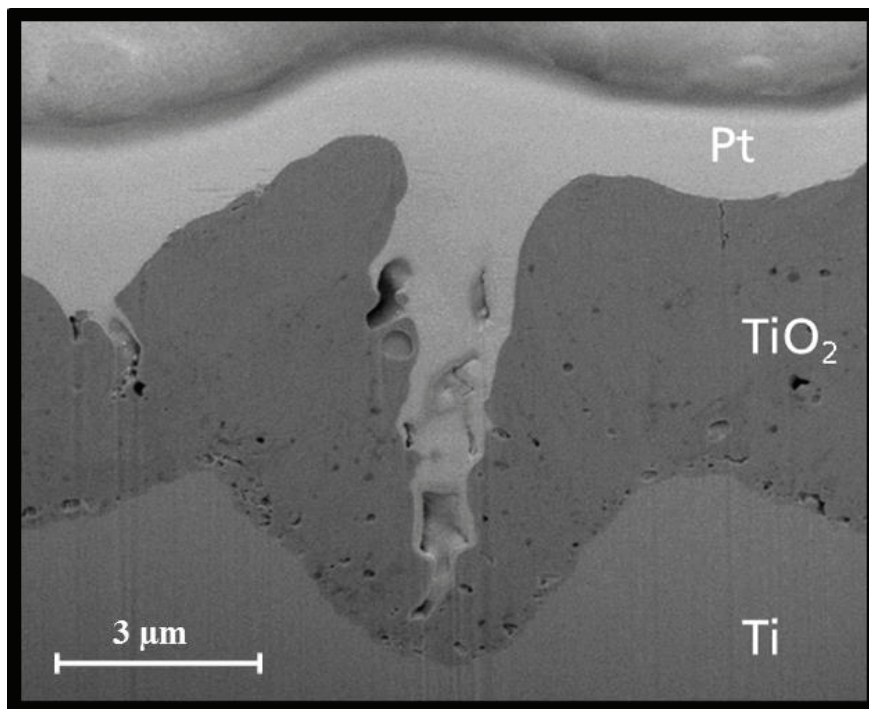


Fig. 62 Characteristic crater-like pore in a FIB-cross-section that reaches to the boundary layer of the substrate, “Reprinted with permission from Applied Surface Science, 443 (2018) 467–474. Copyright 2018 Applied Surface Science.”

The following illustration in Fig. 63 shows the influences of the micro-discharges on the structure of the oxide layer during the PEO-process. Because of the high dielectric strength of the plasma discharges at the bottom of the oxide layer, the energy and heat inputs can act up to the bottom of the oxide layer resulting in small TiO_2 crystallites. This also leads to a partial recrystallization of the titanium particles, which results in a small average crystallite size (titanium 101(11) nm). These parts with small crystallites and the amorphous phases around the pores clearly shows that the titanium dioxide can be converted into the gaseous phase formed by the micro-discharges with a resulting TiO_2 gas cloud. Liu et al. [80] and Hussein et al. [47] reported local discharge temperatures by the discharges of 10^3 to 10^4 K, which is the reason for the liquefying and evaporation of the produced TiO_2 phases. Anatase and rutile have a melting point of about 2130 K and a boiling point of around 3173 K, far below 10^4 K. The formed gas cloud has a reduced thermal conductivity, which leads to a rapid cooling and a reduced crystallization rate of the TiO_2 promoting the formation of an amorphous phase. In addition, the cold electrolyte reduces the crystallization in regions around the produced pores because of a high temperature difference between the molten TiO_2 and cold electrolyte. The oxide cooled down rapidly, and the particles do not receive enough time to order themselves.

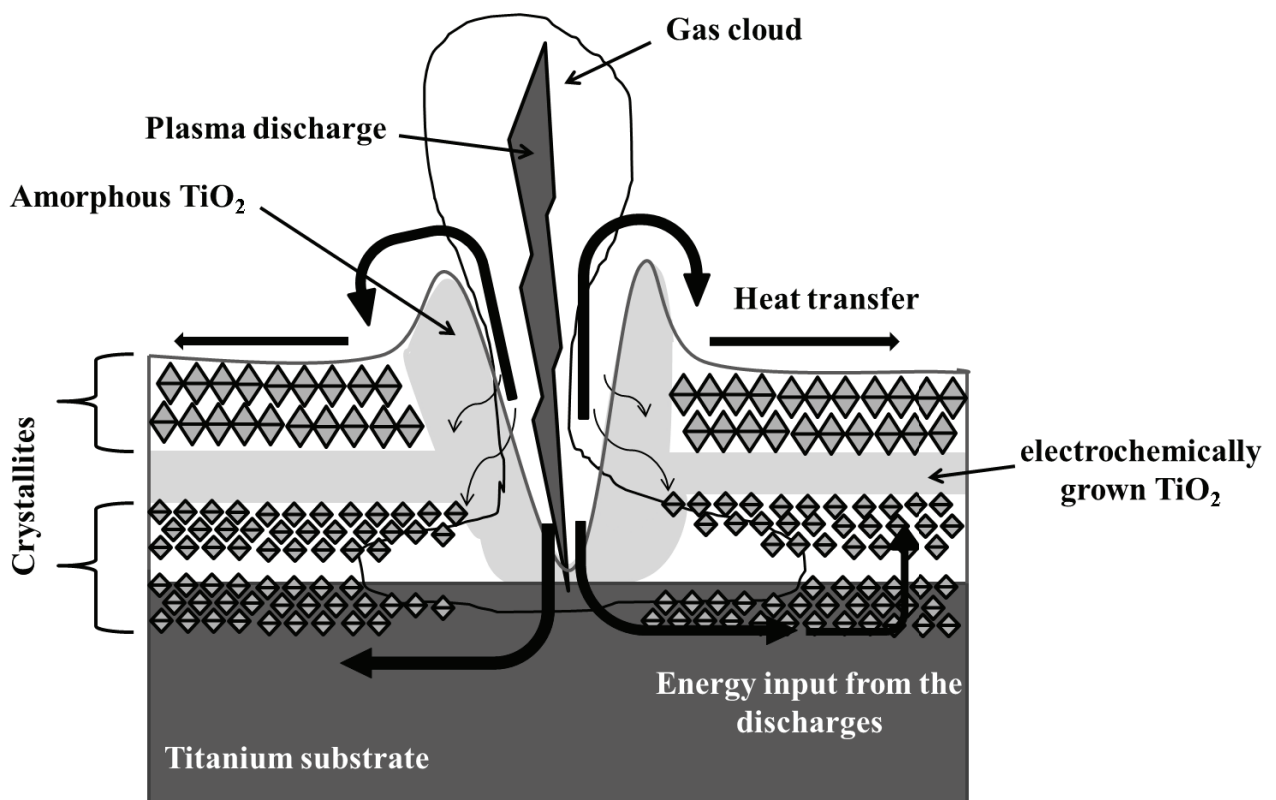


Fig. 63 Model of the discharges during the PEO-process and the influences of the energies on the oxide layer formation, “Reprinted with permission from Applied Surface Science, 443 (2018) 467–474. Copyright 2018 Applied Surface Science.”

The assumption that TiO₂ is also present in the gaseous phase during the appearance of the plasma discharge leads to another used spectroscopic analytical spectroscopic technique. This method measures the spectroscopic information of the produced plasma species of the included atoms. Due to the plasma discharges of the PEO-process, the resulting atoms and gaseous phases can be identified using a spectroscopic detector; the resulting spectra for the two different electrolytes E1 and E2 are shown in Fig. 64.

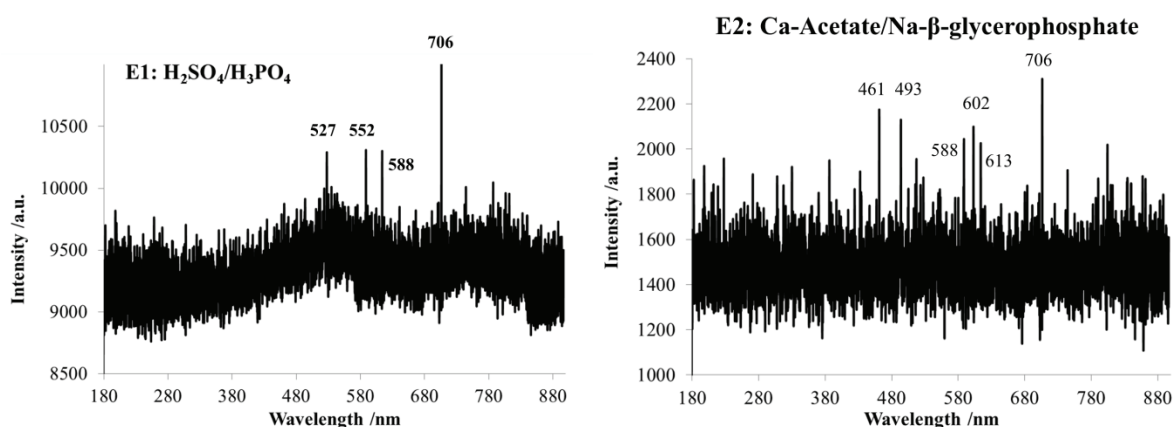


Fig. 64 Detected spectroscopic information of the included atoms on the surface during the PEO-process

Tab. 24 Wavelength of the detected atoms in the LIBS spectra

Element	Titan I	Na I	Ca	TiO				
Wavelength /nm	461	493	527	552	588	602	613	706

The Tab. 24 gives the resulting molecules and elements of the plasma discharges during the PEO-process. Both spectra in Fig. 64 were measured during the plasma discharge phase, when the discharges become very intense. The calcium peaks at 602 nm and 612 nm originate from the electrolyte E2, which contains calcium acetate. The peak at 588 nm is related to the included sodium molecules, which are present in any atmospheric measurement. In both spectra, a lot of peaks of titanium phases are visible, especially the peak at 706 nm, which belongs to the titanium monoxide phase and is visible in both electrolytes. This leads to the conclusion that titanium and titanium oxide pass over into the gaseous phase because of the plasma discharges, which explains the high crystallinity of the oxide layer.

The investigations of the PEO oxide layer gave a more detailed understanding of the structure throughout this layer. The Raman measurements gave an indication of the increasing crystallinity from the bottom of the oxide layer to the top, which was confirmed in the EBSD measurements. The EBSD pattern show a clenched concentration of crystalline rutile phases

Chapter 5: PEO model

at the top of the oxide layer, which decreases to the bottom. The investigation into the small average crystallite sizes of both the anatase and rutile phases resulted in a deeper understanding of the PEO-procedure. The recorded STEM micrographs showed bigger crystallites at the top of the layer, which leads to the supposition that the high temperatures of the acting plasma discharges result in both a liquid and a gaseous TiO_2 phase. Due to the high energy input, large crystallites can be formed at the top of the oxide layer and by the colder electrolyte, and the gaseous phase amorphous TiO_2 is left around the PEO-pores. As with the Raman spectra, it is apparent that small crystallites can be formed at the bottom. This is because of the PEO pore structure and the plasma discharges, which reach to the bottom of the boundary layer of the titanium substrate.

CONCLUSION

5. CONCLUSION

The modification of parameters of plasma electrolytic oxidation for a classification of titanium dioxide layer properties (structure, crystallinity, photocatalytic activity and biocompatibility) as well as a subsequent expansion of the oxide layer formation were carried out in the present work. The layers were prepared in various electrolytic systems and were examined for their structure and crystallinity without further treatment. The different electrolytic systems had a strong influence on the structure and crystallinity of the surfaces, which were analyzed using SEM and XRD. It could be shown that higher electrolyte conductivity increased the pore size and oxide layer thicknesses as well as strongly influenced the proportions of the crystalline phases anatase and rutile inside the oxide layer. The different conductivities of alkaline electrolytic systems impacted on the breakdown voltages due to an increased gas formation at the anode surface and a consequently reduced surface area. These phenomena affected the layer thicknesses, which were lowered in comparison to the acidic electrolytes. Significant differences in the oxide surface structures were observed between phosphate-containing (PO_4^{3-}) solutions, which produced round pore structures, and solutions with hydroxide anions (OH^-), which produced linear pore structures. Electrolytic systems with sulfuric acid (H_2SO_4) produced a novel stacked structure, which resulted in an increased surface area due to more distributed small pores inside the layer structure. The process of plasma electrolytic oxidation allows the properties of TiO_2 surfaces to be adjusted in any direction, such as with regard to pore size and layer thickness as well as the adjustment of the ratio of the crystalline components anatase and rutile.

Inside the oxide layer of all PEO-samples, high crystalline fractions of anatase and rutile were detected using x-ray diffraction, which increased markedly with an increase in the conductivity or the oxidizing capacity of the electrolyte and the applied voltage. Very high levels of crystalline rutile phases can be seen with a treatment in highly conductive H_2SO_4 containing electrolytes. Compared to the strongly photocatalytic active reference material P25, a ratio of anatase to rutile of almost 3 : 1 could be established on some PEO-surfaces. PEO-films with a predominantly crystalline anatase content and a high layer thickness, as well as layers with a high rutile content of 2 : 1 or 1 : 2 and a lower layer thickness showed the highest photocatalytic activity. In these cases, the contained rutile phases provided an increase in photocatalytic activity. Similarly, the determination of a direct band gap of the PEO-layers suggested an increased efficiency of the photocatalytic activity in a comparison with conventionally used layers and coatings.

CONCLUSION

The investigations into the modification of titanium dioxide surfaces, showed the possibility of adjusting porosity and layer thickness, such as the crystallinity of PEO-layers. PEO-coatings can help to strengthen the cell adhesion and the durability of implants in the human body, due to a better attachment of cell proteins and filaments at the characteristic PEO pore structure. The adjustment of different pore sizes using the plasma electrolytic oxidation can help to create ideal conditions for different cell types. Cells prefer to attach to structures similarly to their own size, because of an optimal anchoring to the structure. This adjustment can be provided by the PEO-process.

The results of the oxide layer structure demonstrate an ability to further develop the theoretical PEO-layer growth and to forecast the influences of the plasma discharges on the PEO-structure. Producing of highly crystalline oxide layers makes the process of plasma evolution and its actions clearer. The high energies of the plasma discharges form high crystalline parts at the top of the oxide layer. Further crystalline regions can be recognized at the bottom of the oxide layer and in the titanium substrate by the pore structures extending to the substrate. The high energy input of the plasma discharges thus affects the bottom of the oxide layer and also forms crystallites in these regions of the titanium substrate. The high temperatures of the plasma discharges result in a melting and evaporating of the TiO_2 , and the gaseous phases cool down rapidly around the pore structures. This results in amorphous TiO_2 phases around the pore structures, contrary to the expected high crystallinity due to the plasma influence.

Through the development of the crystalline TiO_2 surfaces, it was possible to detect the photocatalytic activity of these structures and predict a high efficiency of such surfaces in the catalytic domain. The formation of the highly structured TiO_2 surfaces also allows a transfer to polymeric substrates. The detection of an improvement in biocompatibility and suitability as an implant material compared to pure polymer substrates could be proven. The production of the different surface structures and compositions show a not yet fully exploited potential of these structures to further optimize the possibilities of applications, and especially regarding the photocatalytic activity of PEO-coatings.

6. OUTLOOK

The successful adjustment of special PEO TiO₂ surface properties, such as a high crystallinity of the TiO₂ phases and noticeable photocatalytic behavior, as well as the slight improvement of biocompatibility of polymeric substrates, by applying of PEO-coatings has been demonstrated in this work. In different electrolytic systems, it is possible to produce various structures and oxide layer thicknesses. It could also be detected an effect of the electrolyte components on the breakdown voltages. However, for a better understanding other influencing factors, in a simple alkaline or acidic electrolyte, on the breakdown voltage and structure of the PEO-layers, should be investigated. The generation of defined anatase and rutile amounts in the oxide layers with the electrolytes containing H₂SO₄ (E1, E3) and NaOH/Na-tartrate (E5) seems to be most efficient, and this method could lead to a controlled crystallinity [93]. These results opened the way for the complex possibility of creating highly crystalline and porous TiO₂ structures. For this purpose, further studies on the influence of the electrolyte and its composition on the formation of the crystalline phases should be done. For PEO-structures, other electrolytic systems with a different composition and conductivity will be also interesting for new TiO₂ phase compositions. The produced PEO-layers in this study showed a preferred orientation of the crystalline oxide phases and the titanium substrate. This effect could be further examined relating to the used titanium substrate and its main crystal growth direction. Investigations could be determined on polished or molded samples where these factors can be neglected.

Another important investigation could focus on the surface structure as well as the pore sizes and shapes. The increased pore size or number, such as through a changed shape, could have an influence on the surface area, which can be increased with more pores inside the surface structure. All produced PEO-structures showed a photocatalytic activity for all used electrolytic systems [196]. The surface area, such as the composition of crystalline phases and the crystallite sizes, can have an influence on the photocatalytic activity of PEO-surfaces. One of the most important parameters for photocatalytic activity is the layer thickness, which also increases the specific surface area. The layer thicknesses, in combination with the composition of the crystalline phases, should be examined in greater detail for an example electrolytic system. For this purpose, several samples should be analyzed in a selected electrolyte with different layer thicknesses and crystallinities in order to determine the influence of these parameters on the photocatalytic activity. All parameters should be investigated separately to clarify the influence on the photocatalytic properties more clearly.

OUTLOOK

Furthermore, it might be interesting to investigate the mechanism of photocatalysis on PEO-layers compared to powder samples or TiO₂ composites, which can make the effectiveness of the layers obvious. Similarly, a more useful system for investigating photocatalytic activity should be used. For this, some preliminary experiments could be performed with citric acid and oxalic acid based on some literature data [227–230] as an alternative to the used dyes.

With the application of a PEO-coating to polymeric substrates, a slight improvement in cell adhesion could be shown. For further investigations, an additional development of the used vertical-flow-assay should be done. The different pore sizes of the PEO-layers could also have an influence on the cell adhesion, for which a systematic examination of small and large pores in connection with the cell size should be considered. Some preliminary experiments were carried out with the help of a selected electrolyte [218]. Likewise, an additional use of PEO-layers in medicine and biology of absorption capacities and storing functions could be conceivable.

The extensive investigations on the structure of PEO-layers using TEM and EBSD methods provided a broader understanding of the formation PEO oxide layers. However, subsequent investigations into the influence of the plasma discharges and their species on the PEO-layers and their crystalline constituents should be made. Thermal imaging cameras could record the nature and temperature outputs to the oxide layers of the discharges during the process, which could make temperature gradients during layer growth visible.

For a far-reaching investigation, a Pair Distribution Function (PDF) calculation of the PEO-layers is conceivable. With this calculation, the individual titanium dioxide particles within the oxide layers can be simulated and a spatial packing of the TiO₂ phases can be decrypted. A detailed investigation into the TiO₂ layers and the whole structure would lead to the creation of a further model of the PEO-process and the impact of the plasma discharge, which would create a better understanding of the PEO coatings.

7. BIBLIOGRAPHY

- [1] S. Abbasi, F. Golestani-Fard, S.M.M. Mirhosseini, A. Ziaee, M. Mehrjoo, Effect of electrolyte concentration on microstructure and properties of micro arc oxidized hydroxyapatite/titania nanostructured composite, *Mater. Sci. Eng. C.* 33 (2013) 2555–2561. doi:10.1016/j.msec.2013.02.018.
- [2] Y. Huang, Y. Wang, C. Ning, K. Nan, Y. Han, Hydroxyapatite coatings produced on commercially pure titanium by micro-arc oxidation., *Biomed. Mater.* 2 (2007) 196–201. doi:10.1088/1748-6041/2/3/005.
- [3] D. Quintero, O. Galvis, J.A. Calderón, J.G. Castaño, F. Echeverría, Effect of electrochemical parameters on the formation of anodic films on commercially pure titanium by plasma electrolytic oxidation, *Surf. Coatings Technol.* 258 (2014) 1223–1231. doi:10.1016/j.surfcoat.2014.06.058.
- [4] T. Akatsu, Y. Yamada, Y. Hoshikawa, T. Onoki, Y. Shinoda, F. Wakai, Multifunctional porous titanium oxide coating with apatite forming ability and photocatalytic activity on a titanium substrate formed by plasma electrolytic oxidation, *Mater. Sci. Eng. C.* 33 (2013) 4871–4875. doi:10.1016/j.msec.2013.08.003.
- [5] S. Uttiya, D. Contarino, S. Prandi, M. Carnasciali, G. Gemme, L. Mattera, R. Rolandi, Anodic Oxidation of Titanium in Sulphuric Acid and Phosphoric Acid Electrolytes, *J. Mater.* 1 (2009) 2. doi:10.15744/2348-9812.1.S106.
- [6] H.J. Oh, J.H. Lee, Y. Jeong, Y.J. Kim, C.S. Chi, Microstructural characterization of biomedical titanium oxide film fabricated by electrochemical method, *Surf. Coatings Technol.* 198 (2005) 247–252. doi:10.1016/j.surfcoat.2004.10.029.
- [7] Y. Mizukoshi, N. Masahashi, Fabrication of a TiO₂ photocatalyst by anodic oxidation of Ti in an acetic acid electrolyte, *Surf. Coatings Technol.* 240 (2014) 226–232. doi:10.1016/j.surfcoat.2013.12.030.
- [8] M.A. Fox, Photocatalytic Oxidation of Organic Substrates, in: *Proc. NATO ASI Int. Conf. Photocatal. Environ. Trends Appl.*, In: Schiavello M (ed.), Palermo, Kluwer, Dodrecht, 1988: pp. 445–467.
- [9] J.M. Macak, M. Zlamal, J. Krysa, Self-Organized TiO₂ Nanotube Layers as Highly Efficient Photocatalysts, 6 (2007) 300–304. doi:10.1002/sml.200600426.
- [10] E.M. Saggiaro, A.S. Oliveira, T. Pavesi, C.G. Maia, L. Filipe, V. Ferreira, J.C. Moreira, Use of Titanium Dioxide Photocatalysis on the Remediation of Model Textile Wastewaters Containing Azo Dyes, (2011) 10370–10386. doi:10.3390/molecules161210370.
- [11] M. Gratzel, *Energy Resources through Photochemistry and Catalysis*, Academic Press, New York, 1983.
- [12] N. Serpone, Ezio Pelizzetti, *Photocatalysis*, Wiley, New York, 1989.
- [13] O.K. Varghese, M. Paulose, K. Shankar, G.K. Mor, C.A. Grimes, Water-photolysis properties of micron-length highly-ordered titania nanotube-arrays, *J. Nanosci. Nanotechnol.* 5 (2005) 1158.

BIBLIOGRAPHY

- [14] N.K. Allam, C.A. Grimes, Photoelectrochemical and water photoelectrolysis properties of ordered TiO₂ nanotubes fabricated by Ti anodization in fluoride-free HCl electrolytes, (2008). doi:10.1039/b718580d.
- [15] A. Fujishima, K. Hashimoto, T. Watanabe, TiO₂ photocatalysis: fundamentals and applications, Tokyo Bkc, Tokyo, 1999.
- [16] D.G. Fu, Y. Zhang, X. Wang, J.Z. Liu, Z.H. Lu, Surface Second Order Optical Nonlinearity of Titanium Dioxide Sized in Nanometer Range, *Chem. Lett.* (2001) 328–329.
- [17] A.H. Abdullah, U.I. Gaya, Heterogeneous photocatalytic degradation of organic contaminants over titanium dioxide: A review of fundamentals, progress and problems, *J. Photochem. Photobiol., C Photochem. Rev.* 9 (2008) 1–12.
- [18] C.B. Mendive, T. Bredow, A. Feldhoff, M. Blesa, D. Bahnemann, Adsorption of oxalate on anatase (100) and rutile (110) surfaces in aqueous systems: experimental results vs. theoretical predictions, *Phys. Chem. Chem. Phys.* 11 (2009) 1794–1808. doi:10.1039/b814608j.
- [19] M. Kaneko, I. Okura, *Photocatalysis: Science and Technology*, Springer, Berlin, 2002.
- [20] M.R. Hoffmann, S.T. Martin, W. Choi, D.W. Bahnemann, Environmental Applications of Semiconductor Photocatalysis, *Chem. Rev.* 95 (1995) 69–96.
- [21] A.Y. Ahmed, T. Kandiel, T. Oekermann, D. Bahnemann, Photocatalytic Activities of Different Well-defined Single Crystal, *J. Phys. Chem. Lett.* 2 (2011) 2461–2465. doi:10.1021/jz201156b.
- [22] W. Kim, T. Tachikawa, G.H. Moon, T. Majima, W. Choi, Molecular-level understanding of the photocatalytic activity difference between anatase and rutile nanoparticles, *Angew. Chemie - Int. Ed.* 53 (2014) 14036–14041. doi:10.1002/anie.201406625.
- [23] M.L. Kääriäinen, T.O. Kääriäinen, D.C. Cameron, Titanium dioxide thin films, their structure and its effect on their photoactivity and photocatalytic properties, *Thin Solid Films.* 517 (2009) 6666–6670. doi:10.1016/j.tsf.2009.05.001.
- [24] S.K. Poznyak, D. V. Talapin, A.I. Kulak, Electrochemical oxidation of titanium by pulsed discharge in electrolyte, *J. Electroanal. Chem.* 579 (2005) 299–310. doi:10.1016/j.jelechem.2005.03.002.
- [25] M.R. Bayati, F. Golestani-Fard, A.Z. Moshfegh, The effect of growth parameters on photo-catalytic performance of the MAO-synthesized TiO₂ nano-porous layers, *Mater. Chem. Phys.* 120 (2010) 582–589. doi:10.1016/j.matchemphys.2009.12.005.
- [26] M.R. Bayati, F. Golestani-Fard, A.Z. Moshfegh, How photocatalytic activity of the MAO-grown TiO₂ nano/micro-porous films is influenced by growth parameters?, *Appl. Surf. Sci.* 256 (2010) 4253–4259. doi:10.1016/j.apsusc.2010.02.011.
- [27] L.K. Mirelman, J.A. Curran, T.W. Clyne, The production of anatase-rich photoactive coatings by plasma electrolytic oxidation, *Surf. Coatings Technol.* 207 (2012) 66–71. doi:10.1016/j.surfcoat.2012.05.076.
- [28] Y. Mizukoshi, N. Masahashi, Photocatalytic Activities and Crystal Structures of

BIBLIOGRAPHY

- Titanium Dioxide by Anodization: Their Dependence upon Current Density, *Mater. Trans.* 51 (2010) 1443–1448. doi:10.2320/matertrans.M2010106.
- [29] X. Liu, P.K. Chu, C. Ding, Surface modification of titanium, titanium alloys, and related materials for biomedical applications, *Mater. Sci. Eng. R Reports.* 47 (2004) 49–121. doi:10.1016/j.mser.2004.11.001.
- [30] M. Schmidt, J.; Schrader, C.; Tzschach, Die plasmachemische Oxidation von Leichtmetallen für optische und medizinische Anwendungen, *Galvanotechnik.* (2012) 2416–2427.
- [31] R.C. Chang, F.Y. Chen, C.T. Chuang, Y.C. Tung, Residual stresses of sputtering titanium thin films at various substrate temperatures., *J. Nanosci. Nanotechnol.* 10 (2010) 4562–4567. doi:10.1166/jnn.2010.1696.
- [32] D.M. Devine, J. Hahn, R.G. Richards, H. Gruner, R. Wieling, S.G. Pearce, Coating of carbon fiber-reinforced polyetheretherketone implants with titanium to improve bone apposition, *J. Biomed. Mater. Res. - Part B Appl. Biomater.* 101 (2013) 591–598. doi:10.1002/jbm.b.32861.
- [33] C.-M. Han, E.-J. Lee, H.-E. Kim, Y.-H. Koh, K.N. Kim, Y. Ha, S.-U. Kuh, The electron beam deposition of titanium on polyetheretherketone (PEEK) and the resulting enhanced biological properties., *Biomaterials.* 31 (2010) 3465–70. doi:10.1016/j.biomaterials.2009.12.030.
- [34] S.D. Cook, M. Rust-Dawicki, Preliminary evaluation of titanium-coated PEEK dental implants, *J. Oral Implantol.* 21 (1995) 176–81. doi:10.1109/SBEC.1995.514436.
- [35] M. Martin, N. Eckardt, A. Henning, A. Weißbach, F. Hollstein R. Ohser-Wiedemann, M. Martin, N. Eckardt, A. Henning, A. Weißbach, F. Hollstein R. Ohser-Wiedemann, *Galvanotechnik.* 5 (2004) 1128–1133.
- [36] X. Wu, X. Liu, J. Wei, J. Ma, F. Deng, S. Wei, Nano-TiO₂/PEEK bioactive composite as a bone substitute material: In vitro and in vivo studies, *Int. J. Nanomedicine.* 7 (2012) 1215–1225. doi:10.2147/IJN.S28101.
- [37] H.K. Tsou, P.Y. Hsieh, M.H. Chi, C.J. Chung, J.L. He, Improved osteoblast compatibility of medical-grade polyetheretherketone using arc ionplated rutile/anatase titanium dioxide films for spinal implants, *J. Biomed. Mater. Res. - Part A.* 100 A (2012) 2787–2792. doi:10.1002/jbm.a.34215.
- [38] H.K. Tsou, P.Y. Hsieh, C.J. Chung, C.H. Tang, T.W. Shyr, J.L. He, Low-temperature deposition of anatase TiO₂ on medical grade polyetheretherketone to assist osseous integration, *Surf. Coatings Technol.* 204 (2009) 1121–1125. doi:10.1016/j.surfcoat.2009.06.018.
- [39] J. Yahalom, J. Zahavi, Experimental evaluation of some electrolytic breakdown hypotheses, *Pergamon Press.* 16 (1971) 603–607.
- [40] J. Yahalom, J. Zahavi, Electrolytic breakdown crystallization of anodic oxide films on Al, Ta and Ti, *Ektrochimia Acta.* 15 (1970) 1429–1435.
- [41] R.S. Alwitt, A.K. Vijh, Sparking Voltages Observed on Anodization of Some Valve Metals, *J. Electrochem. Soc.* 116 (1969) 388–390.

BIBLIOGRAPHY

- [42] T. Mi, B. Jiang, Z. Liu, L. Fan, Plasma formation mechanism of microarc oxidation, *Electrochim. Acta.* 123 (2014) 369–377. doi:10.1016/j.electacta.2014.01.047.
- [43] A. Hickling, M.D. Ingram, Glow-discharge electrolysis, *J. Electroanal. Chem.* 8 (1964) 65–81.
- [44] S. Ikonopisov, Theory of electrical breakdown during formation of barrier anodic films, *Electrochim. Acta.* 22 (1977) 1077–1082. doi:10.1016/0013-4686(77)80042-X.
- [45] S. Ikonopisov, A. Girginov, M. Machkova, Post-breakdown anodization of aluminium, *Electrochim. Acta.* 22 (1977) 1283–1286.
- [46] L. Wang, L. Chen, Z. Yan, H. Wang, J. Peng, Effect of potassium fluoride on structure and corrosion resistance of plasma electrolytic oxidation films formed on AZ31 magnesium alloy, *J. Alloy. Compd.* 480 (2009) 469–474. doi:10.1016/j.jallcom.2009.01.102.
- [47] R.O. Hussein, X. Nie, D.O. Northwood, A. Yerokhin, A. Matthews, Spectroscopic study of electrolytic plasma and discharging behaviour during the plasma electrolytic oxidation (PEO) process, *J. Phys. D: Appl. Phys.* 43 (2010) 105203. doi:10.1088/0022-3727/43/10/105203.
- [48] F. Me, Diagnostics of an electrolytic microarc process for aluminium alloy oxidation, *J. Electroanal. Chem.* 200 (2005) 804–808. doi:10.1016/j.surfcoat.2005.01.076.
- [49] A. Nominé, S.C. Troughton, A.V. Nominé, G. Henrion, T.W. Clyne, High speed video evidence for localised discharge cascades during plasma electrolytic oxidation, *Surf. Coatings Technol.* 269 (2015) 125–130. doi:10.1016/j.surfcoat.2015.01.043.
- [50] C.S. Dunleavy, J.A. Curran, T.W. Clyne, Self-similar scaling of discharge events through PEO coatings on aluminium, *Surf. Coatings Technol.* 206 (2011) 1051–1061. doi:10.1016/j.surfcoat.2011.07.065.
- [51] L. Wang, L. Chen, Z. Yan, W. Fu, Optical emission spectroscopy studies of discharge mechanism and plasma characteristics during plasma electrolytic oxidation of magnesium in different electrolytes, *Surf. Coat. Technol.* 205 (2010) 1651–1658. doi:10.1016/j.surfcoat.2010.10.022.
- [52] A.L. Yerokhin, A. Leyland, A. Matthews, Kinetic aspects of aluminium titanate layer formation on titanium alloys by plasma electrolytic oxidation, *Appl. Surf. Sci.* 200 (2002) 172–184. doi:10.1016/S0169-4332(02)00848-6.
- [53] A.L. Yerokhin, X. Nie, A. Leyland, A. Matthews, S.J. Dowey, Plasma electrolysis for surface engineering, *Surf. Coatings Technol.* 122 (1999) 73–93. doi:10.1016/S0257-8972(99)00441-7.
- [54] S.-W. Ha, E. Wintermantel, *Biokompatible Metalle, Medizintechnik - Life Sci. Eng.* (2009) 191–217. doi:10.1007/978-3-540-93936-8.
- [55] P. Tengvall, M. Textor, P. Thomsen, D.M. Brunette, *Titanium in Medicine.* Berlin, Springer Verlag, 2001.
- [56] J.H. Kerspe, *Aufgaben und Verfahren in der Oberflächenbehandlung: neuere Entwicklungen in der Oberflächentechnik,* expert Verlag, 2000.
- [57] K. Bobzin, *Oberflächentechnik für den Maschinenbau,* Wiley-VCH Verlag, Aachen,

BIBLIOGRAPHY

- 2013.
- [58] P. Schmuki, M.J. Graham, Corrosion, Encyclopedia of Chemical Physics and Physical Chemistry, Volume III: Applications, Institute of Physics Publishing, Bristol and Philadelphia, 2001.
- [59] P. Schmuki, From Bacon to barriers: a review on the passivity of metals and alloys, *J. Solid State Electrochem.* (2002) 145–164.
- [60] H. Masuda, K. Fukuda, Ordered metal nanohole arrays made by a two-step replication of honeycomb structures of anodic alumina, *Science* (80-.). 268 (1995) 1466–1468.
- [61] J.M. Macak, H. Hildebrand, U. Marten-Jahns, P. Schmuki, Mechanistic aspects and growth of large diameter self-organized TiO₂ nanotubes, *J. Electroanal. Chem.* 621 (2008) 254–266. doi:10.1016/j.jelechem.2008.01.005.
- [62] M.J.Q. Yong, A.S.W. Wong, G.W. Ho, Mesophase ordering and macroscopic morphology structuring of mesoporous TiO₂ film, *Mater. Chem. Phys.* 116 (2009) 563–568. doi:10.1016/j.matchemphys.2009.04.037.
- [63] P. Roy, S. Berger, P. Schmuki, TiO₂-Nanoröhren: Synthese und Anwendungen, *Angew. Chemie.* 123 (2011) 2956–2995. doi:10.1002/ange.201001374.
- [64] H. Tsuchiya, J.M. Macak, L. Müller, J. Kunze, F. Müller, P. Greil, S. Virtanen, P. Schmuki, Hydroxyapatite growth on anodic TiO₂ nanotubes, *J. Biomed. Mater. Res.* 77 A (2006) 534–541.
- [65] Y. Wang, H. Yu, C. Chen, Z. Zhao, Review of the biocompatibility of micro-arc oxidation coated titanium alloys, *Mater. Des.* 85 (2015) 640–652. doi:10.1016/j.matdes.2015.07.086.
- [66] N.P. Sluginov, -, *J. Russ. Phys. Chem.* 12 (1880) 1–2.
- [67] A.G. Schulze, H. Betz, *Electrolytkondensatoren-Ihre Entwicklung, wissenschaftliche Grundlage, Herstellung, Messung und Verwendung*, Krayn. (1937).
- [68] W. Mc Niell, G. Nordbloom, Method of making cadmium niobate, US2854390 A, 1958.
- [69] W. Mc Niell, G. Nordbloom, Anodic spark reaction processes and articles, US 3293158 A, 1966.
- [70] G. Markov, G. Markova, The formation method of anodic electrolytic condensation, 526961, 1976.
- [71] A.V. Nikolaev, G.A. Markov, B.I. Peshchevitskij, In Russian, *Izv. SO ANSSSR. Ser. Khim. Nauk* 5. 5 (1977) 32.
- [72] Keronite, 09.10.2017. (2017). <http://www.keronite.com/benefits/>.
- [73] E. Pfeifer, Automoteam, 09.10.2017. (2017). <http://www.metaker.com/impresum.html>.
- [74] D.H. Sauer, ACH Oberflächentechnik, 09.10.2017. (2017). <https://www.ahc-surface.com/de/oberflaechentechnik/verfahren/magoxid-coat/>.

BIBLIOGRAPHY

- [75] F.C. Walsh, C.T.J. Low, R.J.K. Wood, K.T. Stevens, J. Archer, a. R. Poeton, a. Ryder, Plasma electrolytic oxidation (PEO) for production of anodised coatings on lightweight metal (Al, Mg, Ti) alloys, *Trans. Inst. Met. Finish.* 87 (2009) 122–135. doi:10.1179/174591908X372482.
- [76] B.L. Jiang, Y.M. Wang, Plasma Electrolytic Oxidation Treatment of Aluminum and Titanium Alloys, *Surf. Eng. Light Alloy. Aluminum, Magnes. Titan. Alloy*, Woodhead Publishing, 2010.
- [77] Y. Cheng, Z. Xue, Q. Wang, X.-Q. Wu, E. Matykina, P. Skeldon, New findings on properties of plasma electrolytic oxidation coatings from study of an Al–Cu–Li alloy, *Electrochim. Acta.* 107 (2013) 358–378.
- [78] Y. Cheng, F. Wu, E. Matykina, P. Skeldon, G.E.E. Thompson, The influences of microdischarge types and silicate on the morphologies and phase compositions of plasma electrolytic oxidation coatings on Zircaloy-2, *Corros. Sci.* 59 (2012) 307–315.
- [79] P. Gupta, G. Tenhundfeld, E.O. Daigle, D. Ryabkov, Electrolytic plasma technology: Science and engineering—An overview, *Surf. Coatings Technol.* 201 (2007) 8746–8760.
- [80] X. Liu, P.K. Chu, C. Ding, Surface nano-functionalization of biomaterials, *Mater. Sci. Eng. R Reports.* 70 (2010) 275–302. doi:10.1016/j.mser.2010.06.013.
- [81] X. Zhang, Z. Yao, Z. Jiang, Y. Zhang, X. Liu, Investigation of the plasma electrolytic oxidation of Ti–6Al–4V under single-pulse power supply, *Corros. Sci.* 53 (2011) 2253–2262.
- [82] T.H. Teh, A. Berkani, S. Mato, P. Skeldon, G.E. Thompson, H. Habazaki, Initial stages of plasma electrolytic oxidation of titanium, *Corros. Sci.* 45 (2003) 2757–2768.
- [83] R.O. Hussein, X. Nie, D.O. Northwood, An investigation of ceramic coating growth mechanisms in plasma electrolytic oxidation (PEO) processing, *Electrochim. Acta.* 112 (2013) 111–119.
- [84] T. Mi, B. Jiang, Z. Liu, L. Fan, *Electrochimica Acta* Plasma formation mechanism of microarc oxidation, 123 (2014) 369–377. doi:10.1016/j.electacta.2014.01.047.
- [85] R.O. Hussein, D.O. Northwood, X. Nie, Coating growth behavior during the plasma electrolytic oxidation process, *J. Vac. Sci. Technol. A Vacuum, Surfaces Film.* 28 (2010) 766–773.
- [86] H. Guo, M. An, S. Xu, H. Huo, Formation of oxygen bubbles and its influence on current efficiency in micro-arc oxidation process of AZ91D magnesium alloy, *Thin Solid Film.* 485 (2005) 53–58.
- [87] W. Xue, Z. Deng, Y. Lai, R. Chen, Analysis of Phase Distribution for Ceramic Coatings Formed by Microarc Oxidation on Aluminum Alloy, *J. Am. Ceram. Soc.* 81 (1998) 1365–1368.
- [88] G. Sundararajan, L. Rama Krishna, Mechanisms underlying the formation of thick alumina coatings through the MAO coating technology, *Surf. Coatings Technol.* 167 (2003) 269–277. doi:10.1016/S0257-8972(02)00918-0.
- [89] A.L. Yerokhin, L.O. Snizhko, N.L. Gurevina, A. Leyland, A. Pilkington, A. Matthews,

BIBLIOGRAPHY

- Discharge characterization in plasma electrolytic oxidation of aluminium, *J. Phys. D. Appl. Phys.* 36 (2003) 2110–2120.
- [90] M. Treviño, R.D. Mercado-Solis, R. Colás, A. Pérez, J. Talamantes, A. Velasco, Erosive wear of plasma electrolytic oxidation layers on aluminium alloy 6061, *Wear*. 301 (2012) 434–441.
- [91] H. Ma, D. Li, C. Liu, Z. Huang, D. He, Q. Yan, P. Liu, P. Nash, D. Shen, An investigation of (NaPO₃)₆ effects and mechanisms during micro-arc oxidation of AZ31 magnesium alloy, *Surf. Coatings Technol.* 266 (2015) 151–159. doi:10.1016/j.surfcoat.2015.02.033.
- [92] Y. V. Khokhryakov, P.I. Butyagin, A.I. Mamaev, Formation of dispersed particles during plasma oxidation, *J. Mater. Sci.* 40 (2005) 3007–3008. doi:10.1007/s10853-005-2383-z.
- [93] A.E.R. Friedemann, T.M. Gesing, P. Plagemann, Electrochemical rutile and anatase formation on PEO surfaces, *Surf. Coat. Technol.* 315 (2017) 139–149. doi:10.1016/j.surfcoat.2017.01.042.
- [94] E. Matykina, R. Arrabal, P. Skeldon, G.E. Thompson, Transmission electron microscopy of coatings formed by plasma electrolytic oxidation of titanium, *Acta Biomater.* 5 (2009) 1356–1366. doi:10.1016/j.actbio.2008.10.007.
- [95] D.S. Doolabi, M. Ehteshamzadeh, S.M.M. Mirhosseini, Effect of NaOH on the Structure and Corrosion Performance of Alumina and Silica PEO Coatings on Aluminum, 21 (2012) 2195–2202. doi:10.1007/s11665-012-0151-1.
- [96] A. Polat, M. Makaraci, M. Usta, Influence of sodium silicate concentration on structural and tribological properties of microarc oxidation coatings on 2017A aluminum alloy substrate, *J. Alloys Compd.* 504 (2010) 519–526. doi:10.1016/j.jallcom.2010.06.008.
- [97] S. Durdu, M. Usta, Characterization and mechanical properties of coatings on magnesium by micro arc oxidation, *Appl. Surf. Sci.* 261 (2012) 774–782.
- [98] H.Y. Zheng, Y.K. Wang, B.S. Li, G.R. Han, The effects of Na₂WO₄ concentration on the properties of microarc oxidation coatings on aluminum alloy, *Mater. Lett.* 59 (2005) 139–142.
- [99] Y. Liu, J. Xu, Y. Gao, Y. Yuan, C. Gao, Influences of Additive on the Formation and Corrosion Resistance of Micro-arc Oxidation Ceramic Coatings on Aluminum Alloy, *Phys. Procedia.* 32 (2012) 107–112. doi:10.1016/j.phpro.2012.03.526.
- [100] X. Liua, G. Liu, J. Xie, Preliminary Study on Preparation of Black Ceramic Coating Formed on Magnesium Alloy by Micro-arc Oxidation in Carbon Black Pigment-contained Electrolyte, 36 (2012) 261–269. doi:10.1016/j.proeng.2012.03.039.
- [101] A. Mandelli, M. Bestetti, A. Da Forno, N. Lecis, S.P. Trasatti, M. Trueba, A composite coating for corrosion protection of AM60B magnesium alloy, *Surf. Coat. Technol.* 205 (2011) 4459–4465. doi:10.1016/j.surfcoat.2011.03.066.
- [102] M. Aliofkhazraei, A.S. Rouhaghdam, Wear and coating removal mechanism of alumina / titania nanocomposite layer fabricated by plasma ..., (2011). doi:10.1016/j.surfcoat.2011.02.058.

BIBLIOGRAPHY

- [103] C.J.-P. Steiner, D.P.H. Hasselman, R.M. Spriggs, Kinetics of the Gamma-to-Alpha Alumina Phase Transformation, *J. Am. Ceram. Soc.* 54 (n.d.) 412–413.
- [104] E. Matykina, R. Arrabal, P. Skeldon, G.E. Thompson, Investigation of the growth processes of coatings formed by AC plasma electrolytic oxidation of aluminium, *Electrochim. Acta.* 54 (2009) 6767–6778. doi:10.1016/j.electacta.2009.06.088.
- [105] H. Kalkanc, S.C. Kurnaz, The effect of process parameters on mullite-based plasma electrolytic oxide coatings, *Surf. Coatings Technol.* 203 (2008) 15–22. doi:10.1016/j.surfcoat.2008.07.015.
- [106] R.O. Hussein, D.O. Northwood, X. Nie, The effect of processing parameters and substrate composition on the corrosion resistance of plasma electrolytic oxidation (PEO) coated magnesium alloys, *Surf. Coatings Technol.* 237 (2013) 357–368.
- [107] J.A. Curran, H. Kalkanc, Y. Magurova, T.W. Clyne, Mullite-rich plasma electrolytic oxide coatings for thermal barrier applications, 201 (2007) 8683–8687. doi:10.1016/j.surfcoat.2006.06.050.
- [108] J.A. Curran, T.W. Clyne, Porosity in plasma electrolytic oxide coatings, *Acta Mater.* 54 (2006) 1985–1993.
- [109] W.J. Felske, A. Plieth, Raman spectroscopy of titanium dioxide layers, *Electrochim. Acta.* 1 (1989) 75–77.
- [110] J. Lausmaa, L. Mattsson, U. Rolander, B. Kasemo, G. Rådegran, Preparation of ultra-thin oxid windows on titanium for TEM analysis, *J. Electron Microsc. Tech.* 19 (1999) 99–106.
- [111] J. Winkler, *Titandioxid*, Vincentz-Verlag, Hannover, 2003.
- [112] E. Riedel, C. Janiak, *Anorganische Chemie*, 8 th, De Gruyter, Berlin, New York, 2011.
- [113] S.-D. Mo, W.Y. Ching, Electronic and optical properties of three phases of titanium dioxide: Rutile, anatase, and brookite, *Phys. Rev. B.* 51 (1995) 13023–13032.
- [114] D.M. Tobaldi, R.C. Pullar, M.P. Seabra, J.A. Labrincha, Fully Quantitative X-ray Characterisation of Evonik Aeroxide TiO₂ P25 ®, *Mater. Lett.* (2014) 345–347. doi:10.1016/j.matlet.2014.02.055.
- [115] T. Ohno, K. Sarukawa, K. Tokieda, M. Matsumura, Morphology of a TiO₂ Photocatalyst (Degussa, P-25) Consisting of Anatase and Rutile Crystalline Phases, *J. Catal.* (2001) 82–86.
- [116] D. Wöhrle, M.W. Tausch, W.-D. Stohrer, *Photochemie: Konzept, Methoden, Experimente*, Wiley-VCH, Weinheim, 1998.
- [117] IUPAC: International Union of Pure and Applied Chemistry, (2017). <https://iupac.org/>.
- [118] A. Aboelzhab, A.M. Azad, S. Dolan, V. Goel, Mitigation of Staphylococcus aureus - mediated surgical site infections with IR photoactivated TiO₂ coatings on Ti implants, *Adv. Healthc. Mater.* 1 (2012) 285–291. doi:10.1002/adhm.201100032.
- [119] M. Castellote, N. Bengtsson, *Application of Titanium Dioxide Photocatalysis to Construction Materials*, 2011. doi:10.1007/978-94-007-1297-3_2.

BIBLIOGRAPHY

- [120] S.E. Braslavsky, Organic and biomolecular chemistry division, subcommittee on photochemistry, Glossary of terms used in photochemistry, 3rd edition (IUPAC Recommendations 2006), *Pure Appl. Chem.* 79 (2007) 293–465. doi:DOI: 10.1351/pac200779030293.
- [121] R. de Richter, S. Caillol, Fighting global warming: The potential of photocatalysis against CO₂, CH₄, N₂O, CFCs, tropospheric O₃, BC and other major contributors to climate change, *J. Photochem. Photobiol. C Photochem. Rev.* 12 (2011) 1–19. doi:DOI: 10.1016/j.jphotochemrev.2011.05.002.
- [122] A. Galińska, 1143-1147. J. Walendziewski, 2005, 19, Photocatalytic Water Splitting over Pt–TiO₂ in the Presence of Sacrificial Reagents, *Energy & Fuels.* 19 (2005) 1143–1147. doi:10.1021/ef0400619.
- [123] M. Seyler, K. Stoewe, W.F. Maier, New hydrogen-producing photocatalysts-A combinatorial search, *Appl. Catal. B Environ.* 76 (2007) 146–157. doi:10.1016/j.apcatb.2007.05.020.
- [124] C. Shifu, Y. Xiaoling, Zhang Huaye, L. Wie, Preparation and Photocatalytic Activity Evaluation of Composite Fe–TiO₂/TiO₂ Photocatalyst, *J. Electrochem. Soc.* 157 (2010) K96–K102.
- [125] W. Jia, B. Jia, F. Qu, X. Wu, Towards a highly efficient simulated sunlight driven photocatalyst: a case of heterostructured ZnO/ZnS hybrid structure., *Dalton Trans.* 42 (2013) 14178–87. doi:10.1039/c3dt51712h.
- [126] J.I. Goldsmith, W.R. Hudson, M.S. Lowry, T.H. Anderson, S. Bernhard, Discovery and high-throughput screening of heteroleptic iridium complexes for photoinduced hydrogen production, *J. Am. Chem. Soc.* 127 (2005) 7502–7510. doi:10.1021/ja0427101.
- [127] P. Dunlop, C.P. Sheeran, J.A. Byrne, M. McMahon, M.A. Boyle, K.G. McGuigan, Inactivation of clinically relevant pathogens by photocatalytic coatings, *J. Photochem. Photobiol. A Chem.* 216 (2010) 303–310. doi:DOI: 10.1016/j.jphotochem.2010.07.004.
- [128] K. Shiraishi, H. Koseki, T. Tsurumoto, K. Baba, M. Naito, K. Nakayama, H. Shindo, Antibacterial metal implant with a TiO₂-conferred photocatalytic bactericidal effect against *Staphylococcus aureus*, *Surf. Interface Anal.* 41 (2009) 17–22. doi:10.1002/sia.2965.
- [129] A.M. Gallardo-Moreno, M.A. Pacha-Olivenza, M.C. Fernández-Calderón, C. Pérez-Giraldo, J.M. Bruque, M.L. González-Martín, Bactericidal behaviour of Ti₆Al₄V surfaces after exposure to UV-C light, *Biomaterials.* 31 (2010) 5159–5168. doi:10.1016/j.biomaterials.2010.03.005.
- [130] J.-W. Seo, H. Chung, M.-Y. Kim, J. Lee, I.-H. Choi, J. Cheon, Development of Water-Soluble Single-Crystalline TiO₂ Nanoparticles for Photocatalytic Cancer-Cell Treatment, *Small.* 3 (2007) 850–853. doi:DOI: 10.1002/sml.200600488.
- [131] R. Imani, P. Veranic, A. Iglic, M. Erdani Kreft, M. Pazoki, S. Hudoklin, Combined cytotoxic effect of UV-irradiation and TiO₂ microbeads in normal urothelial cells, low-grade and high-grade urothelial cancer cells, *Photochem. Photobiol. Sci.* 14 (2015) 583–590. doi:10.1039/c0pp00354a.

BIBLIOGRAPHY

- [132] A. Fujishima, K. Honda, Electrochemical Photolysis of Water at a Semiconductor Electrode, *Nature*. 238 (1972) 37–38. doi:10.1038/238037a0.
- [133] K. Hashimoto, H. Irie, A. Fujishima, TiO₂ Photocatalysis: A Historical Overview and Future Prospects, *Jpn. J. Appl. Phys.* 44 (2005) 8269–8285.
- [134] T. Ochiai, A. Fujishima, Photoelectrochemical properties of TiO₂ photocatalyst and its applications for environmental purification, *J. Photochem. Photobiol. C Photochem. Rev.* 13 (2012) 247–262. doi:10.1016/j.jphotochemrev.2012.07.001.
- [135] Y. Paz, Application of TiO₂ photocatalysis for air treatment: Patents' overview, *Appl. Catal. B Environ.* 99 (2010) 448–460. doi:10.1016/j.apcatb.2010.05.011.
- [136] A.L. Linsebigler, L. Guangquan, J.T. Yates, Photocatalysis on TiO₂ Surfaces: Principles, Mechanisms, and Selected Results, *Chem. Rev.* 95 (1995) 735–758.
- [137] A. Fujishima, T.N. Ra, D.A. Tryk, Titanium dioxide photocatalysis, *J. Photochem. Photobiol. C Photochem. Rev.* (2000) 1–12.
- [138] M. Grätzel, Heterogeneous Photochemical Electron Transfer, in: CRC Press, Boca Raton, 1989.
- [139] H. Kominamia, Y. Ishiia, M. Kohnoa, S. Konishia, Y. Keraa, B. Ohtani, Nanocrystalline brookite-type titanium(IV) oxide photocatalysts, *Catal. Letters*. 91 (2003) 41–47.
- [140] Y. Tian, J. Zhang, J.-C. Ma, X. Jia, Monodisperse rutile microspheres with ultrasmall nanorods on surfaces: Synthesis, characterization, luminescence, and photocatalysis, *J. Colloid Interface Sci.* 385 (2012) 1–7. doi:10.1016/j.jcis.2012.06.086.
- [141] H.R. Kricheldorf, *Menschen und ihre Materialien: Von der Steinzeit bis heute*, 1st ed., Wiley-VCH Verlag, 2012.
- [142] R. Thull, Oberflächenmodifikationen zur verbesserung von biokompatibilit??t und mechanischen eigenschaften von orthopädischen implantaten, *Orthopade*. 32 (2003) 51–59. doi:10.1007/s00132-002-0412-z.
- [143] H.P. Jennissen, *Verträglichkeit groß geschrieben*, *Essener Unikate*. 13 (2000) 78–93.
- [144] J. Michael, B. Schwenzer, D. Scharnweber, R. Beutner, Biological nano-functionalization of titanium-based biomaterial surfaces: a flexible toolbox, *J. R. Soc. Interface*. 7 (2010) 93–105.
- [145] R. Kramme, *Medizintechnik*, 3rd ed., Springer Verlag, 2007.
- [146] M.N. Smith-Petersen, Arthroplasty of the Hip: A New Method, *J. Bone Jt. Surg.* 2 (1939) 269–288.
- [147] H.E. LeMay, B.E. Bursten, T.L. Brown, *Chemie-Studieren kompakt*, 10th ed., Pearson, 2011.
- [148] R. Schmitt, *Werkstoffverhalten im biologischen System*, Springer Verlag, 1999.
- [149] R. Ströbel, G. Rau, *Grundwissen für Zahntechniker-Die Metalle*, 19th ed., Verlag Neuer Merkur GmbH, 2004.

BIBLIOGRAPHY

- [150] L. Kiontke, *Medizintechnik-Biomaterialien*, 3rd ed., Springer Verlag, 2007.
- [151] M. Peters, H. Clemens, Titan, Titanlegierungen und Titanaluminide – Basis für innovative Anwendungen, *BHM Berg- Und Hüttenmännische Monatshefte*. 155 (2010) 402–408. doi:10.1007/s00501-010-0590-7.
- [152] S. Koltzenburg, M. Maskos, O. Nuyken, *Polymere: Synthese, Eigenschaften und Anwendungen*, Springer Verlag, Berlin, Heidelberg, 2014.
- [153] E. Wintermantel, G. Maier, S.-W. Ha, *Medizintechnik-Biokompatible Polymere*, 5th ed., Springer Verlag, 2009.
- [154] D.J. Lyman, *Kunststoffe in der Medizin*, *Angew. Chem.* 4 (1974) 145–150.
- [155] B. Tieke, *Makromolekulare Chemie: Eine Einführung*, 3rd ed., Wiley-VCH, 2014.
- [156] W. Kaiser, *Kunststoffchemie für Ingenieure: von der Synthese bis zur Anwendung*, 2nd ed., Carl Hanser Verlag, München, 2008.
- [157] R.J. Young, P.A. Lovell, *Introduction to Polymers*, 3rd ed., CRC Press, 2011.
- [158] G. Hauser, *Hygienische Produktionstechnologie*, Wiley-VCH Verlag, 2008.
- [159] A.S. Hoffmann, F.J. Schoen, J.E. Lemons, B.R. Ratner, *An Introduction to Materials in Medicine in Biomaterials Science*, Acad. Press. (1996).
- [160] K. Matsuzaka, T. Inoue, Y. Oda, M. Shimono, M. Yoshinari, *Bio-Functionalization of Titanium Surface for Dental Implants*, *Mater. Trans.* 10 (2002) 2494–2501.
- [161] H. Zimmermann, M. Heinlein, N.W. Guldner, *Titanisierung von Implantatoberflächen*, *Medizintechnik*. (2009) 907–925. doi:10.1007/978-3-540-93936-8_39.
- [162] W. Mittelmeier, W. Plotz, R. Gradinger, *Osteoarthritis of the hip joint - Causes and therapeutic options*, *Fortschritte Der Medizin*. 115 (1997) 34–39.
- [163] M.P. Casaletto, S. Kaciulis, G. Mattogno, A. Mezzi, L. Ambrosio, F. Branda, *XPS characterization of biocompatible hydroxyapatite-polymer coatings*, *Surf. Interface Anal.* 34 (2002) 45–49. doi:10.1002/sia.1249.
- [164] M.A. Baker, S.L. Assis, O.Z. Higa, I. Costa, *Nanocomposite hydroxyapatite formation on a Ti-13Nb-13Zr alloy exposed in a MEM cell culture medium and the effect of H₂O₂ addition*, *Acta Biomater.* 5 (2009) 63–75. doi:10.1016/j.actbio.2008.08.008.
- [165] V.M. Frauchiger, F. Schlottig, B. Gasser, M. Textor, *Anodic plasma-chemical treatment of CP titanium surfaces for biomedical applications*, *Biomaterials*. 25 (2004) 593–606. doi:10.1016/S0142-9612(03)00560-X.
- [166] C.C. Berndt, G.N. Haddad, A.J.D. Farmer, K.A. Gross, *Characterization of Thermal Sprayed Hydroxyapatite Powders and Coatings*, *Mater. Forum*. 14 (1990) 161–173.
- [167] J. Lee, H. Aoki, *Hydroxyapatite coating by dipping method, and bone bonding strength*, *Biomed. Mater. Eng.* 5 (1995) 49–58.
- [168] H. Baumann, K. Bethge, G. Bilger, D. Jones, I. Symietz, *Thin hydroxyapatite surface layers on titanium produced by ion implantation*, *Nucl. Instrum. Methods Phys. Res. B*.

BIBLIOGRAPHY

- 196 (2002) 286–292.
- [169] T. Peltola, M. Patsi, H. Rahiala, I. Kangasniemi, A. Yli-Urpo, Calcium phosphate induction by sol-gel-derived titania coatings on titanium substrates in vitro, *J. Biomed. Mater. Res.* 41 (1998) 504–510.
- [170] L.Á. de Sena, M.C. de Andrade, A.M. Rossi, G.A. Soares, Hydroxyapatite deposition by electrophoresis on titanium sheets with different surface finishing, *J. Biomed. Mater. Res.* 60 (2002) 1–7.
- [171] J.S. Chen, H.Y. Juang, M.H. Hon, Calcium phosphate coating on titanium substrate by a modified electrocrystallization process, *Mater. Sci. Eng. - Mater. Med.* 9 (1998) 297–300.
- [172] R. Luo, Z. Liu, F. Yan, Y. Kong, Y. Zhang, The biocompatibility of hydroxyapatite film deposition on micro-arc oxidation Ti6Al4V alloy, *Appl. Surf. Sci.* 266 (2013) 57–61. doi:10.1016/j.apsusc.2012.11.074.
- [173] D. Wei, Y. Zhou, D. Jia, Y. Wang, Structure of calcium titanate/titania bioceramic composite coatings on titanium alloy and apatite deposition on their surfaces in a simulated body fluid, *Surf. Coatings Technol.* 201 (2007) 8715–8722. doi:10.1016/j.surfcoat.2007.04.124.
- [174] A. Alsarani, G. Purcek, I. Hacisalihoglu, Y. Vangolu, O. Bayrak, I. Karaman, A. Celik, Hydroxyapatite production on ultrafine-grained pure titanium by micro-arc oxidation and hydrothermal treatment, *Surf. Coatings Technol.* 205 (2011) S537–S542. doi:10.1016/j.surfcoat.2011.03.032.
- [175] J. Mayer, L.A. Giannuzzi, T. Kamino, J. Michael, TEM Sample Preparation and FIB-Induced Damage, *MRS Bull.* 32 (2007) 400–407. doi:doi.org/10.1557/mrs2007.63.
- [176] A. Houas, H. Lachheb, M. Ksibi, E. Elaloui, C. Guillard, J.-M. Herrmann, Photocatalytic degradation pathway of methylene blue in water, *Appl. Catal. B Environ.* 31 (2001) 145–157. doi:10.1016/S0926-3373(00)00276-9.
- [177] P. Wilhelm, D. Stephan, Photodegradation of rhodamine B in aqueous solution via SiO₂@TiO₂ nano-spheres, *J. Photochem. Photobiol. A Chem.* 185 (2007) 19–25. doi:10.1016/j.jphotochem.2006.05.003.
- [178] C.J. Pendegrass, C.A. Middleton, D. Gordon, J. Jacob, G.W. Blunn, Measuring the strength of dermal fibroblast attachment to functionalized titanium alloys in vitro, *J Biomed Mater Res A.* 92 (2010) 1028–1037.
- [179] K. Venkateswarlu, N. Rameshbabu, D. Sreekanth, M. Sandhyarani, A.C. Bose, V. Muthupandi, S. Subramanian, Role of electrolyte chemistry on electronic and in vitro electrochemical properties of micro-arc oxidized titania films on Cp Ti, *Electrochim. Acta.* 105 (2013) 468–480. doi:10.1016/j.electacta.2013.05.032.
- [180] P. Kern, O. Zinger, Purified titanium oxide with novel morphologies upon spark anodization of Ti alloys in mixed H₂SO₄/H₃PO₄ electrolytes, *J. Biomed. Mater. Res. Part A.* 80A (2006) 283–296. doi:10.1002/jbm.a.
- [181] Y.T. Sul, C.B. Johansson, Y. Jeong, T. Albrektsson, The electrochemical oxide growth behaviour on titanium in acid and alkaline electrolytes, *Med. Eng. Phys.* 23 (2001) 329–346. doi:10.1016/S1350-4533(01)00050-9.

BIBLIOGRAPHY

- [182] H. Ishizawa, M. Ogino, Formation and characterization of anodic titanium oxide films containing Ca and P, *J. Biomed. Mater. Res.* 29 (1995) 65–72. doi:10.1002/jbm.820290110.
- [183] S. Ito, K. Koizuka, M. Hirochi, T. Onaka, H.M.T. Haneda, Anodic Oxidation of Titanium in Phosphoric Acid-Sulfuric Acid System Electrolytic Bath, *J. Japan Soc. Colour Mater.* 61 (1988) 599–605.
- [184] M.E. Sibert, Electrochemical oxidation of titanium surfaces, *J. Electrochem. Soc.* 110 (1963) 65–71.
- [185] J.S.L. Dyer, K C; Leach, Breakdown and efficiency of anodic oxide growth on titanium, *J. Electrochem. Soc.* 125 (1978) 1032–1038.
- [186] N. Ohtsuka, T; Masuda, M; Sato, Ellipsometric study of anodic oxide films on titanium in hydrochloric acid, sulfuric acid, and phosphate solution, *J. Electrochem. Soc.* 132 (1985) 787–92.
- [187] Z. Su, L. Zhang, F. Jiang, M. Hong, Formation of crystalline TiO₂ by anodic oxidation of titanium, *Prog. Nat. Sci. Mater. Int.* 23 (2013) 294–301. doi:10.1016/j.pnsc.2013.04.004.
- [188] M. V. Diamanti, M.P. Pedefferri, Effect of anodic oxidation parameters on the titanium oxides formation, *Corros. Sci.* 49 (2007) 939–948. doi:10.1016/j.corsci.2006.04.002.
- [189] M. Fengcang, L. Ping, L. Wei, L. Xinkuan, C. Xiaohong, H. Daihua, W. Liqiang, G. Fang, Effect of Applied Voltage on the Microstructure and Bioactivity of MAO Film on Ti Substrate, 54 (2013) 1800–1804. doi:10.2320/matertrans.M2013004.
- [190] B. Kasalica, M. Petkovic, I. Belca, S. Stojadinovic, L. Zekovic, Electronic transitions during plasma electrolytic oxidation of aluminum, *Surf. Coatings Technol.* 203 (2009) 3000–3004.
- [191] V. Swamy, D. Menzies, B.C. Muddle, A. Kuznetsov, L.S. Dubrovinsky, Q. Dai, V. Dmitriev, Nonlinear size dependence of anatase TiO₂ lattice parameters, *Appl. Phys. Lett.* 88 (2006) 1–4. doi:10.1063/1.2213956.
- [192] I. Djerdj, A.M. Tonejc, Structural investigations of nanocrystalline TiO₂ samples, *J. Alloys Compd.* 413 (2006) 159–174. doi:10.1016/j.jallcom.2005.02.105.
- [193] I.E. Grey, N.C. Wilson, Titanium vacancy defects in sol–gel prepared anatase, *J. Solid State Chem.* 180 (2007) 670–678. doi:10.1016/j.jssc.2006.11.028.
- [194] Y. Li, T.J. White, S.H. Lim, Low-temperature synthesis and microstructural control of titania nano-particles, *J. Solid State Chem.* 177 (2004) 1372–1381. doi:10.1016/j.jssc.2003.11.016.
- [195] A.Y. Kuznetsov, R. MacHado, L.S. Gomes, C.A. Achete, V. Swamy, B.C. Muddle, V. Prakapenka, Size dependence of rutile TiO₂ lattice parameters determined via simultaneous size, strain, and shape modeling, *Appl. Phys. Lett.* 94 (2009) 2009–2011. doi:10.1063/1.3139078.
- [196] A.E.R. Friedemann, K. Thiel, T.M. Gesing, P. Plagemann, Photocatalytic activity of titania films produced with plasma electrolytic oxidation, *Surf. Coat. Technol.* (2018) submitted.

BIBLIOGRAPHY

- [197] J. Tauc, R. Grigorovici, V. A. Optical properties and electronic structure of amorphous germanium, *Phys. Status Solidi*. 15 (1996) 627–637. doi:10.1002/pssb.19660150224.
- [198] D. Souri, Z.E. Tahan, A new method for the determination of optical band gap and the nature of optical transitions in semiconductors, *Appl. Phys. B Lasers Opt.* 119 (2015) 273–279. doi:10.1007/s00340-015-6053-9.
- [199] P. Kubelka, F. Munk, Ein Beitrag zur Optik der Farbanstriche, *Zeitschrift Für Tech. Phys.* 12 (1931) 593–601.
- [200] V. Džimbeg-malčić, Ž. Barbarić-mikočević, K. Itrić, Kubelka-Munk Theory in Describing Optical Properties of Paper (1), *Tech. Gaz.* 18 (2011) 117–124. doi:10.1017/CBO9781107415324.004.
- [201] A. Kirsch, M.M. Murshed, M. Schowalter, A. Rosenauer, T.M. Gesing, Nanoparticle precursor into polycrystalline Bi₂Fe₄O₉: An evolutionary investigation of structural, morphological, optical and vibrational properties., *J. Phys. Chem. C.* 120 (2016) 18831–18840.
- [202] M. Teck, M.M. Murshed, M. Schowalter, N. Lefeld, H.K. Grossmann, T. Grieb, T. Hartmann, L. Robben, A. Rosenauer, L. Mädler, T.M. Gesing, Structural and spectroscopic comparison between polycrystalline, nanocrystalline and quantum dot visible light photo-catalyst Bi₂WO₆., *J. Solid State Chem.* (2017). submitted.
- [203] K.M. Reddy, S. V. Manorama, A.R. Reddy, Bandgap studies on anatase titanium dioxide nanoparticles, *Mater. Chem. Phys.* 78 (2003) 239–245. doi:10.1016/S0254-0584(02)00343-7.
- [204] M. Inagaki, R. Nonaka, B. Tryba, A.W. Morawski, Dependence of photocatalytic activity of anatase powders on their crystallinity, *Chemosphere.* 64 (2006) 437–445. doi:10.1016/j.chemosphere.2005.11.052.
- [205] H. Kominami, J. Kato, M. Kohno, Y. Kera, B. Ohtani, Photocatalytic Mineralization of Acetic Acid in Aerated Aqueous Suspension of Ultra-highly Active Titanium(IV) Oxide Prepared by Hydrothermal Crystallization in Toluene, *Chem. Lett.* 12 (1996) 1051–1052.
- [206] F. Amano, O.-O. Preto-Mahaney, Y. Terada, T. Yasumoto, T. Shibayama, B. Ohtani, Decahedral Single-Crystalline Particles of Anatase Titanium(IV) Oxide with High Photocatalytic Activity, *Chem. Mat.* 21 (2009) 2601–2603. doi:DOI: 10.1021/cm9004344.
- [207] O. Carp, C.L. Huisman, A. Reller, Photoinduced reactivity of titanium dioxide, *Prog. Solid State Chem.* 32 (2004) 33–177.
- [208] A. Friedemann, M. Burchardt, N. Shirazi, T. Fladung, I. Grunwald, D. Salz, Beschichtetes Substrat mit titanhaltiger Beschichtung und modifizierter Titanoxidbeschichtung, DE 10 2017 111 784.9, 2017.
- [209] P. Zhang, Z. Zhang, W. Li, M. Zhu, Effect of Ti-OH groups on microstructure and bioactivity of TiO₂ coating prepared by micro-arc oxidation, *Appl. Surf. Sci.* 268 (2013) 381–386. doi:10.1016/j.apsusc.2012.12.105.
- [210] T. Kokubo, H. Kushitani, S. Sakka, T. Kitsugi, T. Yamamuro, Solutions able to reproduce in vivo surface-structure changes in bioactive glass-ceramic A-W3, *J.*

BIBLIOGRAPHY

- Biomed. Mater. Res. 24 (1990) 721–734. doi:10.1002/jbm.820240607.
- [211] S. Ramesh, C. Tan, M. Hamdi, I. Sopyan, W. Teng, The influence of Ca / P ratio on the properties of hydroxyapatite bioceramics, (2014). doi:10.1117/12.779890.
- [212] J. Althaus, C. Padeste, J. Köser, U. Piele, K. Peters, B. Müller, Nanostructuring polyetheretherketone for medical implants, *Eur. J. Nanomedicine*. 4 (2012) 7–15. doi:10.1515/ejnm-2011-0001.
- [213] D.Y. Kim, M. Kim, H.E. Kim, Y.H. Koh, H.W. Kim, J.H. Jang, Formation of hydroxyapatite within porous TiO₂ layer by micro-arc oxidation coupled with electrophoretic deposition, *Acta Biomater*. 5 (2009) 2196–2205. doi:10.1016/j.actbio.2009.02.021.
- [214] F. Urselmann, F. Witte, K. Zanger, X. Li, D.C. Ayers, R. Krauspe, M. Jäger, Osteoblast differentiation onto different biometals with an endoprosthetic surface topography in vitro, *J. Biomed. Mater. Res. Part A*. 1 (2008) 61–75.
- [215] Y. Tian, S. Ding, H. Peng, S. Lu, G. Wang, L. Xia, P. Wang, Osteoblast growth behavior on porous-structure titanium surface, *Appl. Surf. Sci.* 261 (2012) 25–30. doi:10.1016/j.apsusc.2012.07.035.
- [216] Y.W. Lim, S.Y. Kwon, D.H. Sun, H.E. Kim, Y.S. Kim, Enhanced cell integration to titanium alloy by surface treatment with microarc oxidation: A pilot study, *Clin. Orthop. Relat. Res.* 467 (2009) 2251–2258. doi:10.1007/s11999-009-0879-6.
- [217] N. Suter, Evaluation of the influence of chemical and topographic trauma implant surface modification on cell adhesion using the example of osteoblasts, Fraunhofer Institut für Fertigungstechnik und Angewandte Materialforschung, 2015.
- [218] B. Heim, Zellbiologische Untersuchungen an funktionalisierten Titanoberflächen, Technische Universität München, Fraunhofer Institut für Fertigungstechnik und Angewandte Materialforschung, 2016.
- [219] L. Leoni, C.A. Grimes, T.A. Desai, K.C. Popat, Influence of engineered titania nanotubular surfaces on bone cells, *Biomaterials*. 28 (2007) 3188–3197.
- [220] O. Zinger, K. Anselme, A. Denzer, P. Habersetzer, M. Wieland, J. Jeanfils, Time-dependent morphology and adhesion of osteoblastic cells on titanium model surfaces featuring scale-resolved topography, 25 (2004) 2695–2711. doi:10.1016/j.biomaterials.2003.09.111.
- [221] Z. Schwartz, M. Wieland, F. Rupp, J. Geis-Gerstorfer, D.L. Cochran, B.D. Boyan, G. Zhao, High surface energy enhances cell response to titanium substrate microstructure, *J. Biomed. Mater. Res. Part A* 74 (2005) 49–58.
- [222] A.E.R. Friedemann, K. Thiel, U. Haßlinger, M. Ritter, T.M. Gesing, P. Plagemann, Investigations into the structure of PEO layers for understanding of layer formation, *Appl. Surf. Sci.* (2018) submitted.
- [223] F. Patcas, W. Krysmann, Efficient catalysts with controlled porous structure obtained by anodic oxidation under spark-discharge, *Appl. Catal. A Gen.* 316 (2007) 240–249. doi:10.1016/j.apcata.2006.09.028.
- [224] S.S. Saleh, C.C. Sorrell, H.Z. Abdullah, The Anatase Formation on Anodised Titanium

BIBLIOGRAPHY

- in Sulphuric Acid, *Adv. Mater. Res.* 1087 (2015) 334–339.
<http://www.scientific.net/AMR.1087.334>.
- [225] M. Shen, Z. Zhao, S. Wen, X. Chen, H. Li, Fabrication of CTP / HAp novel gradient composite bioceramics, *Trans. Nonferrous Met. Soc.* 17 (2007) 1385–1390.
- [226] O. Frank, M. Zikalova, B. Laskova, J. Kürti, J. Koltai, L. Kavan, Raman spectra of titanium dioxide (anatase, rutile) with identified oxygen isotopes (16, 17, 18), *Phys. Chem. Chem. Phys.* 14 (2012) 14567–14572. doi:10.1039/c2cp42763j.
- [227] C.B. Mendive, D.W. Bahnemann, M.A. Blesa, Microscopic characterization of the photocatalytic oxidation of oxalic acid adsorbed onto TiO₂ by FTIR-ATR, *Catal. Today.* 101 (2005) 237–244. doi:10.1016/j.cattod.2005.03.016.
- [228] C.B. Mendive, M.A. Blesa, D. Bahnemann, The adsorption and photodegradation of oxalic acid at the TiO₂ surface, *Water Sci. Technol.* 55 (2007) 139–145. doi:10.2166/wst.2007.398.
- [229] J.M. Meichtry, N. Quici, G. Mailhot, M.I. Litter, Heterogeneous photocatalytic degradation of citric acid over TiO₂. I: Mechanism of 3-oxoglutaric acid degradation, *Appl. Catal. B Environ.* 102 (2011) 454–463. doi:10.1016/j.apcatb.2010.12.026.
- [230] J.M. Meichtry, N. Quici, G. Mailhot, M.I. Litter, Heterogeneous photocatalytic degradation of citric acid over TiO₂. II. Mechanism of citric acid degradation, *Appl. Catal. B Environ.* 102 (2011) 555–562. doi:10.1016/j.apcatb.2010.12.038.
- [231] DIN EN ISO 4624:2016-08, Beschichtungsstoffe- Abreißversuch zur Bestimmung der Haftfestigkeit (ISO 4624:2016); Deutsche Fassung EN ISO 4624:2016

8. CURRICULUM VITAE

PERSÖNLICHE DATEN

NAME ARIANE FRIEDEMANN
GEBURTSDATUM 26.09.1985, HAMBURG
KONTAKT Op de Lust 58
21640 Nottensdorf
0176/61150241
ariane.friedemann@t-online.de

AKADEMISCHE AUSBILDUNG

2004 – 2007 Abitur an den Berufsbildenden Schulen Verden in Dauelsen
Fachgymnasium Ökotrophologie
Abschluss: Allgemeine Hochschulreife

2007 – 2011 **Bachelor Chemie:** Universität Bremen, Deutschland
Abschluss: Bachelor of Science

Feb. 2011 – Jun. 2011 **Bachelorarbeit:** „Synthese von Borcluster-Derivaten zur Anwendung als Acetylcholinesterase-Inhibitor“ bei Prof. Dr. D. Gabel am Institut für Organische Chemie und Biochemie

Okt. 2011 – März 2014 **Master Chemie:** Universität Bremen, Deutschland
Abschluss: Master of Science

Okt. 2012 – Jan. 2013 **Forschungspraktikum A:**
„Präparation und Charakterisierung von Bi₂Fe₄O₉-Nanopartikeln“ bei Prof. Dr. Thorsten M. Gelsing auf dem Gebiet der Chemischen Kristallographie fester Stoffe am Institut für Anorganische Chemie und Kristallographie, Universität Bremen

Feb. 2013 – Mai 2013 **Forschungspraktikum B:**
„Präparation poröser Titandioxidoberflächen mittels Microarc-Oxidation“ bei Prof. Dr. A. Hartwig am Fraunhofer-Institut für Fertigungstechnik und Angewandte Materialforschung IFAM, Bremen

Aug. 2013 – März 2014 **Masterarbeit:**
„Generierung biokompatibler Titandioxidschichten auf Edelstahl- und PEEK-Oberflächen mit Hilfe

CURRICULUM VITAE

plasmaelektrolytischer Oxidation“ bei Prof. Dr. A. Hartwig am Fraunhofer-Institut für Fertigungstechnik und Angewandte Materialforschung IFAM, Bremen

Okt. 2014 – Dez. 2017

Promotion:

Mit dem Thema „Preparation and structure elucidation of multifunctional porous titanium dioxide surfaces by means of plasma electrolytic oxidation“ am Fraunhofer-Institut für Fertigungstechnik und Angewandte Materialforschung IFAM, Bremen unter der Leitung von Herrn Dr. Peter Plagemann in Kooperation mit Herrn Prof. Dr. Thorsten M. Gesing, Chemischen Kristallographie fester Stoffe am Institut für Anorganische Chemie und Kristallographie, Universität Bremen

NEBENTÄTIGKEITEN

Jan. 2011 – März 2011

Studentische Hilfskraft, Universität Bremen, Prof. Dr. D. Gabel

Jun. 2011 – Okt. 2011

Praktikum am Institut für Pharmakologie, Zentrum für Spezielle Analytik und Medizinische Diagnostik, Klinikum Bremen Mitte

Juni 2011 – Sept. 2014

Anstellung als Wissenschaftliche Hilfskraft in Teilzeit/ Vollzeit am Fraunhofer-Institut für Fertigungstechnik und Angewandte Materialforschung IFAM (Bremen) im Bereich Korrosionsschutz und Elektrochemie

BESONDERE KENNTNISSE

Sprachen

Deutsch – Muttersprache

Englisch – gut in Wort, Schrift und Verständnis

Französisch – Grundkenntnisse

Latein – Grundkenntnisse

Japanisch – Grundkenntnisse

EDV

Gute Kenntnisse in Microsoft Word, Excel und Power Point

Grundkenntnisse in ChemSketch und ChemDoodle, Datenauswertung Topas, Image J, Gnuplot